Fall 2011

Large population evaluation of contact stress exposure in articular joints for prediction of osteoarthritis onset and progression

Andrew M. Kern
University of Iowa

Recommended Citation

Kern, Andrew M.. "Large population evaluation of contact stress exposure in articular joints for prediction of osteoarthritis onset and progression." MS (Master of Science) thesis, University of Iowa, 2011.
http://ir.uiowa.edu/etd/2725.

LARGE POPULATION EVALUATION OF CONTACT STRESS EXPOSURE IN ARTICULAR JOINTS FOR PREDICTION OF OSTEOARTHRITIS ONSET AND PROGRESSION

by

Andrew M. Kern

A thesis submitted in partial fulfillment
of the requirements for the Master of
Science degree in Biomedical Engineering
in the Graduate College of
The University of Iowa

December 2011

Thesis Supervisors: Associate Professor Donald D. Anderson
Professor Thomas D. Brown

Graduate College
The University of Iowa
Iowa City, Iowa

CERTIFICATE OF APPROVAL

MASTER'S THESIS

This is to certify that the Master's thesis of

Andrew M. Kern

has been approved by the Examining Committee
for the thesis requirement for the Master of Science
degree in Biomedical Engineering at the December 2011 graduation.

Thesis Committee: ___________________________________
Donald D. Anderson, Thesis Supervisor

____
Thomas D. Brown, Thesis Supervisor

____
Nicole M. Grosland

____
Tae-Hong Lim

____
Neil A. Segal

ACKNOWLEDGMENTS

I would first like to thank my thesis supervisors Drs. Don Anderson and Thomas Brown. Their knowledge, guidance and support have been crucial to my success and development over the past two years. Additionally, I would like to thank Dr. Neil Segal for his direction and support in the MOST dataset and its associated challenges. I would also like to thank the other members of my thesis committee, Drs. Nicole Grosland and Tae-Hong Lim for their guidance and perspectives on my work. A NIH NIAMS Program Grant P50 AR055533 provided funding for this research. I would like to thank the other students and faculty members in the Orthopaedic Biomechanics Research Laboratory not directly involved in my research for their questions, recommendations and support. Finally, I would like to thank my friends and family their love and support during this academic odyssey.

TABLE OF CONTENTS

LIST OF TABLES

Table

LIST OF FIGURES

Figure

CHAPTER 1: AN INTRODUCTION TO POST-TRAUMATIC OSTEOARTHRITIS AND CONTACT STRESS ASSESSMENT

Osteoarthritis (OA) is the most prevalent joint disease and one of the most common causes of pain and disability across all demographics [1]. It is estimated that joint pain and disability attributable to OA cost the nation on average 128 billion dollars or approximately 1% of GDP per year [2]. It also has a significant effect on a patient's quality of life, disabling approximately 10% of the population over the age of 60 [3]. The level of disability caused by lower extremity OA is comparable to that of heart failure or end stage kidney disease [4].

Given such a large societal impact, it is somewhat surprising how little is known about the factors involved in the onset and progression of OA [3]. OA is a condition in which both biological and mechanical factors are believed to play a significant role in the onset and worsening of OA symptoms [1, 3, 5-9]. There appears to be an intricate interplay between the mechanical stimuli given to cartilage and its subsequent biochemical and metabolic behavior.

The mechanical factors involved in OA onset and worsening are of particular interest, specifically measurement of contact stress exposure on articular joint surfaces. Prior research examined the role of contact stress and acute injury severity in the onset and worsening of post-traumatic osteoarthritis (PTOA) in the human ankle joint [9-13]. The results from these previous studies showed promising correlations between chronic contact stress exposure, acute injury severity and PTOA development. However, challenges in the methodologies used, primarily those related to patient-specific contact finite element analysis (FEA), limited studies to small samples sizes (n=11 and n=20) necessarily involving significant investigator time investment. For progress in this area, new methodologies need to be adapted or developed that allow for much greater subject numbers (hundreds or thousands), to feasibly be studied [7, 9].

Rigid body spring modeling, otherwise widely termed discrete element analysis (DEA) is a much simpler methodology than FEA for modeling contact between two surfaces [14-19] . It is a method which treats cartilage surfaces as a bed of compressive-only springs attached to an underlying rigid bone surface [20]. DEA does not involve the complex differential equation-solving that is central to FEA, but it is incapable of solving for the internal stresses or strains of an object. DEA returns only contact stress distributions and reaction forces generated from these contact stresses. The return upon this reduction in simulation complexity is greatly reduced computational time, and easier model preparation due to lack of an explicit FEA meshing step. DEA potentially enables much greater numbers of subject-specific contact stress evaluations to be run in the hopes of providing more statistical power with regard to determining the correlation between mechanical factors, such as contact stress exposure, and PTOA onset and worsening.

Prior to embarking on such studies, two important questions must be answered:

1. Can a DEA methodology for contact stress prediction on articular joint surfaces be developed which provides equivalent results as current FEA based methods, for the purpose of OA prediction?
2. Can such DEA methods be successfully extended to other joints with limited modifications?

In this thesis a purpose-written DEA algorithm is developed, evaluated for performance, and validated against a prior human ankle cadaver study. Then the DEA results are compared to previous FEA human ankle joint contact stress computations on the basis of node-by-node contact stress, population contact stress, and concordance to radiographic OA scores.

The DEA methodology is then combined with a purpose-written 3D-to-2D registration algorithm to evaluate contact stress across 38 subject-specific human knee models. The contact stress values are then correlated with the incidence of bone marrow lesion worsening, an indicator for joint pain and degeneration in the human knee.

CHAPTER 2: SUBJECT-SPECIFIC CONTACT STRESS COMPUTATION

2.1 Finite Element Analysis

Finite element analysis, or FEA, is the current standard in orthopaedic computational stress analysis methodology. It was introduced to the field of orthopaedic biomechanics in 1972 as a method of determining internal stresses present in skeletal models [21]. This method proved revolutionary because of its ability to compute stresses in the unique and complex shapes of human bones [22].

FEA begins by subdividing 2D or 3D geometry into many smaller blocks, or finite elements. This subdivision is typically referred to as meshing. Each finite element can then be assigned specific parameters such as material properties and boundary conditions (forces or displacements). The computer can then assemble and solve the system of element specific-stiffnesses, by solving a large number of partial differential equations governing force equilibrium at nodal interfaces [22]. By dividing the geometry into smaller and smaller components the finite element method turns complex structures with no hope for an analytical solution into large arrays of readily solved systems of equations. Smaller and smaller element sizes generally lead to an increasingly accurate representation of real world phenomena. Largely due to improvements in the semiconductor industry, FEA has been expanded to accommodate increasingly complex tasks over the course of its development. It has been extended to involve complex material models, larger model geometries, smaller mesh sizes, multi-scale coupled modeling and boundary conditions. Still, one specifically difficult task for FEA remains the computation of contact between multiple bodies [23].

Contact between two surfaces or morphologies presents a difficult computational challenge because of the inherent nonlinearity of contact between two bodies [24]. There is a complex interplay between deformations of models due to contact forces, boundary conditions, external forces, and how these deformations cause different parts of the model to gain or lose contact [23]. This increased complexity results in significantly increased run times, and numerical convergence issues in the FEA solver, thus significantly increasing the required time investment from the analyst.

The FE meshing step is also often difficult for biomedical problems due to the irregularity of natural surfaces, the requirement for relatively uniform element size, and the specific investigator knowledge needed for FEA mesh generation [25]. The size and shape of the individual elements of an FEA mesh can dramatically impact the quality of the final contact solution, necessitating considerable analyst vigilance. This makes FEA meshing perhaps the most time-consuming portion of the setup procedure for a simulation [25]. Additionally, numerical convergence issues can arise due to irregularities in the mesh or sharp incongruities within the model [12, 23]. Numerical convergence issues may require the FEA mesh to be modified, smoothed or even redone, costing significant analyst time.

The combination of numerical convergence issues in contact, the restrictions of meshing, and the extended run times make FEA unsuited for use in large studies involving hundreds of subjects [26]. This is a significant disadvantage in orthopaedic biomechanics research when taking into account the variability that inevitably exists across subjects. Subject-to-subject variability makes it extremely difficult to draw wide conclusions from any sort of small scale FEA study. To the knowledge of the author, the largest study to date of subject-specific orthopaedic contact FEA models is 11 subjects [12]. Proposed future contact stress analysis studies will likely require at least an order of magnitude larger numbers to achieve appropriate statistical power [7].

2.2 Discrete Element Analysis

2.2.1 Background and Literature Review

Discrete element analysis (DEA) is an alternative methodology to FEA for solving well-prescribed elastic contact problems [14]. DEA relies on a much simplified set of computations relative to FEA, but it is only capable of computing contact forces and stresses between rigid bodies, and is thus unsuitable for any study in which internal stresses or strains are of interest [16]. A wide variety of 2D and 3D DEA algorithms have been created and used in the field of orthopaedic biomechanics for contact between natural surfaces as well as artificial surfaces [15, 17-20, 26-31]. DEA models are primarily used for resolving joint contact forces in larger multi-body dynamic or quasi-static simulations. To a lesser extent they have been used in direct quantification of joint contact stresses [32].

Due to the relative simplicity of a DEA algorithm compared to a present day FEA algorithm, many groups have developed their own purpose-built implementations, primarily constrained to one specific joint or task [18]. All DEA algorithms rely on treating contact surfaces as an array of compressive-only springs connected to their underlying rigid surfaces [20]. A load or displacement is placed on one or all of the bodies in a model and the resulting deformation of the springs is used to compute contact stresses between the bodies [19]. This is typically done in an iterative fashion, in which a matrix of spring stiffnesses is set up and then solved using a minimum energy principle to find final contact stresses and displacements of the bodies [20].

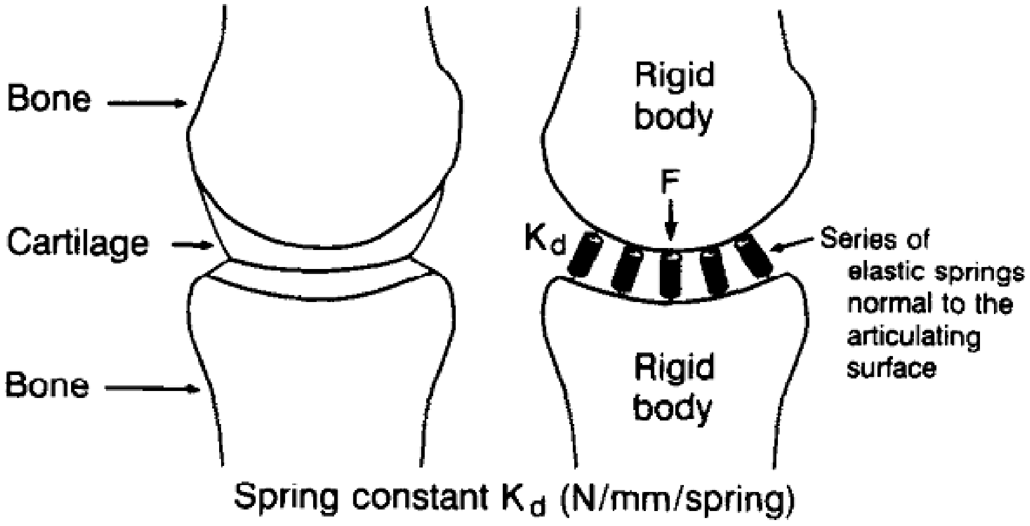

Figure 1. The general concept of rigid body spring modeling. Cartilage is modeled as an array of elastic springs connected to an underlying rigid bone surface. Properties of the springs, such as stiffness and linearity, can be adjusted according to the desires of the investigator. Taken from (Schuind et al. 1995).

An implementation of deformable contact using DEA has been described by Blankevoort et al. 1991 with the assumption that contact surfaces are isotropic, linear-elastic and bonded to a rigid surface [17]. This theory spreads springs over the contact surface, with the springs being treated as the elastic deformable surface. Springs are considered to be independent, so that pressure on a given spring does not affect pressure on any adjacent springs, thus simplifying the integral nature of contact and drastically reducing computation time and complexity [32]. The three underlying assumptions made from this theory are: (1) the size of the contact area is large compared to the cartilage thickness, (2) the cartilage surface is an isotropic linear elastic material and (3) the subchondral bone is considered as rigid [17]. Using this model, spring deformations are related to engendered contact stress using a linear elastic spring equation. Spring deformations using this contact model have been computed using a penetration analysis, in which any apparent overlap between the two apposed contact surfaces is interpreted as indicative of surface deformation [18, 29, 33]. Alternative implementations have incorporated a proximity-based analysis in which the contact surface is implicit and distances between underlying (rigid) subchondral surfaces are computed [19, 20, 31, 34]. This theory has also been extended to use other spring models for large strain, small strain, and nonlinear surface material models to represent native cartilage surfaces as well as polymer surfaces [18, 26, 33].

DEA systems have been validated against both experimental and computational contact stress evaluation methods. Li et al. compared DEA methods to other computational methods such as a modified Hertzian theory, a simplified elasticity solution and a finite element model with a ball in cup geometry suggestive of a hip joint. Contact stress results were found to be comparable between all computational methods, but with DEA predicting 5% higher peak contact stresses compared to FEA across all contact configurations [14]. Deformable FEA was compared to rigid FEA using a pressure-overclosure model which is similar to DEA methods in a natural human knee joint model by Fitzpatrick et al. 2010. It was found that there was a 95% reduction in computational time using the rigid model vs. the deformable model, while the computed contact areas and peak and average contact stresses differed by only 8.3%, 11.2% and 5.7%, respectively [26]. Halloran et al. compared an FEA model and a linear and non-linear DEA in a dynamic knee loading task for a total knee replacement. Computed displacements for the DEA were found to agree well with both experimental and deformable FEA results. Linear DEA modeling was found to consistently over predict the deformable FEA computation by up to 7 MPa at peak pressure, whereas nonlinear DEA was found to have a good reproduction of contact stress results with only slight over prediction for approximately 25% of the gait cycle [33].

Based on previous work comparing DEA models to FEA and to experimental results it is apparent that DEA models can be used to reproduce more complex FEA simulations with acceptable accuracy. Over-prediction of FEA contact forces seems to be characteristic of the majority of reported DEA comparisons, even when measures are taken to tune the spring model results to the FEA [26, 33]. To date no comparison has been done comparing contact stress results for highly incongruous surfaces such as that following articular fracture reduction. Additionally, most comparison studies have been done with a single model. Knowing the assumptions made in performing efficient penetration analysis, a wide variety of models and configurations should ideally be tested to confirm agreement between FEA, experimental, and DEA results. Even though there are significant reductions in computational and investigator time due to the simplification of DEA methods, to date no large-scale (n>20) studies have been done using subject-specific models and DEA methods.

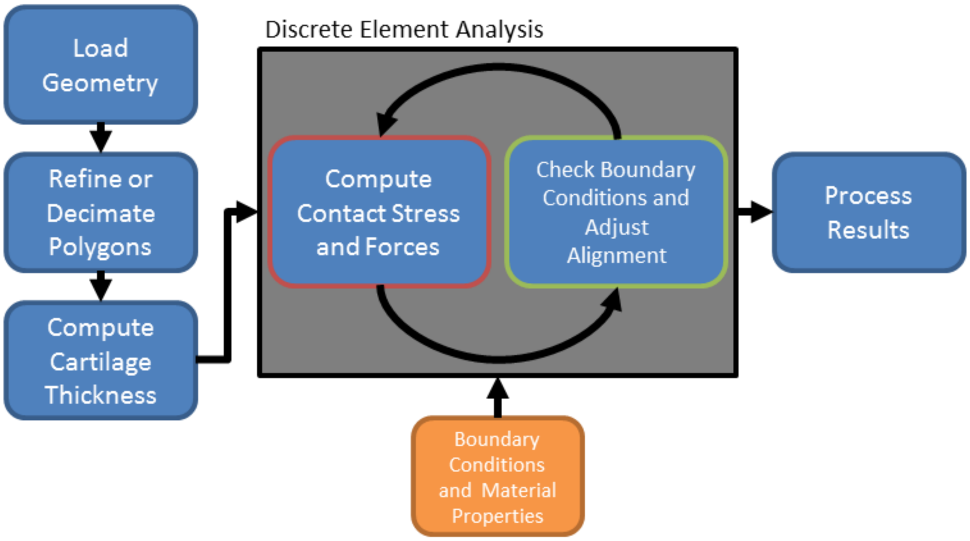

Figure 2. Flowchart of overall DEA methodology. The simulation begins with 3D geometries. These geometries are refined or decimated to an appropriate number of polygons for improved computational performance as well as accuracy of results. Cartilage thicknesses are computed and then input to the DEA algorithm along with user input boundary conditions. The DEA algorithm iteratively computes a contact stress evaluation and then allows for results processing.

2.2.2 DEA Implementation

The current DEA algorithm is implemented in MATLAB (2011a, The MathWorks, Natick, MA). The described methodology requires a model preparation step involving segmentation from a source medical imaging dataset, decimation/refinement of the model, cartilage thickness computation and alignment of the model to a functional apposition. Following this preparation step, model loading/displacement conditions are input by the user and the model is analyzed using the DEA method (Figure 2).

2.2.2.1 Simulation Preprocessing

Preparation for the DEA method begins with model creation from source 3D imaging data, namely CT or MRI data. Models can be segmented manually or through an automated or semi-automated system. Ideally the cartilage surface can be directly segmented from the source 3D image, leading to a direct representation of the subject-specific model. CT imaging and low B_0 field strength MRI modalities, however, do not allow for accurate cartilage segmentation. This necessitates segmentation of the underlying bony surface and then an extrapolation to represent the cartilage surface. Final representations of these models are stored as a triangulated polygon surface in a face-vertex mesh representation. This representation consists of a list of vertices and faces. The vertex list contains three-dimensional Cartesian coordinates for every vertex in the model. The face list contains sets of three indices to the vertex list, with each set of vertices representing a face on the surface stored in clockwise winding order. This is a simple and efficient method of storing surface model representations, which allows for simple calculation and traversal of the mesh as long as no triangle adjacency data are needed [35].

Initialization for contact analysis between two contact surfaces also needs to account for proper alignment between the contact surfaces and mesh density. Contact surfaces in biological applications are typically represented by a segmented or extruded cartilage surface. The contacting surfaces need to be aligned such that they are unloaded or barely touching, for proper contact force calculation if they are to be run exclusively in load control. To be run in displacement control, the contact surfaces must be in their final loaded apposition. The surfaces also must be in an apposition relative to one another which is representative of either a subject-specific or a nominal functional loading task, to achieve meaningful contact stress results [36]. This alignment can be done either through manual expert alignment, or through a computer guided semi-or fully-automated approach. Ideally a computer-aided alignment approach can be used to align 3D datasets to a subject-specific loading apposition.

Prior to contact stress computation, the cartilage thickness must be known for each contact surface. If the quality of the 3D source data set does not allow segmentation of the contact surface directly at this step, a cartilage surface can be extruded from the underlying bone surface to a nominal representative thickness. In its most simple form uniform shell can be extruded from an underlying bony surface to represent cartilage of a uniform thickness. More detailed irregular cartilage thicknesses can also be accommodated if both the contact surface and an underlying bone surface are available from the segmentation step. The contact surfaces are required to be aligned in an appropriate physiological position with respect to one another. Next, the measurement is performed by computing a nearest neighbor search on the entire collection of cartilage contact surface faces to all of the underlying bone surface faces. A list of these distances is stored in memory for later use in the contact stress algorithm.

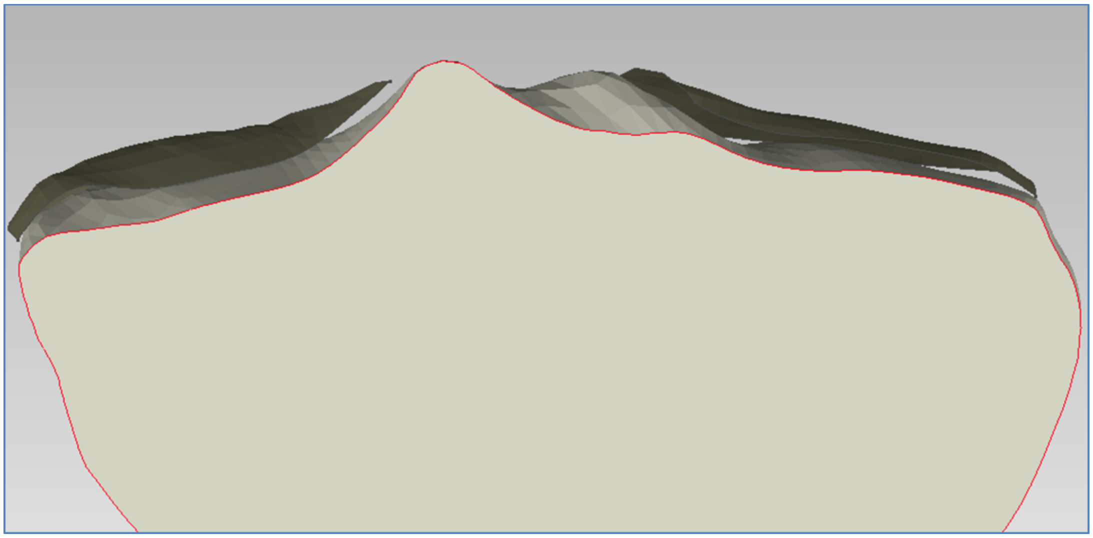

Figure 3. Cross section of tibia bone (cream color) and cartilage articular surface (black color) models. Thickness is computed for each facet on the articular surface by performing a distance transform between the articular surface and the bone surface.

The DEA algorithm requires as inputs (1) two aligned and triangulated cartilage surfaces with a corresponding cartilage thickness value for each facet, (2) desired loads, (3) displacements, (4) termination constraints for the model, and (5) desired kinematic constraints such as joint flexion or springs. One surface is designated the master surface by the user and another is designated as the slave surface. The master surface is constrained to have one contact spring for each individual facet on the surface, whereas the slave surface does not have this constraint. This allows for accommodation of mismatches in the relative decimation or refinement of the contact surface meshes. Additionally, contact stress reporting is performed with respect to the master surface.

2.2.2.2 Discrete Element Analysis Algorithm

The DEA system implemented consists of a pair of rigid contact surfaces lined with a system of linear springs designating contact points. The simulation progresses as a series of iterative static solutions. Within each iteration contact stress is computed at the current joint position, reaction forces are computed and the solution is tested for the satisfaction of termination constraints. A load balancing routine then incrementally adjusts the displacement of the joint, and an additional iteration is performed. This is continued until termination constraints of the simulation have been met (typically force/moment equilibrium).

Each iteration begins with the assumption that there is no contact and that no springs are connected between the surfaces. Apparent overlap is then detected between the contacting surfaces, and a system of springs is assembled over these contacting regions. The deformed length of these springs then relates to the engendered contact stress in each facet of the contact surface. A single iteration of the contact solution is solved by the following steps: (1) efficiently select nearest neighbors between polygon centroids on contact surfaces, (2) create a spring system between nearest neighbors, (3) correct spring displacements to normal projections, (4) compute contact stress between remaining springs, and (5) determine forces engendered by contact stress.

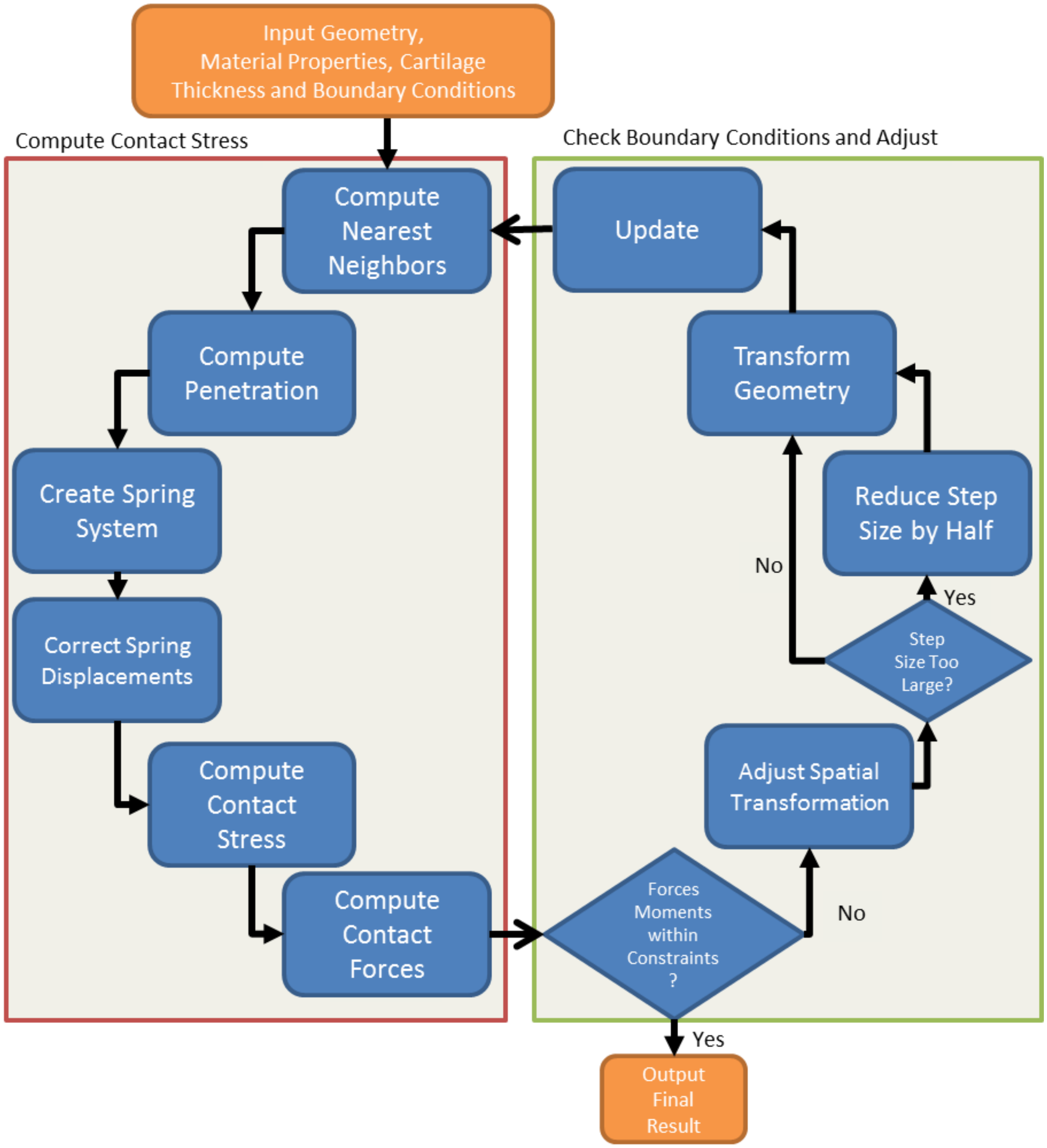

Figure 4. Flowchart of DEA algorithm where subject-specific geometries, material properties, cartilage thicknesses and boundary conditions are input to the algorithm. Through an iterative process contact stress is computed using a penetration computation and balanced using a simple load control algorithm until final termination criteria are met.

Efficiently Select Nearest Neighbors:

To accurately detect contact between two surfaces, adjacent polygons on the opposing surfaces must be found. This distance measurement is typically the most time-consuming step in contact simulations. Thus, selecting an accurate and computationally efficient method is critical [18]. The selected approach assumes that each polygon is small enough to be represented by its centroid. Each contacting surface can thus be represented as a cloud of centroids, nearest neighbors are then found using a nearest neighbor algorithm.

Nearest neighbor (NN) searching a classical problem in many disciplines of computer science [37]. Given a set of n data points, (P) and a query point (q) to the goal of an NN algorithm is to find the point within P which has the smallest spatial distance to q. The most common and easily implemented method is a naïve approach in which the distance between a query point q and a set of test points P is explicitly calculated for all points in P, and then the minimum distance pair is selected.

$$NN = \min_{i=size(B)} (dist(q, P_i))$$

This algorithm unfortunately scales poorly with increasingly large data sets and requires significant computational time, as its solution can be performed in O(dn) time, where d is the dimensionality of the space containing P [37].

Another solution to finding nearest neighbors is to use a space partitioning tree [38]. Space partitioning trees are used widely in the fields of computational geometry and computer graphics to accelerate geometrical algorithms. Space partitioning algorithms are capable of making the nearest neighbor algorithm scale in O(log(n)) time which is a significant reduction from the naïve approach at O(dn) time [37]. There are a wide variety of space partitioning algorithms available, all of which achieve the goal of creating a hierarchy of increasingly specific volumes containing smaller numbers of query points [39]. This enables a space partitioning tree to occlude large numbers of possible nearest neighbor candidates quickly and reduce the total of number of distance calculations performed.

Voronoi diagrams, another important fundamental computational geometry algorithm, are also useful for performing NN searches [40]. A Voronoi diagram describes the space surrounding a set of points, P, by dividing the space into a set of unique regions for every point in P. Each region in the Voronoi diagram describes the space which is nearest to its associated point in P. By definition, if a query point q lies within a specific region of a Voronoi diagram then it is nearest neighbors with that region's associated point in P [40]. It has been shown that Voronoi diagram NN searches can achieve computational times scaling with O(log(n)^2) [37].

A number of these algorithms were implemented and tested in MATLAB to determine the most efficient method. A brute force, space partitioning tree (k-d tree) and Voronoi diagram algorithm were each tested on sample point cloud data representative of contact surface geometries and point densities (Table A-1) [41]. One important aspect of the kd-tree and Voronoi diagram algorithms is that they require pre-computation of a data structure prior to any NN search. The time required to compute these data structures was also recorded. The Voronoi diagram algorithm was selected due to the fact that it is a native MATLAB algorithm based off the Qhull libraries, and due to its having the best performance across all numbers of points tested [41]. The MATLAB function used is listed as **dsearchn** in the MATLAB documentation.

The selected algorithm requires the pre-calculation of a spatial geometric triangulation prior to performing NN searches. This triangulation is performed in the initialization step of the DEA simulation immediately after loading model data, and is stored in memory for the duration of the contact simulation. The set of points on the master contact surface are used as query points, and the set of points in the slave surface are used in the initial triangulation, ensuring a computed neighbor for every point on the master surface.

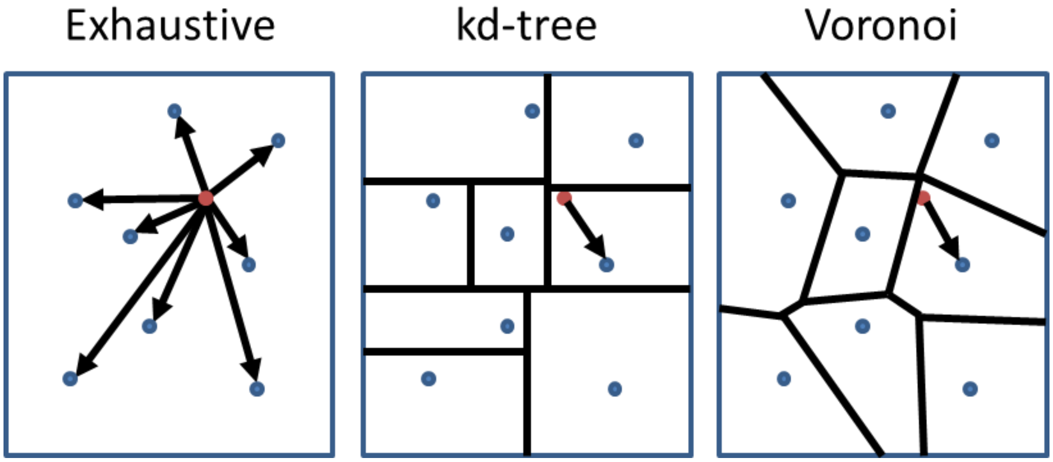

Figure 5. Diagram of different methods of computing nearest neighbors between a set of points (blue) and a query point (red). An exhaustive search computes the distance between all points in both query and data points. A kd-tree implementation subdivides the data point set into increasingly more specific spatial domains allowing for fast searching of the points. A Voronoi diagram creates specific regions in space which correspond to points in the data set that designate the space closest to its corresponding point.

Create Spring System Between Nearest Neighbors

Once nearest neighbors have been identified it is necessary to determine which polygons to include in DEA calculations. Springs are generated only for the polygons of the contact surfaces which have undergone apparent penetration. Penetration state is determined by computing the sign of the dot product of each polygon’s outward-pointing normal and the vector connecting the two polygons paired in contact. In Figure 6 it is shown that if the surfaces have penetrated the sign of the dot product will be negative, whereas if they have not penetrated the sign is positive. If the contacting surfaces are large and have many tortuous geometric features this methodology can produce incorrect contact patches. A minimum distance threshold can be added to cull additional points which are not candidates for contact.

To avoid selecting a minimum distance threshold and any ambiguity surrounding the selection of such criteria, geometry specific penetration criteria can be created.

Certain contact surface geometries allow for alternative purpose-written penetration algorithms. For example, contact between distal the tibia and talus can be roughly modeled as two superimposed cylinders. Distance can be computed between the center of mass of the talus cylinder and all points on the tibia and talus. The distance to the talar surface will be less than the distance to the tibial surface in all NN pairs which have not undergone apparent penetration (Figure 6).

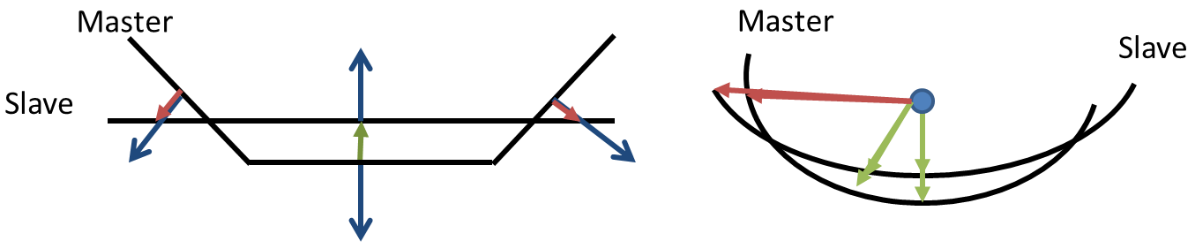

Figure 6. Two methods of determining overlap between two contact bodies. The general method on the left determines agreement between the master surface normal vectors (blue) and the spring direction (red, green). A specific method on the right allows for contact detection on conformal surfaces resembling cylinders. If the distance from the slave surface to the master centroid (blue) is greater than the distance from the master surface to the master centroid then the surface is determined to be in contact. Springs in contact are shown in green; springs not in contact are shown in red.

Correct Spring Displacements

Following creation of the spring system and detection of regions which have undergone apparent penetration, the contact solution appears as an array of springs connecting the master surface to the slave surface (Figure 7). The spring model used in this algorithm assumes the stresses computed on each polygon are exclusively normal to the polygon face [17, 18]. Due to the fact NN pairs are computed using centroid-to-centroid distance and that many springs from the master contact surface may connect to a shared spring on the slave contact surface, a correction needs to be performed to adjust spring directions and lengths to match the normal direction of each master surface polygon. Otherwise the dichotomy between the normal direction of the master surface facets and the contact spring direction may cause aberrant contact stress distributions that have a "mottled" effect, as well other erroneous results (Figure 8).

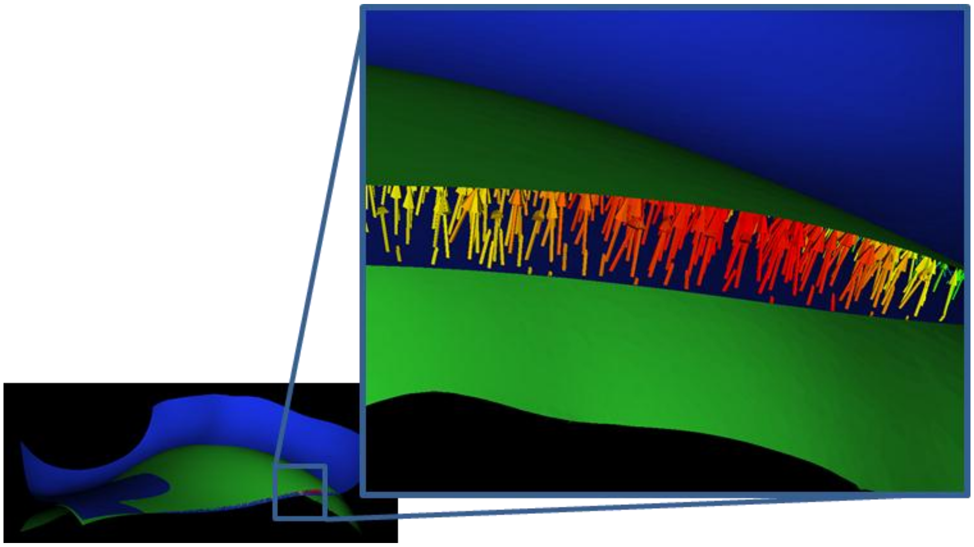

Figure 7. Rendering of spring system established between two contact surfaces. Master surface (blue) has a unique spring assigned to each face connecting to a face on the slave surface (green).

A correction is performed by projecting the spring displacement vector along the normal vector of the polygon. This is done using a dot product between a unit normal vector and the spring vector to compute the new displacement of the contact spring.

$$S' = dot(norm(N), S)$$

Where S is the original spring vector, N is the normalized facet normal and S′ is the projected spring direction. This projects all of the springs in the normal direction of the contact surface and helps to correct aberrant contact stress patches.

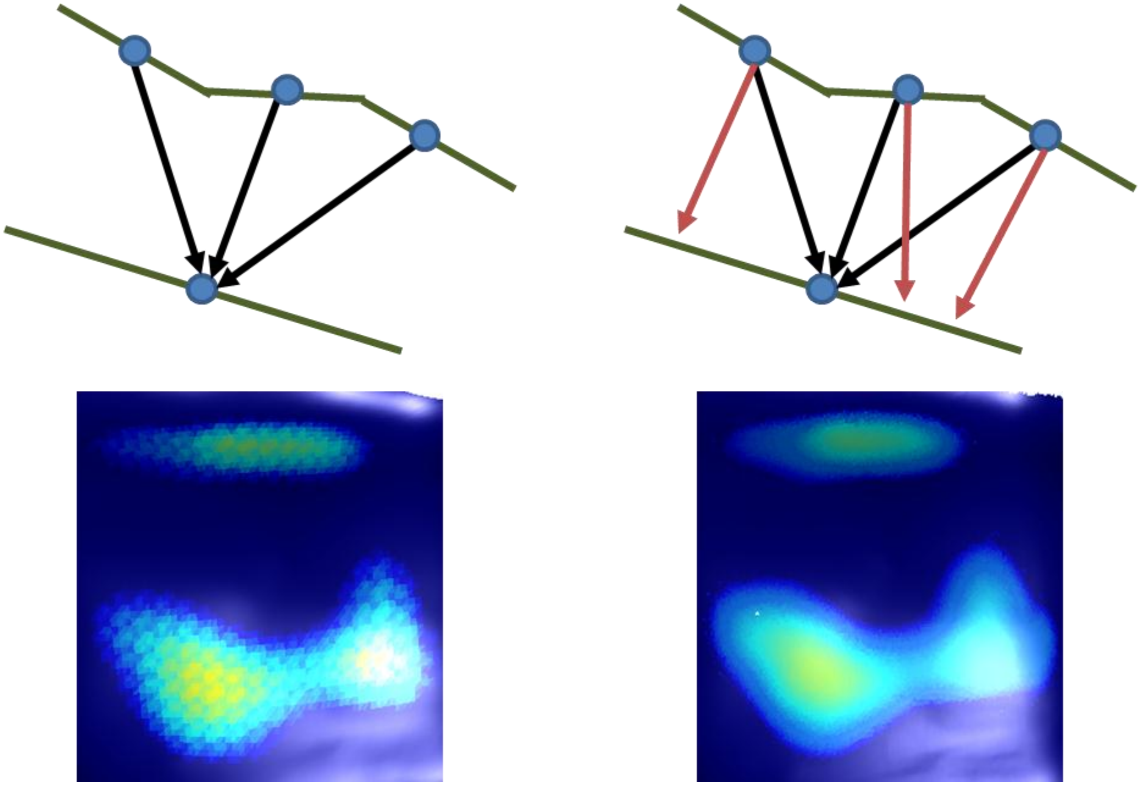

Figure 8. Demonstration of contact stress distributions without spring correction (left) and with correction (right). Pre-correction springs are displayed as black and post-correction springs are displayed as red.

Compute Contact Stress between Surfaces

Once the system of contacting springs has been determined and corrected, contact stress can be computed between the surfaces. A force-displacement spring model is used which relates the spring deformation, (d) effective cartilage thickness, (h) Young's modulus, (E) and Poisson's ratio, (v) to the engendered contact stress, (p) [17].

$$p = \frac{(1-v)E}{(1+v)(1-2v)}\frac{d}{h}$$

This contact stress value is calculated for each facet on the contact surface. The effective cartilage thickness is obtained from the preprocessing prior to DEA simulation and can be either face-specific or a uniform value for each contact surface. The thickness, h, is calculated as the combination of the cartilage thickness value assigned to each face associated with a spring. Spring deformation, d, is represented effectively by the corrected distance between each NN pair, since the contacting surfaces are used, and underlying bone surfaces are implicit.

Compute Forces Acting on Contact Surfaces

Contact pressure and associated polygon area are used to find the discrete contact force contributions acting over each individual facet of the contact surface. The contributions are vectorially summed to find a total contact force and moment vector acting over the entire contact surface. This vector is computed with respect to the centroid of each surface and is an output from the DEA algorithm. This is later used either in the iterative load control algorithm.

2.2.2.3 Iterative Load Control

Purely displacement-driven contact stress simulations are of limited utility in many applications, due to the exquisite sensitivity of contact to small displacement changes and the difficulty of precisely registering 3D models to loaded appositions [36, 42]. Alternatively, using load control allows two contacting surfaces to seat and adjust into kinematically suitable force equilibrium. It also allows for a wider variety of simulation and validation work to be performed. The loading algorithm implemented in this DEA is an iterative cycle of quasi-static poses in which a simple optimization algorithm is used to find force and moment equilibrium, subject to appropriate tolerances (Figure 9)

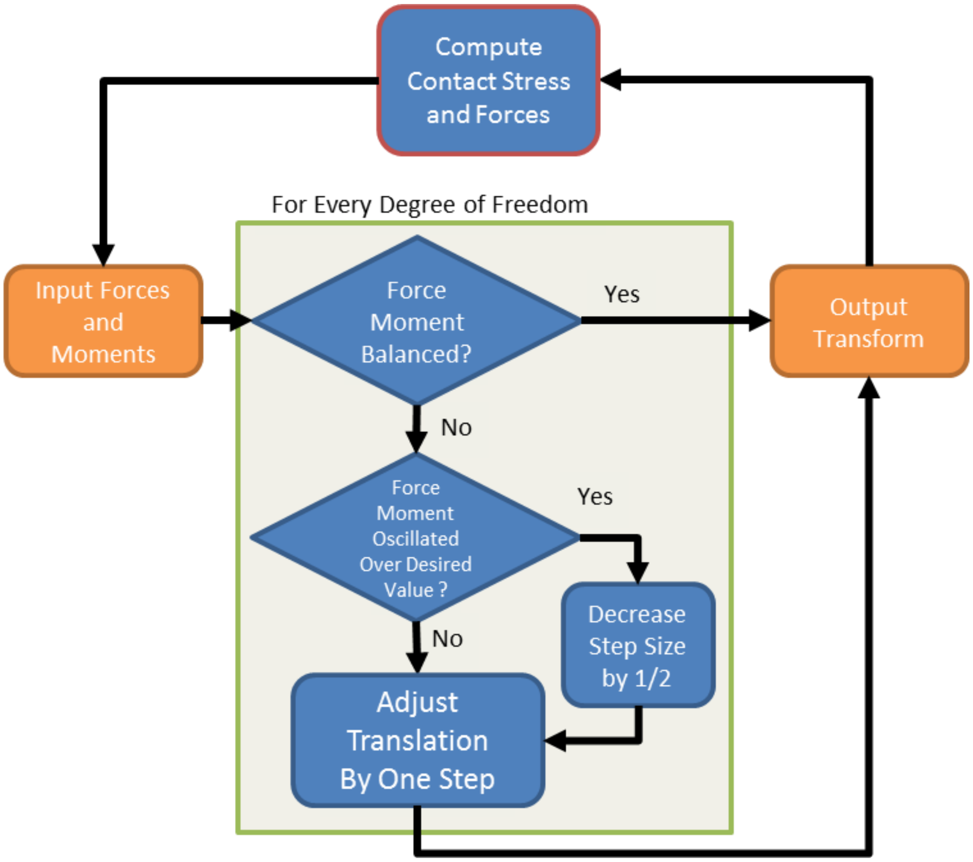

Figure 9. Flowchart of iterative load control system which adjusts translations and rotations to drive the DEA algorithm to equilibrium. Step sizes for each translation are reduced appropriately once the system has been found to oscillate about the desired termination criteria.

Prior to simulation, the user-input tolerances and loads are defined for all six degrees of freedom for each model, and independent step sizes for translations and rotations in all six degrees of freedom are input. For each iteration of the contact stress algorithm, forces and moments are input to the load control optimization algorithm. This algorithm checks these forces and moments against boundary and loading conditions. If a force or moment meets the equilibrium requirements, then no transformation or alteration is made to the corresponding positioning in space. However, if the tolerance criteria are not met, then a corresponding rigid affine spatial transformation is applied. The magnitude of all transformations corresponds to the associated step size for that deformation.

After a number of iterations, the simulation will find itself ‘oscillating’ around the desired loading value due to a larger than optimal step size. If the loading value for the simulation ‘oscillates’ around the desired loading for four consecutive iterations then the step size is decreased by half. This allows the load control optimizer to start with large displacements for gross adjustment of the surfaces, followed by a gradual refinement of step sizes to a final kinematically suitable position.

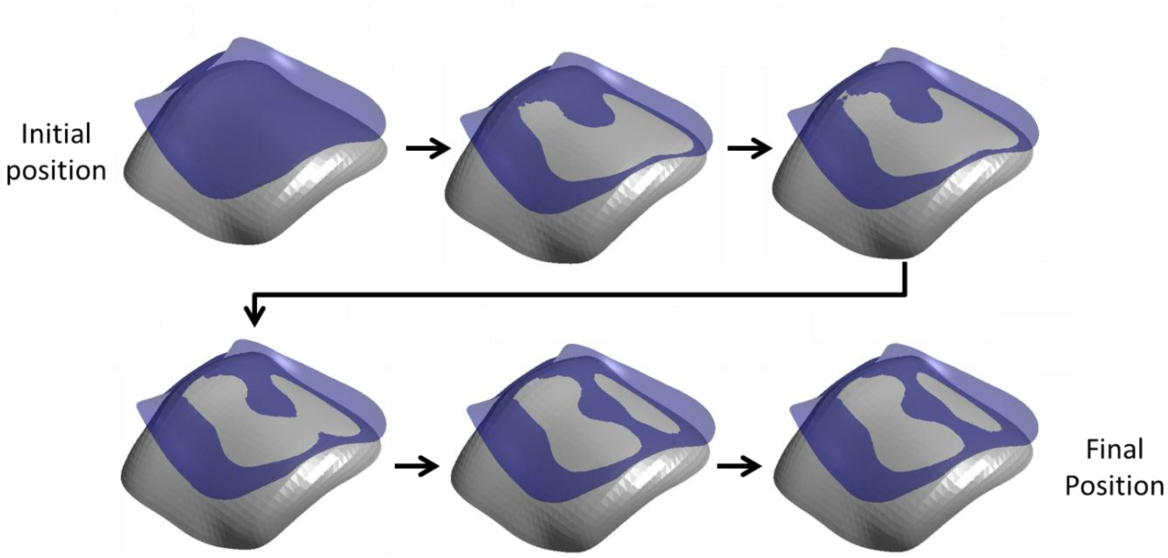

Figure 10. Iterative load control settling algorithm progression from starting apposition to final balanced apposition.

2.2.3 Physical Validation

2.2.3.1 Validation Setup and Procedure

The DEA algorithm discussed was used to replicate a previous FEA cadaver ankle validation study [13]. In that study a purpose-built mechanical apparatus had been used to examine contact stress distributions in two human cadaver ankle joints using a Tekscan ankle sensor to gather contact stress data (Tekscan, Inc., South Boston, MA) (Figure 11). Following physical contact stress measurement, the ankles had been fixed and CT scanned. FEA models were created from the CT data and a validation performed between the FEA and the physically recorded contact stress results.

The FEA models, displacements and material properties from this previous study were presently adapted for use with the DEA. The articular surfaces of the FEA model for both the tibia and the talus were extracted as quadrilateral faces. These quadrilateral faces were then each bisected to form two triangular polygons. Cartilage was treated as linear elastic material with uniform thickness of 1.7mm, a Young's modulus of 12 MPa, and a Poisson's ratio of 0.42 [13].

The simulation was run in load control in the superior-inferior direction with loads of 600N and with a spring of stiffness 75N/mm applied to the lateral side of the talus, representing stabilization of the fibula. The tibia was constrained in all directions except for superior-inferior translation and the talus was constrained in all directions except for medial-lateral translation. Prior to running the DEA model, the talar polygons were refined into four smaller polygons each, to allow for a more accurate discretization of the talar dome, as well as for more accurate distance computations due to the effective creation of additional sampling points for the DEA model. Contact stress results were then compared between the Tekscan, FEA, and DEA approaches.

Ankle #1 was used in a convergence study for the DEA methodology in which the level of decimation of the original tibia and talus surfaces was varied and compared to the resulting variation in contact stresses and residual forces.

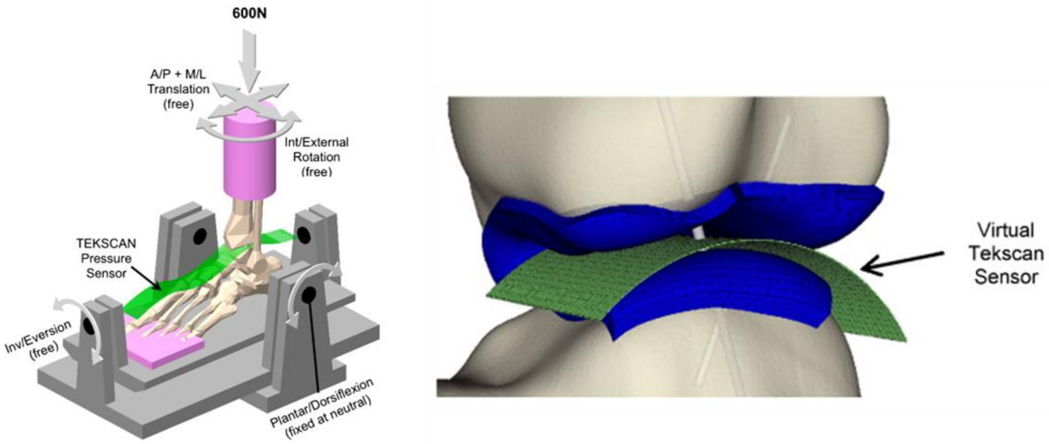

Figure 11. Setup of physical validation study with cadaver ankle and Tekscan sensor to measure contact stress (left). A human cadaver ankle was placed in mechanical fixture to allow for articulation of the joint. A Tekscan ankle sensor was placed between the talocrural articular surface to measure the articular contact stresses. A 600N load was applied axially to the tibia. FEA replication of physical validation with Tekscan sensor implemented in FEA model (right). Figures taken from (Anderson et al. 2007).

2.2.3.2 Validation Results

Validation comparisons were performed for both ankles from the previous FEA study. First, distributions, maximum, and mean contact stresses were compared between the physical testing and the two computational methods. Contact stress distributions and levels were found to be similar for both FEA and DEA methods. Maximum contact stress values were 19% and 2% higher, mean contact stresses were 8% and 37% higher, and contact areas were 1% and 20% lower for the DEA model versus the Tekscan results in ankles #1 and #2, respectively (Figure 12).

Next contact stress from Tekscan ankle sensor was registered to the FEA and DEA models using transformation parameters from the previous study for alignment [13]. Once Tekscan results and DEA results were registered into the same orientation, the DEA contact stress results were mapped to the grid of the Tekscan sensor using an interpolation scheme. This allowed for a direct comparison of Tekscan and DEA results.

Differences between contact stresses in the DEA and the physical results were quite small over the majority of the contact surfaces, with most of the larger discrepancy (>1.5 MPa) occurring on the periphery of contact (Figure 13).

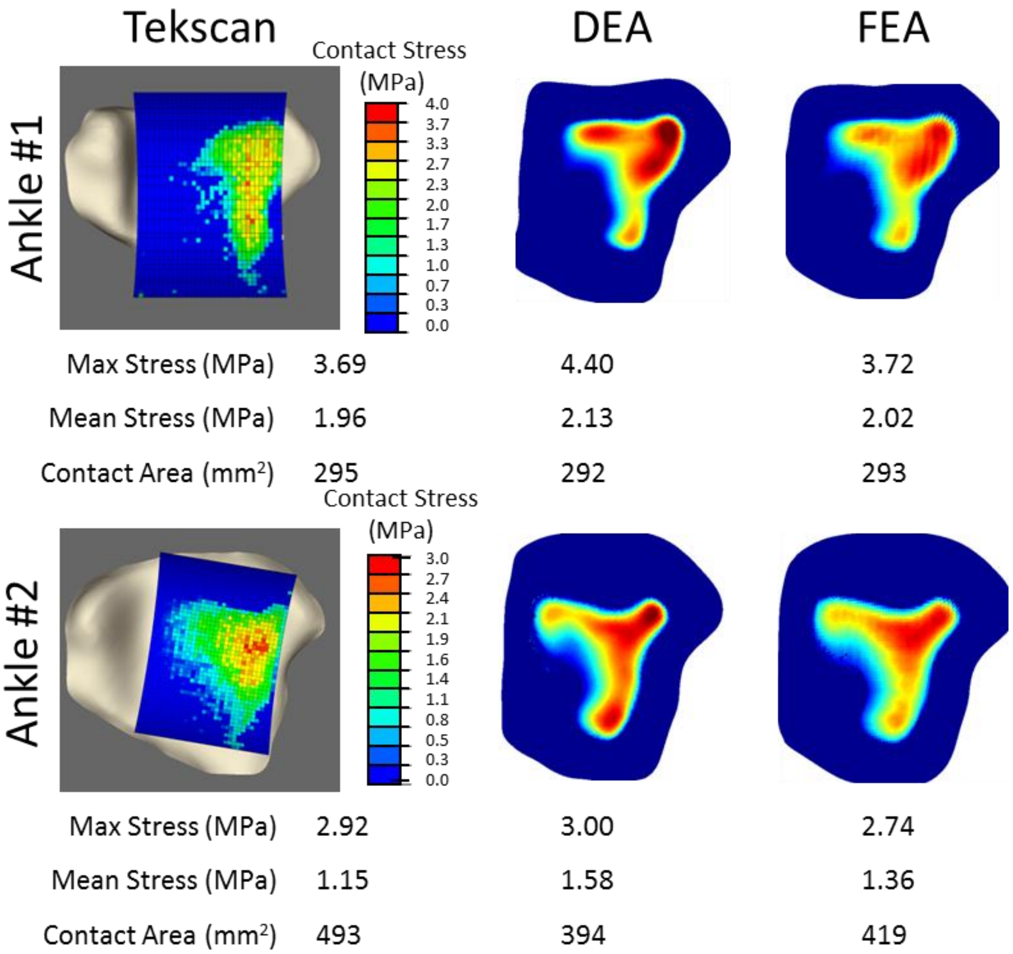

	Tekscan	DEA	FEA
Ankle #1			
Max Stress (MPa)	3.69	4.40	3.72
Mean Stress (MPa)	1.96	2.13	2.02
Contact Area (mm^2)	295	292	293
Ankle #2			
Max Stress (MPa)	2.92	3.00	2.74
Mean Stress (MPa)	1.15	1.58	1.36
Contact Area (mm^2)	493	394	419

Figure 12. Resulting contact stress distributions from the physical validation study displaying Tekscan contact stress distributions along with DEA and FEA contact stress distributions. Maximum and mean contact stresses are reported along with total contact areas.

When observing only portions of the surface which are undergoing contact, differences between the Tekscan and DEA methods fit a normal distribution, centered about zero. The probability that the differences between Tekscan and DEA derived contact stress were less than 1.00 MPa was 91% for ankle #1 and 90% for ankle #2, with correlations coefficients of 88% and 81, respectively (Figure 14).

Run times for the DEA model were 1.3 minutes for ankle #1 and 1.5 minutes for ankle #2.

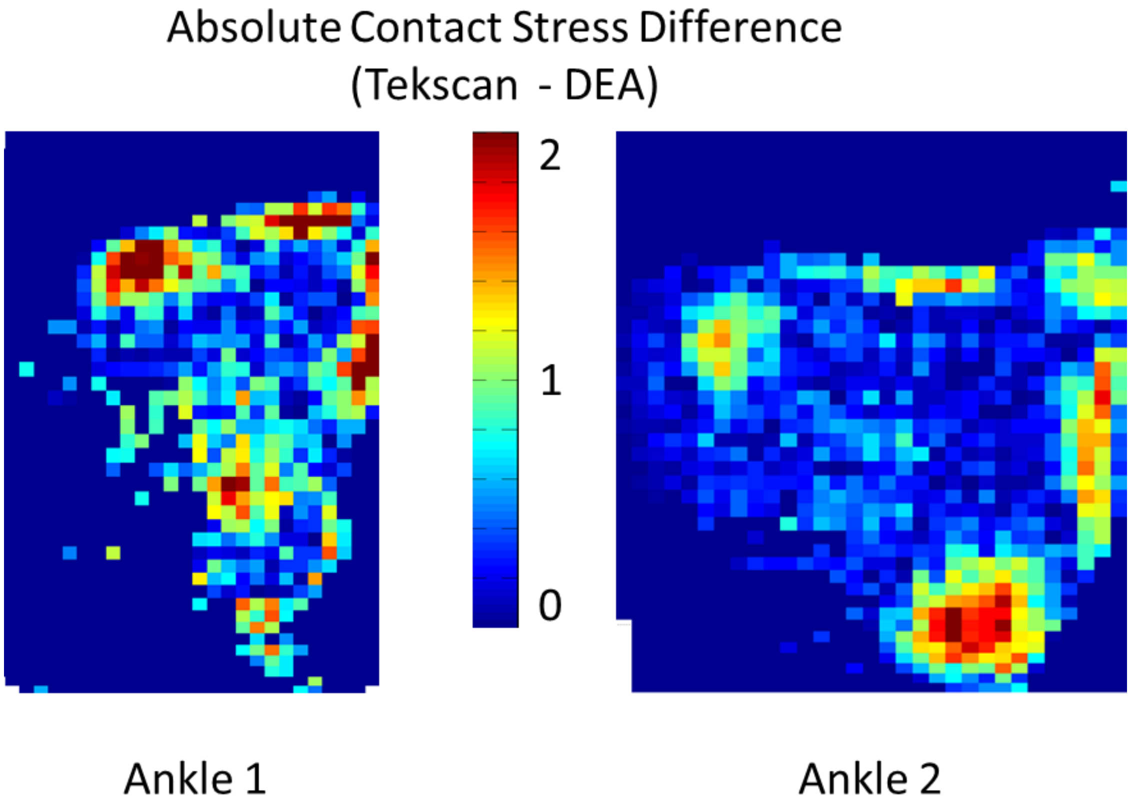

Figure 13. Contact stress differences between Tekscan sensor and DEA-computed contact stresses measured in MPa. Tekscan sensor was registered using k-wire marks from physical validation. DEA contact stresses were then interpolated and mapped to a grid representing the Tekscan sensor. DEA stress was then subtracted from Tekscan stress on a sensel by sensel basis.

	Probabilities of Agreement in Contact (measured-computed)				Correlation Coefficient
	< 0.25 MPa	< 0.50 MPa	< 0.75 MPa	< 1.00 MPa	
Ankle 1	21%	80%	85%	91%	88%
Ankle 2	33%	79%	87%	90%	81%

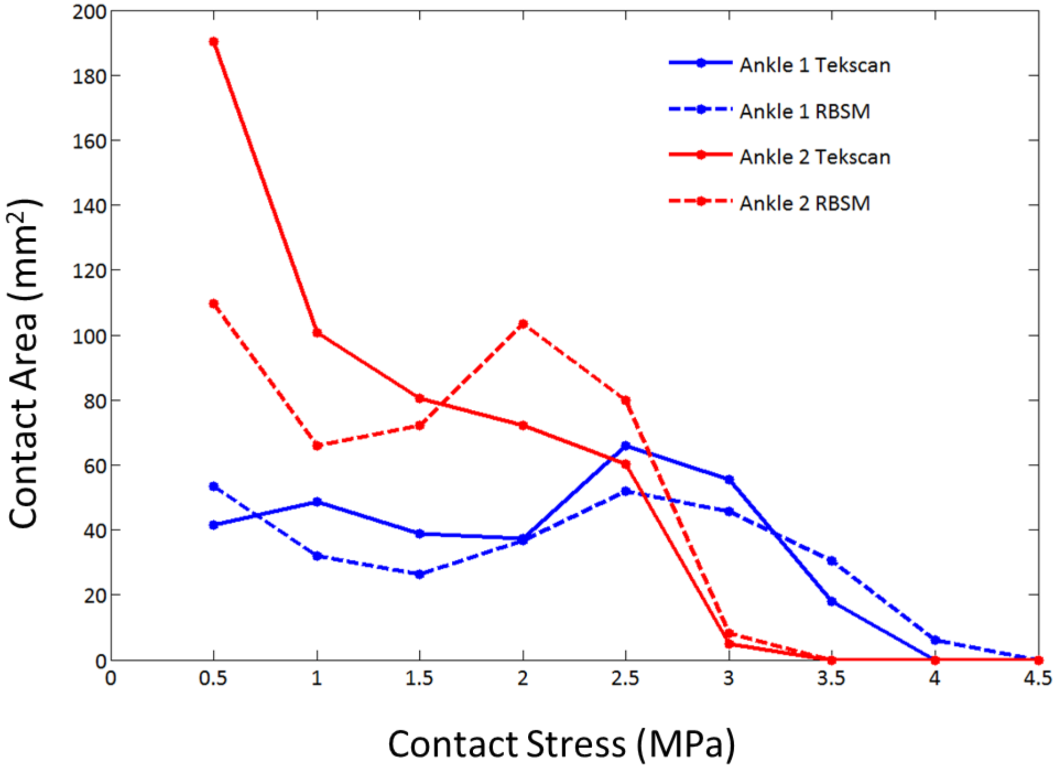

Figure 14. Statistics involving node by node contact stress differences between DEA and Tekscan results (top). Probabilities of agreement are computed for 0.25, 0.50, 0.75, and 1.00 MPa contact stress difference magnitudes on a sensel by sensel basis. Correlations are also computed between the two contact stress distributions. An area-engagement histogram (bottom) is used to show the relationship between the Tekscan and DEA results with respect to the amount of total area which is undergoing a specific level of contact stress.

2.2.3.3 Validation Discussion

The results of this study show that DEA methodology can be used in specific cases to expeditiously provide accurate estimations of articular contact stress. This demonstrates the validity of this contact model for the application of providing rapid contact stress measurements at the human articular surfaces. The DEA method provided a reasonable estimate of gross measures such as maximum (within 19% and 2%) and mean (within 8% and 37%) contact stresses, and performed well for spatial measures, as illustrated by point-by-point comparisons of the contact stresses distributions.

Based on visual inspection of the resulting contact stress distributions, (Figure 12) the DEA approach consistently over-estimated contact stress from the Tekscan and FEA results. This is most likely due to the nature of the DEA method when compared to the Tekscan and the FEA. Each element (face) in DEA is independent of its adjacent elements, which may result in higher than normal contact stress estimates due to the fact that adjacent elements are not able to transfer load between one another. In DEA a focal load on one specific face will generate load on only that one face, resulting in higher computed contact stresses in regions which contain abrupt curvature. Conversely in FEA, the deformation of one element has an effect on its adjacent elements, thus more closely mirroring a true physical situation. The ability of the model geometry to deform, and the communication of adjacent elements, results in a mediation of contact stress peaks as well as in slightly larger contact areas.

Differences in the contact stress distributions between DEA and the physical model may also be due to the lack of inclusion of the Tekscan sensor in the computational simulation. The Tekscan sensor is of a non-trivial thickness (0.08 mm) in the context of a contact problem where microns may cause significant changes in contact stress results [36]. Inclusion of such a sensor was deemed to be infeasible in the contact simulations for both FEA and DEA methods, due to the complexity of modeling a highly deformable thin object such as a Tekscan sensor.

The DEA method also tended to under-estimate contact stress in areas of low contact stress, and to over-estimate stress in areas of high contact stress when compared to the Tekscan measurements. This can be seen by the contact area engagement histograms, in which a much larger portion of the contact area is at higher contact stress levels (Figure 14). These diagrams show that a larger share of the contact area for the physical test is engaged at lower contact stress levels whereas in the DEA test a larger area share is associated with higher contact stresses. This may be attributed again, to the lack of transverse buttressing in the DEA model, preventing the areas of high contact stress from deforming inward to allow for a broader contact patch. Lack of a Tekscan sensor being included in the DEA contact stress analysis may have also played a role.

There is also some possibility that some of the discrepancy may have been caused by lack of a complex material model to represent the transient non-linear mechanical responses of natural cartilage. However if it is assumed that for functional activities loading rates are high compared to the characteristic relaxation time of cartilage, and that the surface of cartilage is nearly frictionless, many of the visco-and poro-elastic properties of cartilage would not have a large effect on resulting contact stress [11, 12, 15-19]. In the future, it would be possible to explore additional spring model formulations which could incorporate non-linear material properties and/or even small deformations of the surface. For example, a non-linear formulation could be used in a surface which experiences high deformation or for a surface which experiences transient changes in material properties [26, 42].

Based on the results of this validation, the DEA model has been shown to predict the Tekscan measurements within a reasonable level of accuracy (88% and 81% correlation coefficient; 91% and 90% probability that contact stress difference is below 1MPa), and errors tend to be predictable when compared to both FEA and physical testing. DEA’s max and mean contact stress tend to be higher than either the FEA or the physical testing contact stress, due to the simple material model, and lack of a deformable surface. This over-estimation of max contact stress tends to occur at areas of high curvature, which may indicate that in future cases with fractured ankles, that the DEA method will over-estimate contact stress values to a greater extent.

CHAPTER 3: APPLICATION I - CONTACT STRESS EVALUATION IN THE HUMAN ANKLE

3.1 Ankle Introduction and Motivation

3.1.1 Ankle Anatomy

The human talocrural joint effectively involves three bones; the tibia, the talus and the fibula (Figure 15). The distal tibia articulates with the superior dome of the talus by a combination of rotation and sliding movements [43]. These articular surfaces can be roughly approximated as two co-axial cylinders (of slightly different radii) rotating as a modified hinge. The ankle joint is also known as a “mortise,” due to the way that the articular surfaces of the tibia and fibula form a mortise within which the “tenon” or talar dome seats. The medial malleolus of the tibia and the lateral malleolus of the fibula serve to stabilize and bound lateral motion within the joint, while the natural curvature of the tibial plafond supports the joint in the AP direction [43].

As the tibia articulates with the talus, the rotational axis of the joint is aligned more or less along a line between the lateral and medial malleoli. The stability of the joint is primarily attributable to the mechanical influence of the congruent articular surfaces when the joint is undergoing passive flexion and extension actions [44].

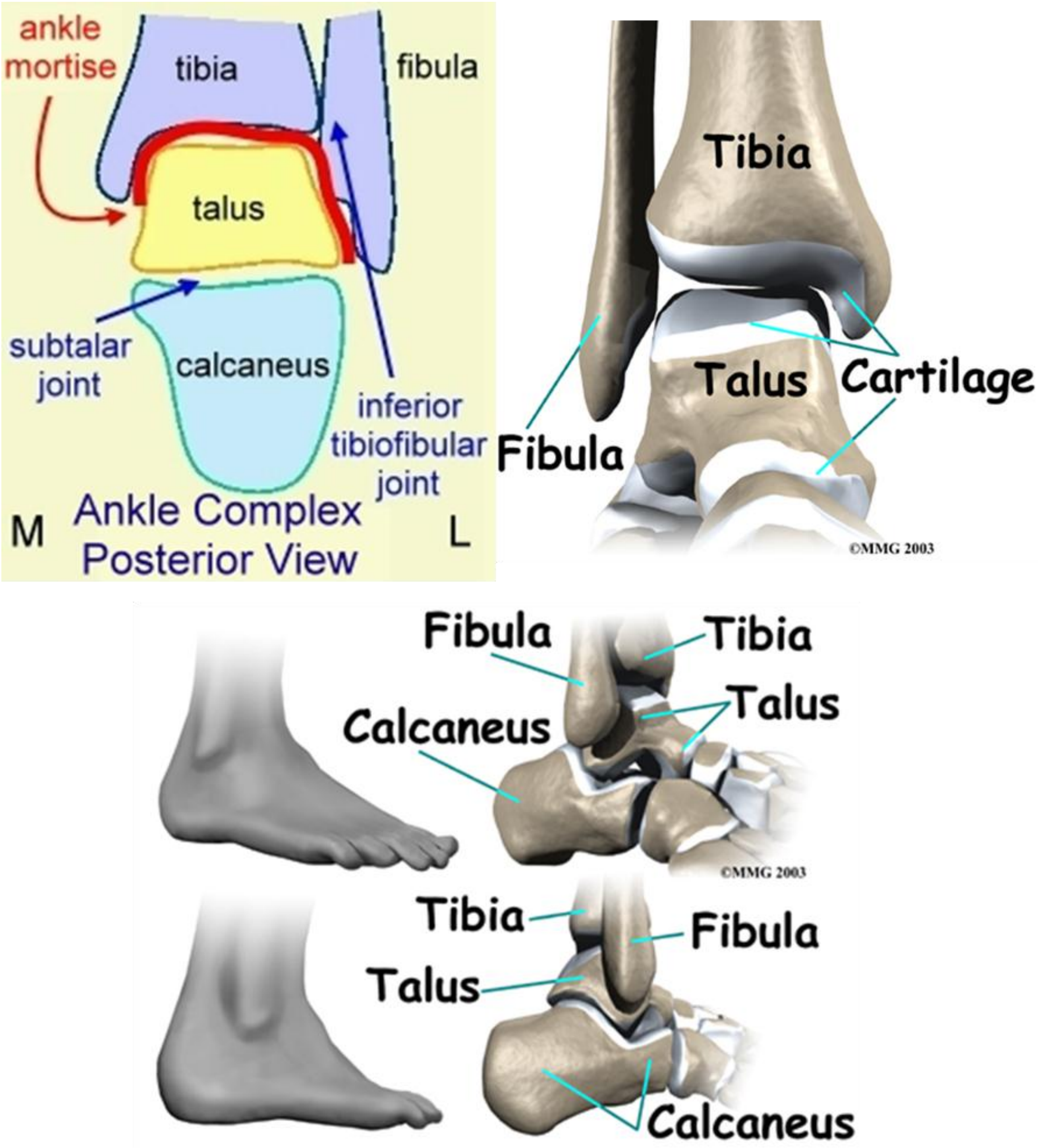

Figure 15. Anatomy of ankle joint showing fibula, talus and tibia. Two dimensional representation (top left) shows the talus seated in the mortise of the tibia and fibula [45, 46].

Cartilage thickness distribution is another important biomechanical factor in the behavior of the talocrural joint. In a study of twelve cadaver ankles performed using stereophotogrammetry, it was found that the cartilage thickness distributions over the talar articulating surfaces are relatively uniform, with slightly thicker regions toward the medial and lateral edges of the talar dome [47]. The tibia has a slight cartilage thickness gradient from anterior to posterior, with the anterior portions having the greater thickness (Figure 16) [47]. Cartilage thicknesses were measured in the distal tibia and talar dome using 5.3mm diameter bone plugs extracted from five human cadaver ankles by El-Khoury et al. It was found that cartilage was relatively thin in the ankle, ranging from 0.4 to 2.1 mm, centered on approximately 1.7mm. By comparison, the human patella has 2 to 3 times the cartilage thickness of the ankle [48].

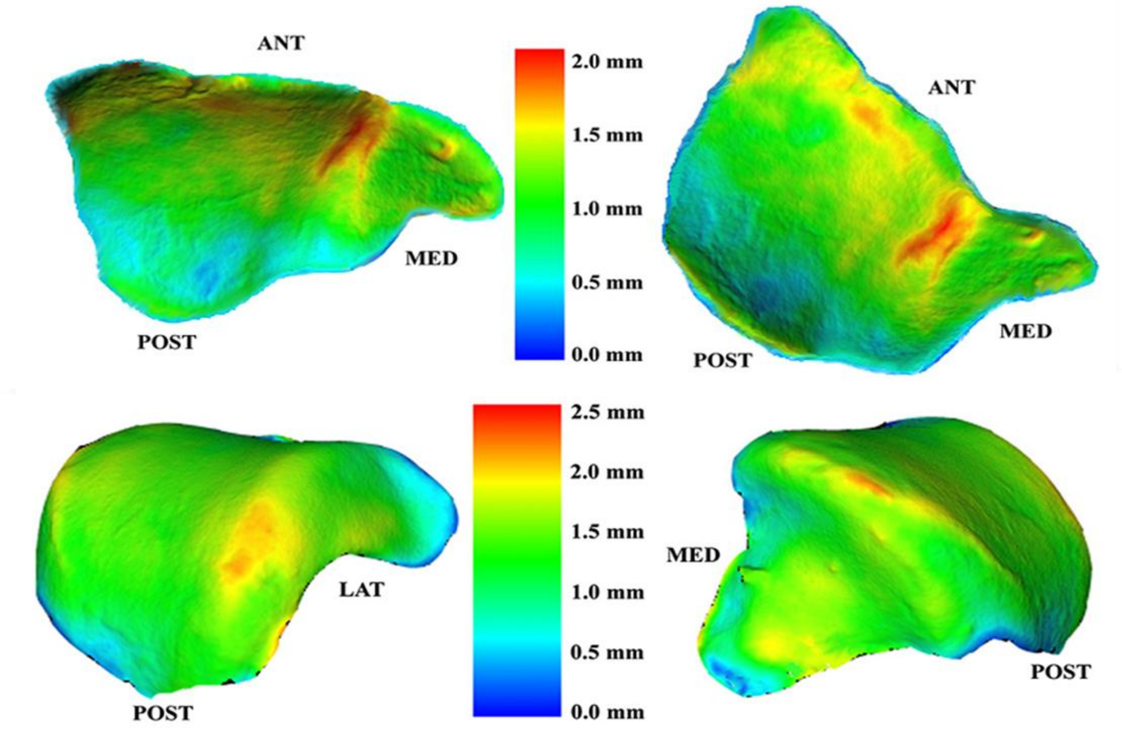

Figure 16. Stereophotographically derived cartilage thickness distributions for the tibia (top) and talus (bottom) [47].

3.1.2 Posttraumatic Osteoarthritis of the Ankle

Posttraumatic osteoarthritis (PTOA) is a manifestation of OA following significant joint injury. It differs from primary OA in that it is much more prevalent in younger (< 60 years) patient populations where typical treatments (joint replacement) for OA are less desirable [3]. This provides an impetus to develop new treatment strategies to provide improved patient outcomes in cases where joint replacement is an undesirable option. Although many studies have established a strong correlation between joint injury and PTOA risk, little is known about the underlying mechanical and biological factors influencing its progression [1, 3, 7].

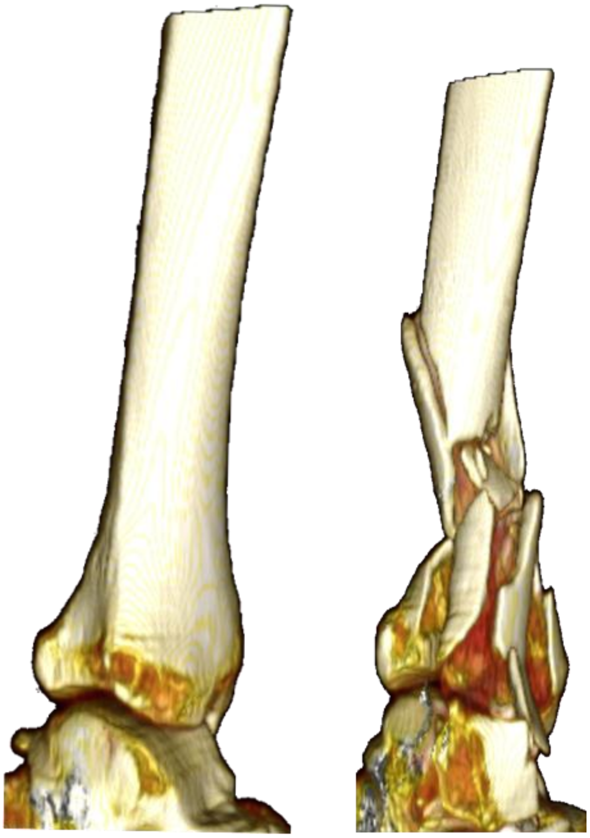

Figure 17. Tibial pilon fracture in which the intra-articular surface is disrupted (right) compared to its intact contralateral (left).

Articular cartilage is an avascular tissue that has limited potential for long-term repair following disruption [3, 7]. It is highly resistant to blunt impacts, with threshold stress values for damage reported to be as high as 25MPa [49]. Following damage, cartilage attempts to mount a reparative response but the tissue produced does not accurately replicate the complex structure of normal articular cartilage, and it has been shown to break down fairly quickly (1-2 years) in the ankle [7].

Incongruities on the articular surface have also been shown to cause substantial increases in contact stress. Brown et al. showed that step-offs of over 3mm caused up to a 75% increase in articular contact stress, measured using pressure sensitive film in studies of the cadaveric human proximal tibia [50]. The relationship between step-off size and contact stress elevation was highly variable between specimens. There was also observed an inverse relationship between cartilage thickness and contact stress levels [50]. This suggests that injuries with similar levels of incongruity could have different levels of contact stress, and therefore different levels of risk for joint degeneration [7].

Mechanical factors such as fracture energy absorbed, joint incongruity and joint instability are all implicated in the development of PTOA [3, 7]. The main conundrum involving these mechanical factors (apart from challenges in measuring them *in vivo*) is that they are closely interrelated. Studies have been performed using a rank ordering methodology employed by experienced clinicians to rank fracture severity based upon a series of tibial plafond fracture radiographs [51]. The same group of clinicians was then asked to rank the same set of fractures following surgical reduction, according to the quality of the reduction [51]. It was found that rankings for reduction and fracture severity were closely interrelated. Specifically, ankles which had high injury severity rankings also had poor fracture reduction rankings [51]. A joint which receives a high level of energy from a fracture will have a much higher level of articular comminution, making for a more difficult surgical repair. There was also no ability for these studies to separate the variables of acute injury severity and poor articular reduction [51].

Understanding and separating the roles of acute injury severity and chronic contact stress exposure in the onset and progression of PTOA is extremely important in prioritizing future clinical research endeavors. If irreversible damage is done from the initial insult of an injury, efforts to develop biological intervention may be prioritized to allow for sufficient cartilage restoration. Conversely if joint incongruity following surgical reduction is the main factor in determining PTOA risk, then further effort should be prioritized in restoring and maintaining the anatomical conformity of the joint [7].

3.1.3 Previous Work in Ankle Contact Stress Evaluation

In order to separate the influence of chronic contact stress exposure and acute fracture severity on PTOA development, studies have been completed involving tibial plafond fracture patients [9-13, 52]. The human ankle joint is useful as a model for the study of PTOA development because of its extremely low incidence of primary OA, combined with the high incidence of PTOA following intra-articular fracture [52, 53]. One line of research was conducted using engineering fracture mechanics principles to quantify acute fracture severity [10]. In that study, CT scans of 20 pre-op tibial plafond fracture patients were segmented and used to quantify liberated surface area associated with the fractures [10]. This liberated surface area correlated with the amount of energy released in the fracture of the tibial plafond. A second line of study was conducted using finite element analysis on the same series of ankles [9, 11-13]. Eleven patient-specific post-op ankle models were created and evaluated for contact stress, over 13 discrete instants from the gait cycle, and their contact stresses were compared with those from their intact contralateral limb. A chronic contact stress-time exposure metric was then used to stratify the ankles with regard to severity [9]. The results of those studies were compared against the 2 year follow-up Kellgren Lawrence (KL) score for each of the subjects. The KL score is a radiographic measure ranging from the 0 (no visible OA) to 4 (severe OA), by rating the presence and severity of multiple indicators of OA [54]. These studies derived a contact stress-time exposure metric that demonstrated 100% concordance with OA development (KL ≥ 2) and a 95% concordance with KL grade [9]. Both the fracture and contact stress severity studies showed promising results on correlating their respective measures to PTOA risk. However, their statistical power was significantly limited due to their small sample sizes (n=11 and n= 20). The primary limiting factor in sample size was not difficulty in enrolling patients, but rather challenges arising in the processing of data[9]. Ideally hundreds of subjects would need to be evaluated to accrue sufficient statistical power to unravel the influence of acute injury and residual incongruity in PTOA development following articular fracture. This fact speaks to the need for a more expeditious method of evaluating both chronic contact stress exposure and acute fracture severity.

3.2 Expedited Computation of Contact Stress in Twenty-Two Patient-Specific Human Ankle Models

The goal of this portion of the study was to establish the equivalence between FEA results and the previously discussed DEA algorithm with respect to resultant kinematics, contact stress distributions and reliability for predicting PTOA development. The FEA models and boundary conditions previously used were translated as faithfully as possible, to allow for direct comparison between FEA and DEA results.

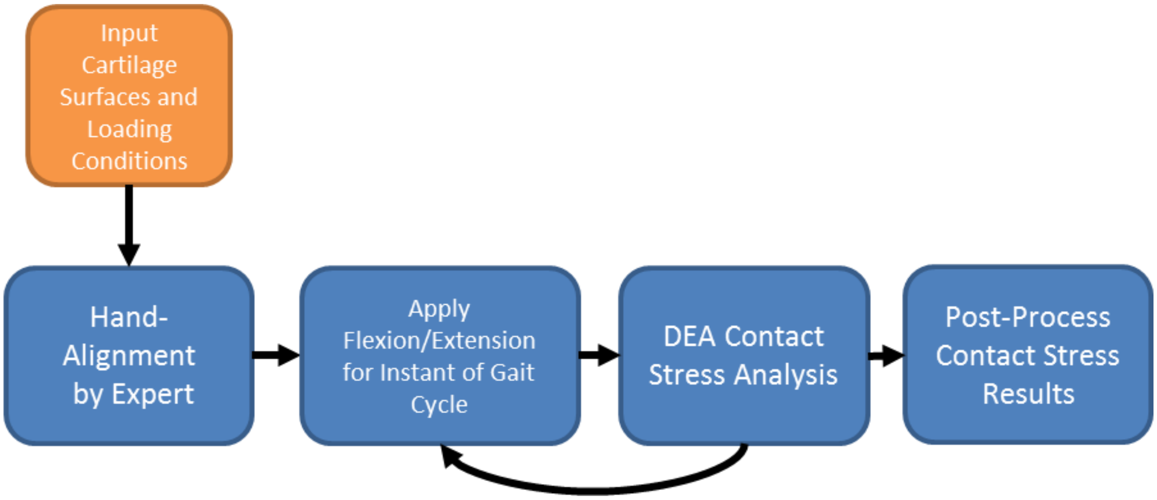

Figure 18. Flowchart of overall procedure for ankle DEA contact stress computation. Cartilage surfaces where taken from a previous FEA ankle contact stress study and were run with similar loading alignments and boundary conditions through a 13 step flexion/extension arc to simulate the stance phase of human gait. Following contact stress computation, results were post-processed to produce a contact stress-time exposure metric, to evaluate the relationship between PTOA and chronic contact stress exposure.

3.2.1 Model Creation

Models were adapted from a previous FEA study detailing the effects of chronic contact stress on PTOA development [11, 12]. The outer faces of hexahedral elements representing articular cartilage of the tibia and talus were taken from the finite element mesh. The quadrilateral faces were each bisected along their diagonals into triangular faces. This allowed for simple direct comparison of contact stress between the FEA and DEA results, by simple interpolation from the FEA results to the DEA results. It also ensured that surface geometry and curvatures were identical for accurate comparison between the two methodologies.

3.2.2 Model Alignment

The models used for this study had been previously aligned to a nominal loaded apposition by an expert orthopaedic surgeon [12]. The DEA models were positioned in the global coordinate system with the same orientation as the FEA models, so that the joint axes were aligned identically. Superior translation coincided with the +Z axis, anterior translation coincided with the +Y axis, lateral translation coincided with the +X axis, flexion coincided with rotation about X axis, inversion coincided with rotation about the Y axis and internal rotation coincided with rotation about the Z axis.

3.2.3 Ankle Loading and Constraints

Boundary conditions from the previous FEA study were also replicated as closely as possible within the framework of DEA [12]. The tibia was constrained in all directions except for motion in the axial direction (Superior/Inferior) to allow for load control. The talus was constrained only against flexion/extension and superior-inferior translation. A gait cycle simulation was run as a 13 step flexion-extension arc to represent the stance phase of human gait. Within this flexion/extension arc the talus was rotated under the tibia. This differs from the previous FEA study in which the tibia was rotated over the talus, but was considered a valid method of simplifying load computation on the tibia. Load was applied axially to the tibia as a percentage of patient body weight, based on previously obtained motion capture and force plate data [55].

A single 100N/mm spring was applied to the talus to represent the stabilization afforded by the lateral malleolus of the fibula, which was not explicitly modeled. The spring was applied once the talus had seated onto the distal tibial surface on the first loading challenge.

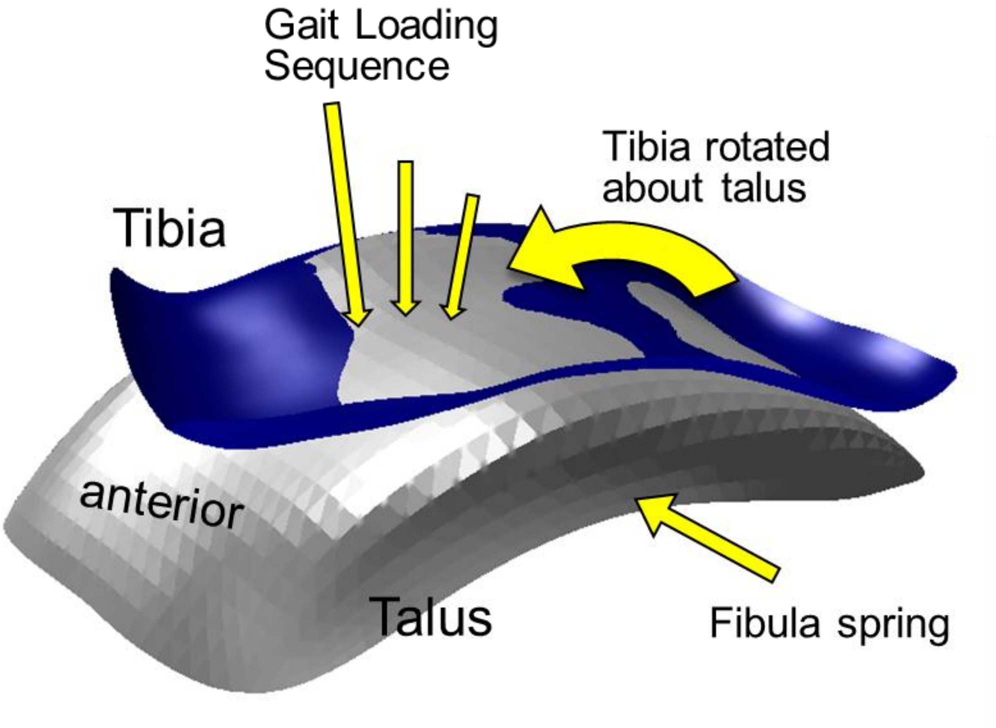

Figure 19. Schematic showing general gait cycle and loading of tibia over talus. Relative rotation between the tibia and talus is changed according to position in gait cycle. Axial loading on the tibia is the subject body weight scaled according to the phase of gait. A spring is applied to the talus to represent the stabilization of the tibia [11].

3.2.4 Cartilage Thickness Selection

To coincide with the previous study, cartilage was assumed to be uniformly distributed over the bones, with a 1.7 mm thickness. Previously, cartilage had been represented as a uniform extrusion from the segmented bone surface [12].

3.2.5 Expedited Evaluation of Contact Stress

Contact stress was evaluated using the previously described DEA algorithm. This algorithm was used in load control in direct replication of the previous FEA study. A full 13-step flexion/extension arc representative of the stance phase in gait was run for each patient-specific model. Cartilage was treated as a linear elastic and frictionless material with a Young's modulus of 12 MPa and a Poisson's ratio of 0.42 [12].

Following simulation, the contact stress computed for each loading step was compared to the FEA results, on a node by node basis. A cumulative contact stress exposure metric was calculated for each patient by multiplying instantaneous contact stress (raw DEA result) with its associated time duration in a normal gait cycle.

The contact stress-time challenge was then used to form a metric for PTOA development. This was done assuming that there is a minimum contact stress threshold, Pd (MPa) which cartilage must experience to be susceptible to damage. Once an area of the ankle cartilage exceeded Pd, a second metric, $Pd_{critical}$, (MPa-s) was used to describe a contact stress-time dosage within this at-risk area, required to cause damage. These two thresholds were used to define a contact stress exposure metric, by computing the percentage of area within Pd which also exceeds $Pd_{critical}$[9]. These threshold values were varied parametrically varied over a wide state space (0 – 15 MPa and 0 – 15 MPa-s for Pd and $Pd_{critical}$, respectively) and concordances were calculated between this metric and a 2 year post-op KL grades for all 11 subjects [9]. The parameters which provided the highest concordances were selected as optimal parameters for the contact stress-time exposure metric.

3.3 Resulting Contact Stress Distributions and Evaluations

Contact stress results from eleven pairs of intact and post-op fractured ankles were converted into a total cumulative contact stress-time metric. This was done by computing a summation of contact stress values (Cstress) from each of the 13 steps in the gait cycle weighted by their associated time duration (Tgait) in the gait cycle.

$$Cstress_{exposure} = \sum_{i=0}^{13} (Cstress_i * Tgait_i)$$

Comparisons between the FEA and DEA contact stress-time challenge are depicted in Figure 20. Contact stress-time distributions overall were similar between the DEA and FEA models. The DEA model did produce higher contact stress-time exposure values in areas of high incongruity and lower values elsewhere. Differences between the DEA and FEA contact stress exposure values are reported in Figure 21. These contour plots reflect contact stress-time exposure values compared on a node-by-node basis. Green colors indicate little or no difference between the two models, red patches show higher FEA contact stress computation and blue patches show higher DEA contact stress computation. The majority (90%) of the contact stress area on both the intact and post-op cases show differences below ±1MPa. Larger discrepancies between the two stress analysis methodologies were largely present on the borders of contact, or areas of high incongruity.

A histogram of the differences between FEA and DEA computed contact stress values were constructed on a node-by-node basis (Figure 22). The difference in contact stress was measured for intact and post-op fractured ankles for each instant of the gait cycle across all 11 ankles. Nodes which did not experience contact stress in either methodology (0 MPa) were omitted from this analysis. Differences between the FEA and DEA models were normally distributed around 0 for both the intact and post-op cases. There was a higher level of disagreement in the post-op cases when compared to the intact cases. When compared across all steps for the gait cycle for 22 models, 97% of the contact area was within a ±1MPa contact stress difference threshold for intact ankles and 89% of the area for fractured ankles.

Area engagement histograms were also made for the FEA and DEA intact and post-op cases (Figure 23). These plots report the relationship between intact and post-op cases is similar for both methodologies, with the intact cases having a higher proportion of the contact area experiencing low contact stress levels and the post-op cases having a higher proportion of contact area with higher contact stress levels.

Results from the DEA models were post-processed using a previously described contact stress-time overexposure metric as a predictor of OA ratings (KL grade). Two separate variables, Pd, a variable signifying a contact stress exposure threshold, and Pd$_{critical,}$ a variable signifying a contact stress-time exposure threshold, were systematically varied in 0.1 MPa increments over a wide range of values (0-15 MPa and 0-15 MPa-s). The separate measures obtained using all possible values of Pd and Pd$_{critical}$ were then compared to binary OA status 0 for K<2, 1 for KL≥2) and KL grade. The values which provided the optimal concordance for both OA status and KL grade were identified. The optimally predictive value for Pd was found at 11 MPa, and Pd$_{critical}$ was 1 MPa-s. Using these values there was excellent discrimination between the cases which developed OA and the ones that did not. Computed predictive agreements of the measures were 95% KL grade concordance and 100% OA concordance (Figure 24).

One attractive aspect of DEA is that it does not suffer from the same numerical convergence issues in computing contact that FEA is prone to. There were models for nine previous cases which had been prepared for FEA analysis, where the FEA code ran into insurmountable numerical convergence issues precluding successful completion. Of these cases, there were six intact ankles and three post-op fractured ankles with 2 year follow-up KL grades. By contrast, these FEA-troublesome cases were run using the DEA algorithm with no difficulty whatsoever, and contact stress distributions were plotted (Figure 25). Additionally, new values were selected for Pd and Pd$_{critical}$ (Pd = 4.1 MPa, Pd$_{critical}$ = 5.1 MPa-s) and KL concordances were reported using all 31 DEA computed ankles as 92% KL grade concordance and 100% OA concordance (Figure 26).

The average time for running each DEA model through a full 13-step gait cycle was 3-5 minutes on a quad-core 8-thread Intel Core i7 920 CPU with 12 GB of RAM.

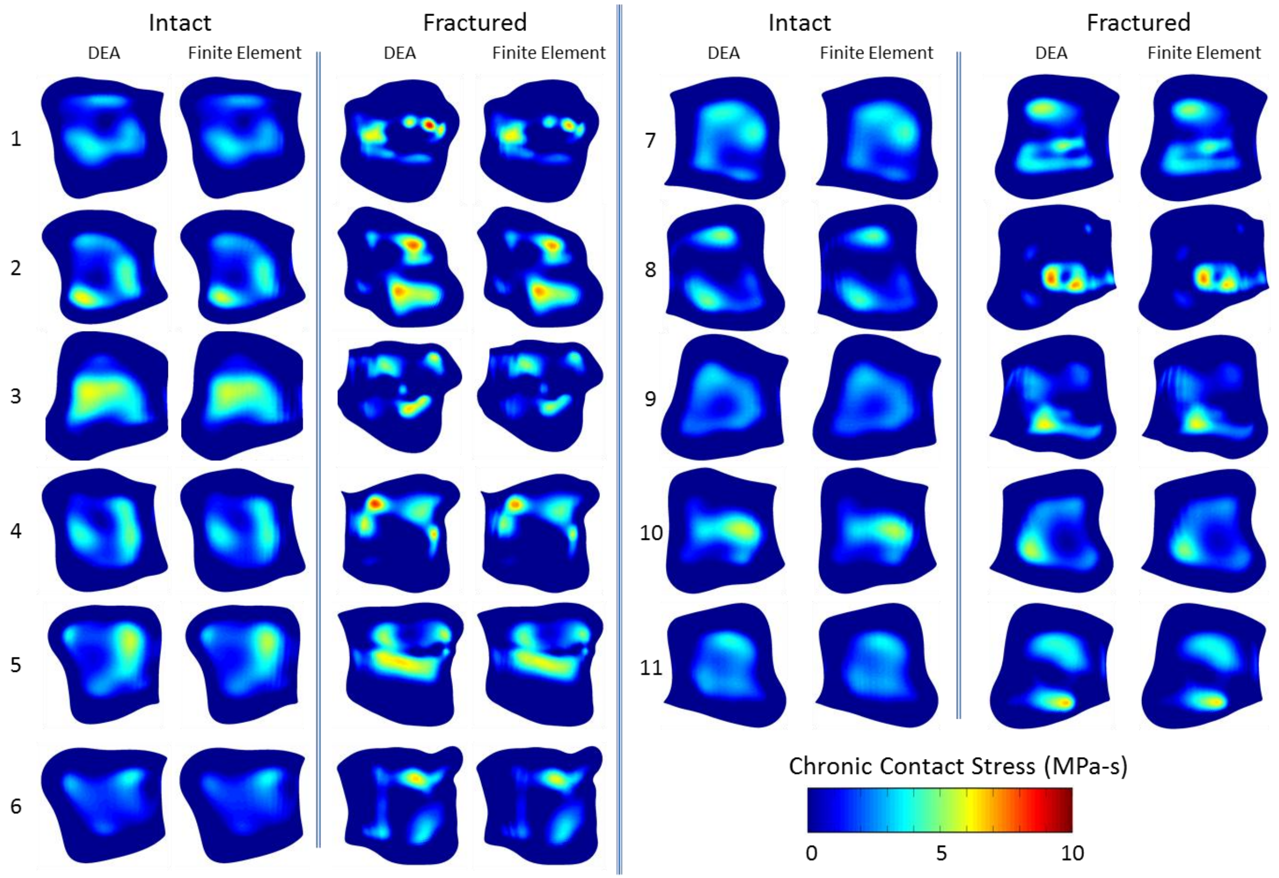

Figure 20. Cumulative contact stress-time distributions for eleven post-op fractured ankles and their intact contralateral pairs for both DEA and FEA results. DEA results are interpolated to the FEA node locations using bi-linear interpolation.

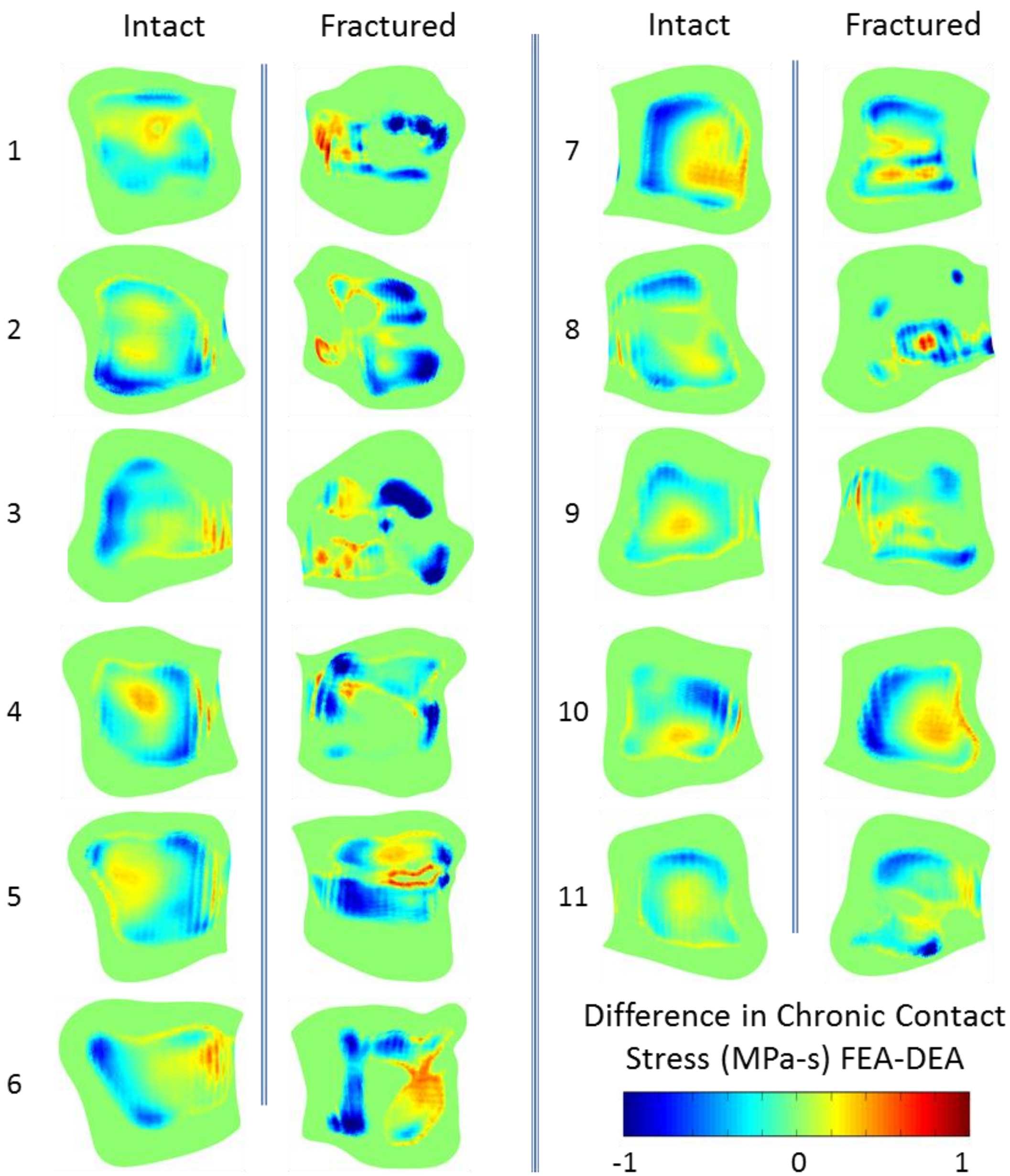

Figure 21. Differences in FEA and DEA cumulative contact stress-time exposure. Differences are computed on a node-by-node basis.

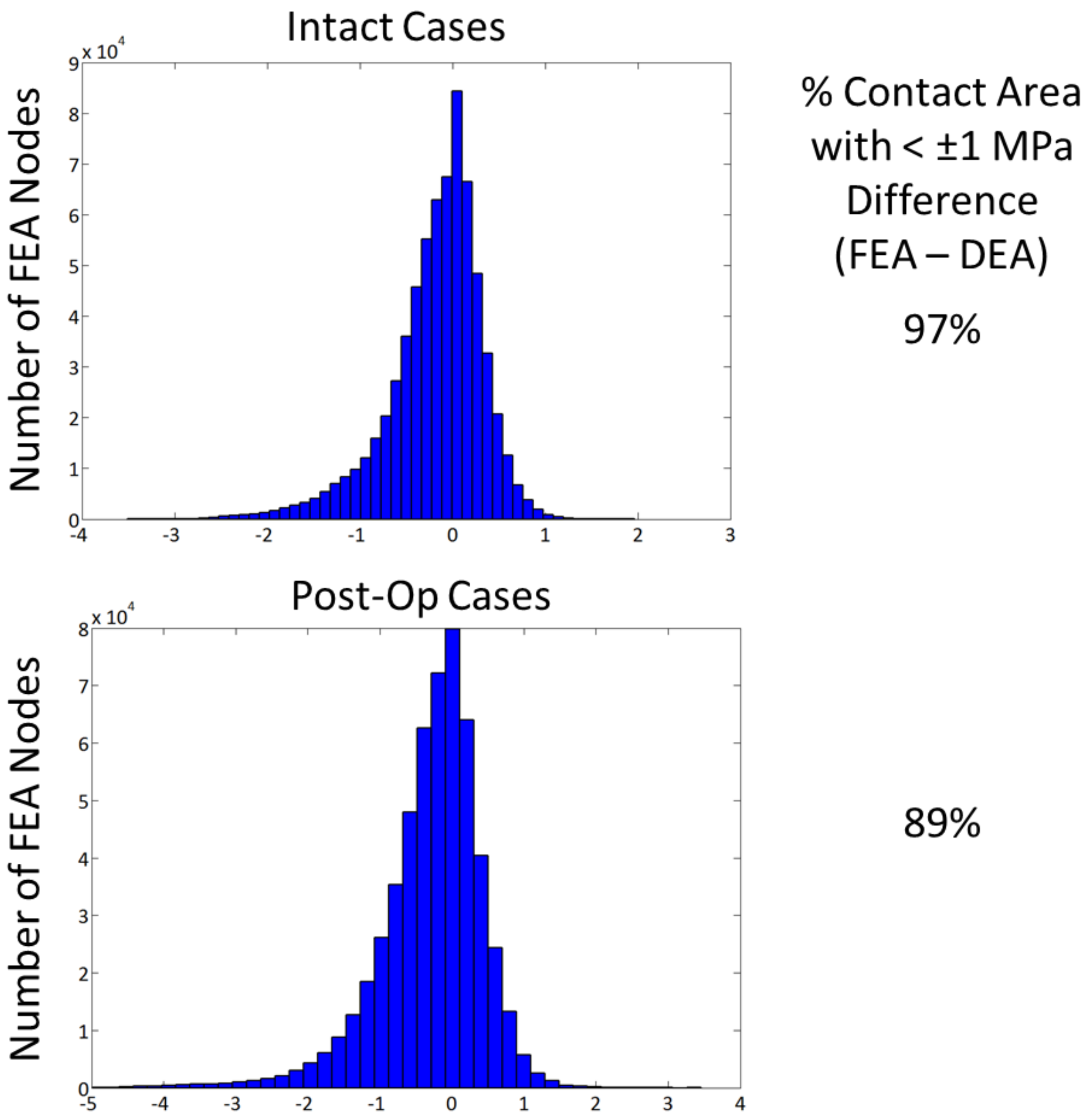

Figure 22. Histogram of the node-by-node contact stress differences between FEA and DEA models in both intact ankles and post-op fractured ankles. Percent of total contact area which has a contact stress difference of less than ±1 MPa is also shown.

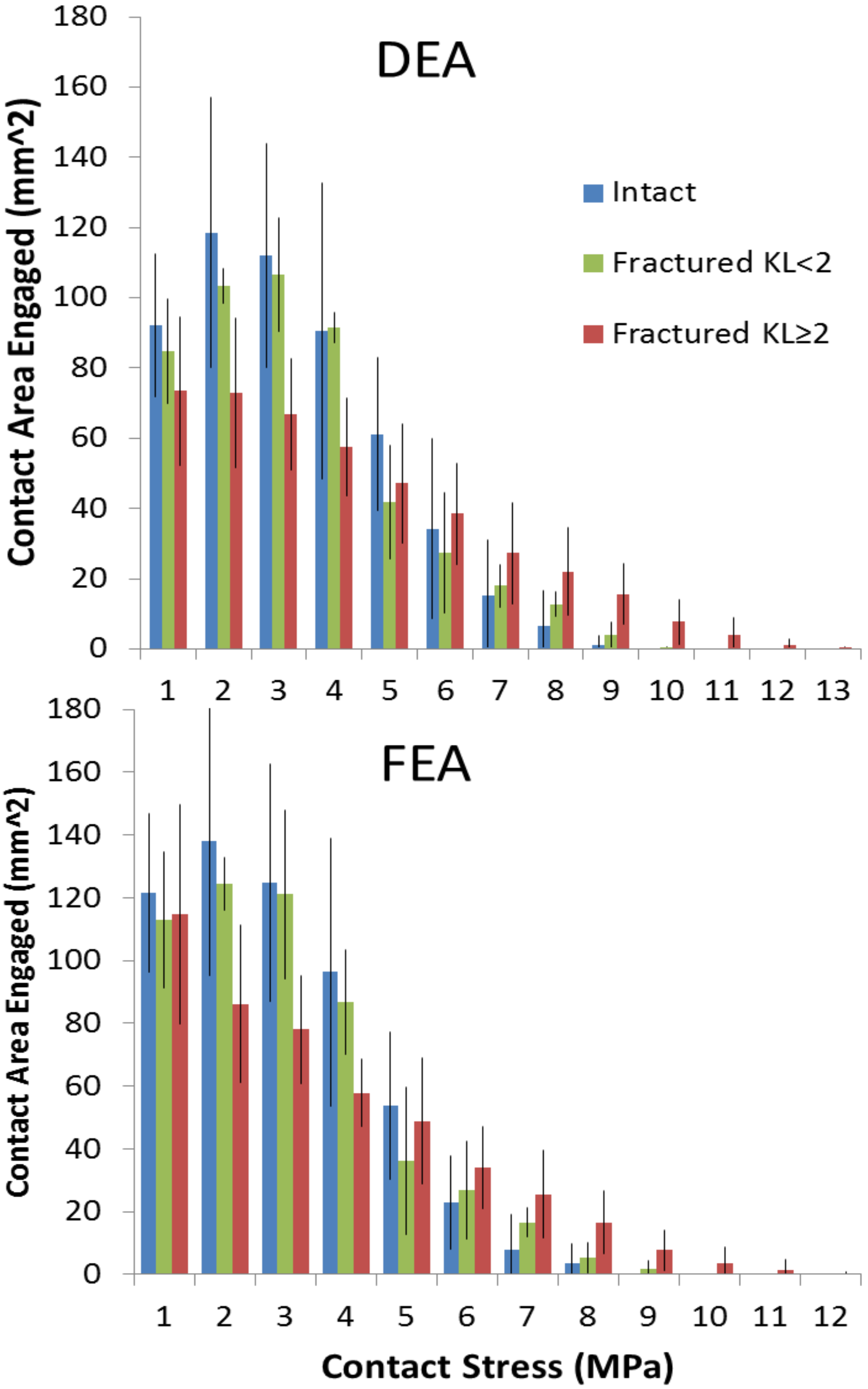

Figure 23. Contact area engagement histograms for both FEA and DEA computations. Fractured ankles are separated into ankles which developed radiographic OA (KL ≥ 2) and those that do not (KL <2). Error bars show standard deviations.

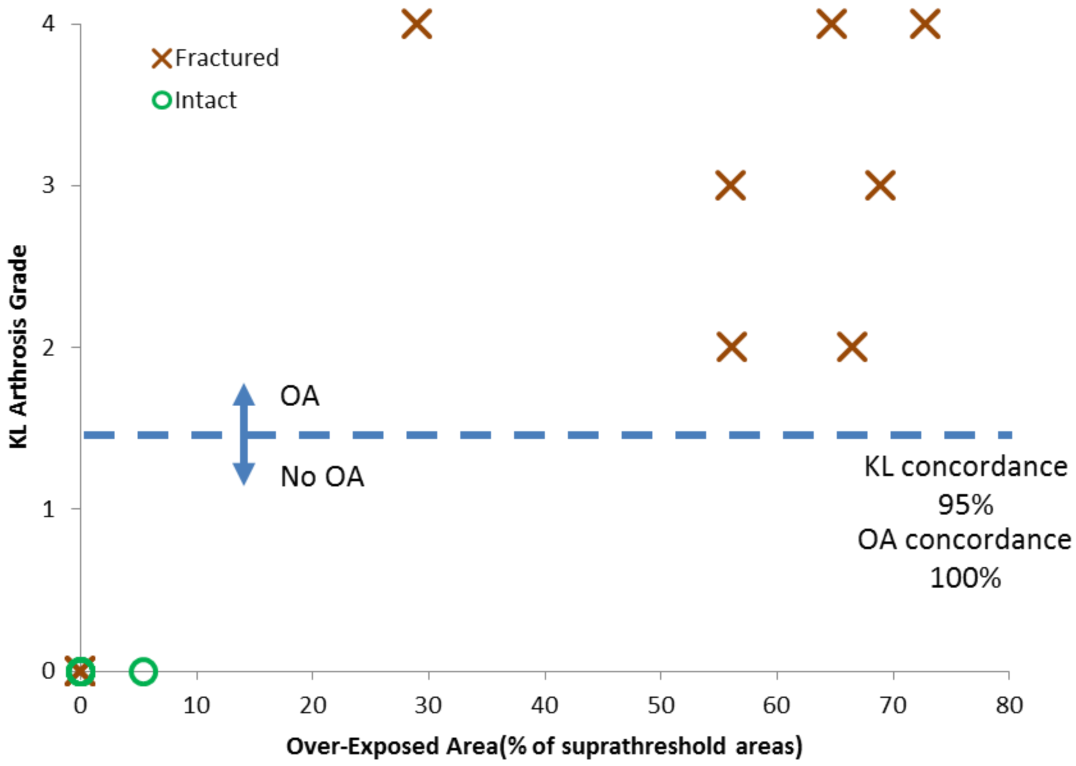

Figure 24. Concordance of 2-year post-op KL grades with contact stress-time-area exposure metric across 11 pairs of intact and fractured ankles. Computed concordances were 95% with KL grade and 100% with OA radiographic OA presence (KL>1).

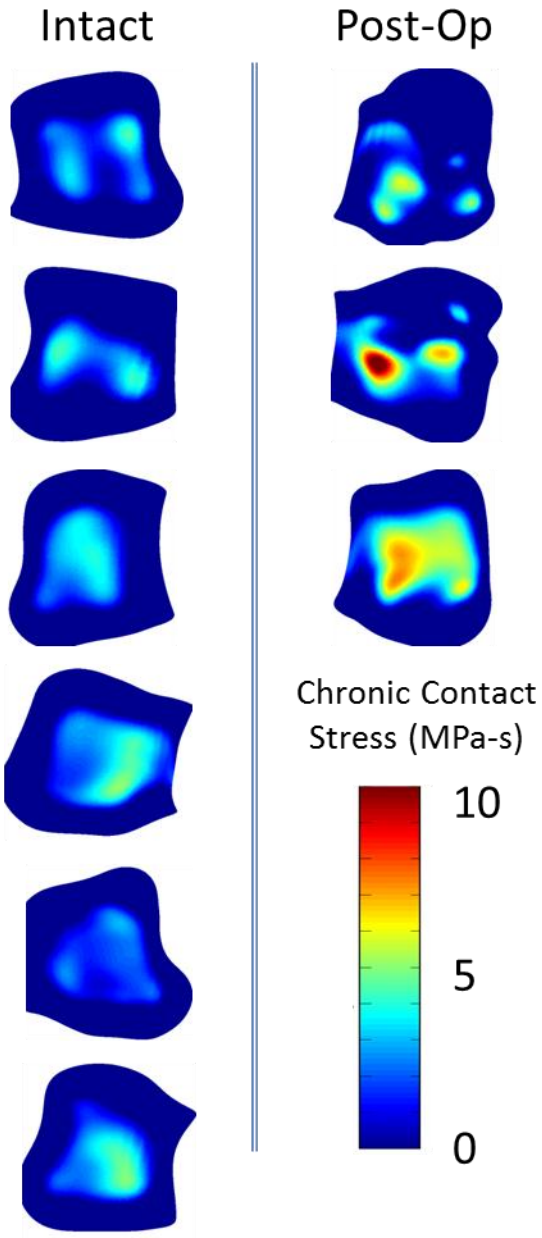

Figure 25. Cumulative contact stress-time distributions for nine ankles which previously could not be computed due to numerical convergence issues with FEA. Six intact ankles and three post-op ankles were computed.

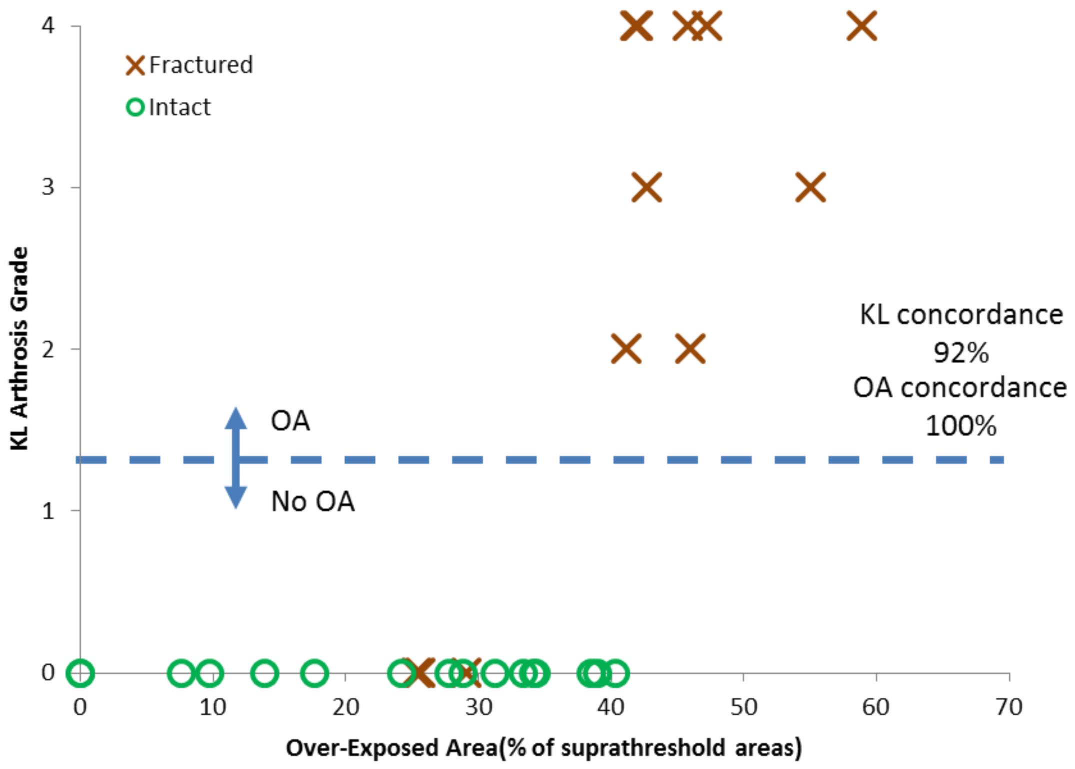

Figure 26. Computed concordances of 2 year post-op KL grade with contact stress-time exposure metric using all 31 computed ankles.

3.4 Interpretation of Resulting Contact Stress Distributions and Evaluations

The discussed DEA methodology showed a substantial ability to replicate the previously-obtained FEA results pertaining to ankle contact stress distributions over a 13-step gait cycle in load control. When evaluating contact stress on a node-by-node basis, DEA frequently (91% of total contact area) is within 1MPa of the FEA-computed contact stress. As with the validation study, DEA demonstrated a tendency to over-estimate FEA values in regions of high contact stress, and to under-estimate FEA values in regions of low contact stress, most likely due to the greater deformability of the FEA formulation.

Much of the discrepancy comes around the edges of contact where several factors can influence the reported contact stress (Figure 21). First, small differences between the

FEA load control and the DEA load control are inevitable. These small differences may cause one model to translate or rotate a fraction of a mm or radian differently, causing a situation where an area of high incongruity is slightly shifted leading to a high reported discrepancy (> 1 MPa-s) between FEA and DEA. Second, FEA has a greater ability to capture the deformity occurring in a model. This is a fundamental difference between FEA and DEA in which FEA treats the surface as a continuum where stress applied focally to one element will affect the adjacent elements creating a wider contact patch. Conversely, elements in DEA are independent from one another so a focal stress will only affect elements directly. This wider contact patch of the FEA may account for the discrepancies along the borders of contact as well as the ring of higher FEA stress surrounding contact patches (Figure 21). These are presumably regions where the deformable nature of the FEA allows the model to adapt to regions of high contact stress and deform by ‘squishing’ the contact patch to effectively make it larger.

There were also discrepancies between the FEA and DEA models in which there appeared to be an imbalance in the contact patch (i.e. there appeared to be an ML or AP bias in the contact patch for DEA when compared to the FEA). This can be explained by differences in the load balancing between FEA and DEA. Even small changes in translation/rotation can have a significant effect on the resulting contact stress [36].

When looking at the majority of nodal comparisons, the observed differences were less than ±1 MPa, and were centered about 0 MPa. This leads to further examination of the relationship between FEA-and DEA-derived contact stress distributions in the human ankle joint. When the ankles were separated into intact cases, fractured cases without OA (KL < 2), and fractured cases with OA (KL ≥ 2), examination by a contact area engagement histogram showed a clear delineation between the ankles with and without OA (Figure 23). Similar to the previous FEA study, ankles with OA show a much higher amount of contact area which is experience high (> 5 MPa) contact stress levels[12]. The difference between ankles which develop OA and those that do not is in fact more pronounced for DEA than for FEA, perhaps due to the tendency of DEA to compute higher contact stresses within areas of incongruity. Additionally, fractured ankles that did not develop OA (KL < 2) appear more similar to intact contralateral ankles than fractured ankles that did develop OA (KL ≥ 2), in terms of contact area engagement. This clear delineation between ankles with and without OA with regards to contact area-engagement provides impetus for utilizing DEA as an alternative to FEA for computation of a contact stress exposure metric.

The DEA model was able to display equivalent predictive ability for both OA development and KL grade, with concordances of 100% and 95%, respectively with a contact stress-time-area exposure metric. This is a slight improvement from the reported 100% OA and 94% KL grade concordances from the previous FEA study [9]. Despite the significant simplifications in DEA with regards to modeling complexity, DEA and FEA appear to be equivalent in their ability to predict OA development. The tendency for DEA to over-estimate contact stress values in regions of high incongruity may have the effect of improving the separation of fractured and intact ankles, thus improving OA predictions in future samples of patients.

Based on these data, we conclude that the DEA method is a suitable (indeed, perhaps preferable) alternative to FEA for determining the role of contact stress exposure in PTOA development. The DEA method is especially compelling for large studies using patient-specific models, considering that run times are on the order of 3-5 minutes, that DEA models need not be taken through a FEA meshing process, and especially that numerical convergence issues are problematic factor in DEA. The DEA method clearly provides significant reduction in computational complexity and investigator time, making it suitable for studies on the order of hundreds or perhaps even thousands of patient- or subject-specific geometries.

Now that the DEA methodology has been shown to offer significant reductions in computational and investigator expenditure, bottlenecks using the DEA method have moved to other portions of the process. Better techniques for segmenting 3D data sets to form 3D surfaces suitable for DEA are required. Additionally better methods for the alignment of joints to functional appositions, quickly, and accurately are needed for effective and valid contact stress measurements.

Automated and semi-automated normative alignment techniques are currently being developed for use with ankle datasets to help resolve this issue. An iterative closest point alignment algorithm combined with a global optimization component has been proposed for solving this issue. This technique allows for previously aligned intact ankle geometry to serve as a template for normative alignment of both fractured and intact ankles. A normative alignment is considered adequate for the ankle due the fact that ankle stabilization is primarily due to the congruency of the articular surface.

CHAPTER 4: APPLICATION II - CONTACT STRESS EVALUTATION IN THE HUMAN KNEE

4.1 Background and Motivation

4.1.1 Human Knee Anatomy

The human knee is a di-arthrodial joint involving the proximal tibia, distal femur, proximal fibula and patella bones, supported by ligamentous and muscular attachments. The distal end of the femur consists of a medial and lateral condyle, which are each specifically shaped to articulate with the matching surfaces on the proximal end of the tibia. The proximal end of the tibia, known as the plateau, consists of medial and lateral cartilage-covered facets that are separated by a central ligamentous attachment region, the tibial spine (Figure 27). This division of both the femur and tibia has led people to commonly describe the knee as having medial and lateral compartments. The medial compartment tends to be larger than the lateral, in both the radius of curvature of the femoral condyle and in the area of the medial tibial plateau [56]. Articulation between the two bony surfaces is stabilized and supported by a fibro-cartilaginous structure known as the meniscus. The medial and lateral portions of the meniscus are anchored to the tibial spine, providing semilunar “cups” for the femoral condyles to settle into. This is of great importance in knee stability due to the somewhat convex nature of the tibial and femoral articular surfaces [56]. The majority of knee support during dynamic activities, however, is from ligamentous and muscular attachments [57].

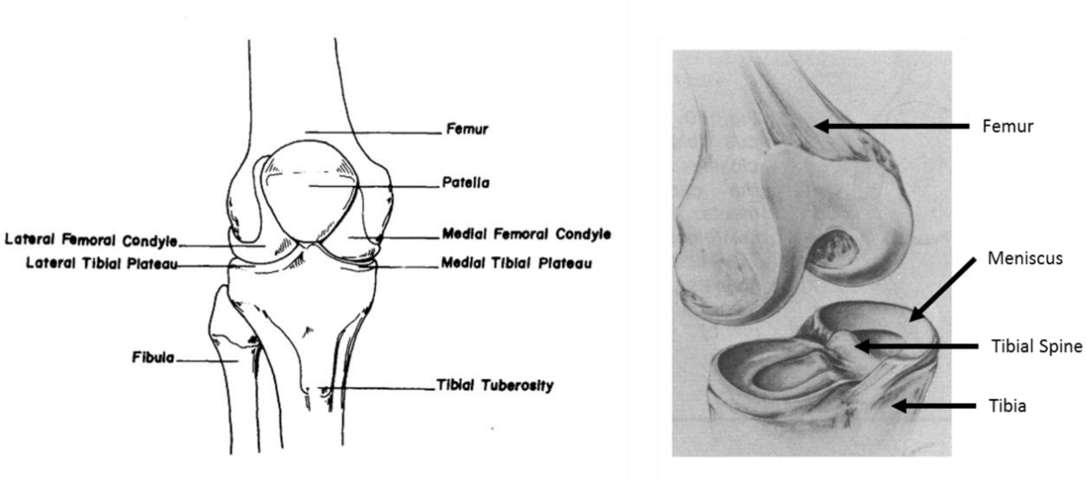

Figure 27. Knee anatomy from a coronal (left) and isometric (right) view. Depicting the femur tibia fibula and patella along with articular cartilage and meniscus. Taken from (Blackburn et al 1980).

The specific bony anatomy of a healthy knee allows the medial femoral condyle to rotate triaxially on the tibia, as well as to translate predominantly in the AP direction. The lateral femoral condyle likewise can translate freely in the AP direction but has limited rotation about the sagittal anatomical axis [58].

4.1.2 Knee Osteoarthritis

Knee osteoarthritis is one of the most prevalent forms of OA, occurring in approximately 6% of adults age 30 or higher [59]. In elderly persons the disability caused by knee OA is as life-altering as that of heart disease [60]. Additionally, the presence of knee OA increases the risk of disability due to other medical complications [61].

OA is a disease which involves the whole joint and is characterized by progressive hyaline cartilage degeneration and corresponding changes in the underlying bone such as growth of osteophytes. Additionally surrounding soft tissue structures can be affected, showing minor inflammation, lax ligaments, and weakened bridging muscle

[59]. Many people who present with radiographic signs of knee OA do not report symptoms or pain with joint use [62].

Even though the societal and economic impact of OA in the knee is large, very little is known about the disease's onset and progression. Although a wide array of societal, biological and mechanical risk factors have been implicated in knee OA worsening, it is widely acknowledged that local mechanical factors play a significant role [60]. Elevated contact stress due to abnormal joint shape, overuse, incongruity or misalignment is widely thought to influence the development of knee OA [59].

Due to a dearth of tools to study contact stress on a large number subject-specific joints, it previously has not been possible to conduct a large scale investigation into the relationship between contact stress exposure and knee OA. Development of expedited methods for large-scale evaluation of contact stress exposure now allows for use of large epidemiological databases for conducting controlled studies. The multicenter osteoarthritis study (MOST) is a study consisting of a cohort of 3,026 men and women (50 to 79 years old) who have been drawn from the general population but were selected to have pre-existing knee OA or to be at high risk for knee OA due to risk factors such as obesity and prior knee surgery [63]. Large-scale studies such as MOST, when combined with large-scale contact stress assessment tools, present a unique opportunity for statistically robust investigation of the relationship between contact stress and OA progression.

4.1.3 Bone Marrow Lesions in Clinical MRI and Relevance to Contact Stress Exposure

Subchondral bone marrow lesions, (BMLs) often discernable on MRI images as areas of aberrant signal intensity in the femur or tibia bone (Figure 28), are thought to represent possible areas of damage or remodeling within the bone[64, 65]. Bone marrow lesions have been shown to be related to general mechanical factors such as obesity [66, 67], malalignment [68] and joint trauma [67, 69, 70], all of which are associated with knee OA. Additionally, severe bone marrow lesions have been found to be predictive of progression of symptomatic knee OA [66, 71]. Bone marrow lesion worsening has also been found to relate to cartilage loss when compared to stable BMLs [72, 73]. Bone marrow lesions have also been shown to decrease in size and improve, a behavior which has been related to correction of limb alignment [74, 75]. Reduction in BML size has also been shown to relate to reduced cartilage loss [76]. All of these factors point towards BMLs being an excellent indicator of OA risk, especially in combination with the finding that BMLs occur in an injury-specific pattern following joint trauma [77].

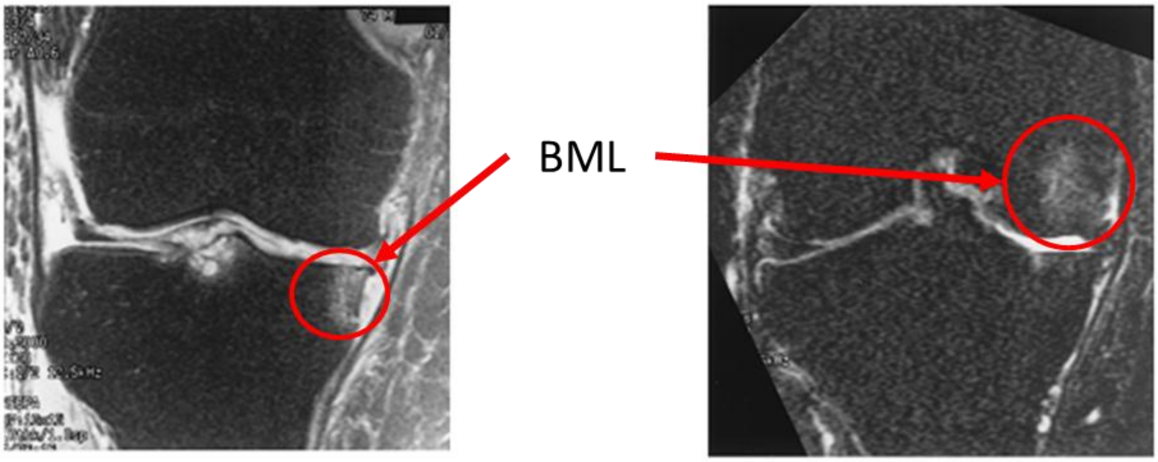

Figure 28. Bone marrow lesions (BMLs) in the human knee are detectable on MRI images as areas of relatively high intensity in the femoral lateral condyle (right) and the lateral tibial compartment (left). BMLs are believed to be an indicator for OA progression and joint pain. Adapted from (Felson et al. 2001)

Articular contact stress exposure has previously been linked to risk for symptomatic knee OA development, using expedited DEA contact stress evaluation methods [78]. However DEA and similar methods have not yet been used to predict structural worsening. Since BMLs and cartilage damage have been associated with increased compartmental loading, the ability of compartment-specific cartilage stress to predict risk for structural worsening and BMLs merits assessment.

4.2 3D-2D Alignment of Bone Morphologies to Subject-specific Appositions

4.2.1 Background and Previous Work

Precise and accurate alignment of articulating surfaces is of critical importance in contact stress computations. Even with the relatively high compliance of cartilage, alignment errors of fractions of a millimeter can significantly alter contact stress results [36]. The knee joint is particularly sensitive to this problem, by virtue of its bi-compartmental nature.

Articular joint modeling often utilizes stabilizing support forces from ligaments. Simulations can be run in load control to better align a joint to a physiologically appropriate position. At the very least, a nominal "normal" alignment can be assigned by a clinician or a computer algorithm. When conducting a study with a large number of subjects at varying levels of disease progression, however, this becomes a more difficult problem. Many subjects may have joint malalignment as a result of soft tissue damage and joint disease progression that have a significant effect on contact stress [36]. This subject-specific alignment is difficult to capture in a "one size fits all" approach, due to the wide array of bone, cartilage, meniscus, and ligament competencies that occur through natural biologic variability. Additionally, it is difficult to capture a functional loading behavior using the 3D medical image acquisition techniques (MRI and CT) typically used for model creation, due to the fact that patients are typically required to be in a supine relaxed position. A secondary, typically 2D, imaging technique is necessary for the acquisition of a subject-specific alignment during a functional loading activity. It is necessary then to perform a registration of the 3D modeling data from the unloaded joint to the 2D functional loading data, to perform contact stress assessment using a subject-specific loading apposition.

Over the last 20 years, a large number of 3D-to-2D image registration techniques have been developed for a wide variety of applications. Techniques were developed primarily for image guided surgery, radiotherapy, radiosurgery and minimally invasive surgery [79]. The registration techniques primarily involve bringing multiple separate image datasets into a common coordinate system, typically a 3D single data set and one or more 2D datasets describing some additional aspect of subject positioning [79, 80]. Typically the 3D datasets used originate from CT or MRI imaging modalities, whereas the 2D data sets can originate from a multitude of sources such as fluoroscopy, plain radiographs, 2D ultrasound, or optical images [79].

3D-to-2D alignment algorithms can be classified in a variety of categories, the simplest being intrinsic or extrinsic. An extrinsic method is a method that uses some sort of additional hardware or intervention such as radiographic markers as a basis for 3D-to-2D alignment. While extrinsic methods are highly accurate and have a closed form solution, they are infeasible for large-scale *in vivo* study due to invasiveness [80]. An intrinsic method uses the inherent properties of the structure being aligned as a basis for alignment. Intrinsic alignment methods are of particular interest for large-scale clinical studies due to ease of obtaining clinical diagnostic x-ray data.

Intrinsic methods can further be broken down into categories based upon their matching methodologies, as being feature-based, intensity-based, or gradient-based [79]. Feature-based methods rely upon utilization of general shape information, from the 3D and 2D image data [42, 81-85]. As they do not take into account intensity information they tend to be useful for multimodality registration techniques such as matching MRI to fluoroscopy, in which the intensities relative to the images have a significantly different meaning [79]. Feature-based methods rely upon accurate segmentations of both the 3D and 2D geometries for accurate alignments, which is a non-trivial task for both automated and manual segmentation [85]. Intensity-based alignment strategies attempt to match intensities between the 2D and 3D data sets. The most common implementation of this technique is digitally reconstructed radiographs or DRRs. This method performs matching of voxels of the 3D image to that of the 2D modality based on some aspect of their intensity, and as such does not require accurate segmentation. Intensity-based methods, however, are poorly suited to matching x-ray images with MR images, due to the vast differences in the imaging modalities [79]. Gradient techniques rely upon matching vectors from the image gradient directions in both the 2D and 3D images, using some sort of gradient correlation measure [86].

Feature-based, intensity-based and gradient-based methodologies can be brought into concordance with one another, based upon three separate techniques: projection, back-projection, and reconstruction [79]. Projection techniques attempt to map the 3D dataset to a 2D dataset and then perform a 2D-to-2D comparison. Back-projection attempts to map the 2D dataset to back into a 3D space for comparison. Reconstruction techniques attempt to use multiple 2D data sets to construct a 3D image representation, and then perform a 3D-to-3D image registration. Each of these three projection techniques can be used with each of the three matching techniques, to form a grid of all currently used methodologies (Figure 29).

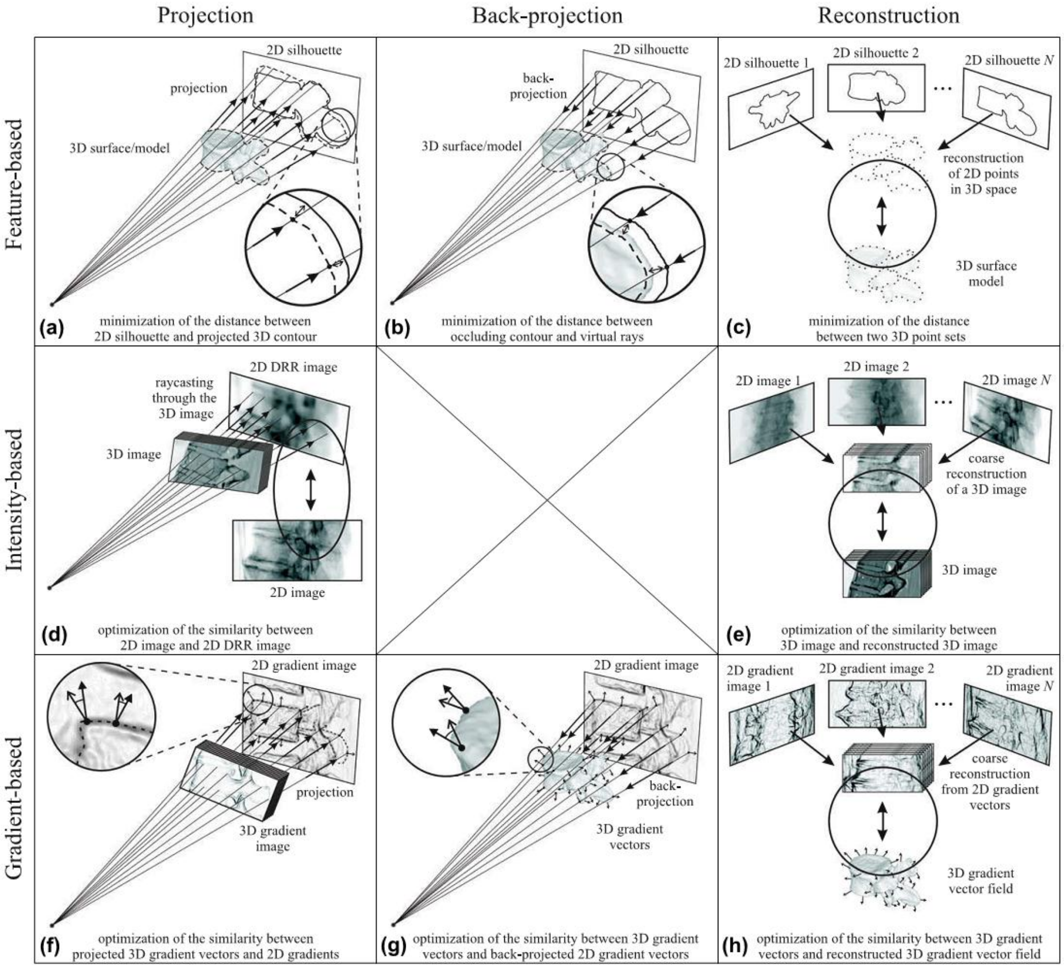

Figure 29. Array of fundamental methods for 3D-to-2D alignment techniques [79].Taken from Markelj et al. 2010

Image registration algorithms further rely implicitly upon an optimization procedure, which is well suited to optimizing translations and rotations of a 3D model (six degrees of freedom) using a cost function with many local minima [79]. For an extrinsic approach simple closed form solutions may be possible [87]. However intrinsic approaches require more advanced optimization techniques due to the inherent discrepancy and error between the 3D and 2D images, due to mismatches in machine calibration, segmentation error, and inherent differences in modalities used. Typically an optimizer is used to search for the geometric transform which best merges the coordinate system of the 2D and 3D datasets. Feature-based methods treat the problem as a minimization of a cost function, based on the difference between the apparent features [79]. This has been used with a number of different local and global optimization techniques such as downhill simplex, gradient descent, Levenberg-Marquardt and simulated annealing [88].

3D-to-2D registration techniques are ideal for orthopaedic applications due to the rigidity of bone, and the ease with which bone surfaces are delineated within CT and x-ray imaging. These techniques have been used for pedicle screw placement, placement of femoral implants, measuring joint kinematics, and in tracking fragment motion during surgical procedures. X-ray-based methods are typically used with single and bi-plane x-ray and with fluoroscopy shape matching techniques. Typically, single plane x-ray-based methods reported ±0.5mm/degree accuracy and biplane methods report ±0.1mm/degree accuracy, versus corresponding physical movement [36]. Many of the techniques used report translational accuracy on the sub-millimeter level, and rotational accuracy on the sub-degree level [36].

Relatively little work has been done with regards to utilizing a 3D-to-2D registration techniques for the purposes of contact stress analysis, most likely due to the accuracy needed and the use of alternative methods such as muscle and ligament modeling. A particular study relating alignment error to repeatability of contact stress results computed in an artificial knee replacement found that even small errors in kinematic measurement can relate to large changes in contact stress [36]. It was reported that for a ±0.1mm or degree change in translation there were 204, 100 and 117% changes in contact force, pressure and area respectively. The degrees of freedom most sensitive to translation error were found to be superior-inferior translations and varus-valgus rotations. Utilizing load control in these directions was found to dramatically improve the contact stress results, with errors of ±0.5mm/degrees causing at most a 3% change in reported contact stress [36]. This suggests the need for extreme accuracy if contact stress is to be computed using purely alignment-based kinematics. Otherwise, load control needs to be used wisely in degrees of freedom which are particularly sensitive to error.

4.2.2 Implementation of a Functional 3D-to-2D Alignment Algorithm

There are many 3D-to-2D alignment algorithms which have been written and demonstrated for a wide variety of scientific applications. In the field of orthopaedics digitally reconstructed radiographs (DRRs) are mainly used to find alignments between a source CT dataset and an x-ray. DRRs are generated by using intensity information from a source CT imaging volume as a surrogate for material density. This 3D density volume can then be used to simulate the attenuation of x-rays projected through the volume. This can be repeated many times to generate many different poses of the 3D volume. This methodology however, is limited to CT-derived 3D datasets, due to the fact that DRR requires use of a signal intensity which can be related to density. This is not possible for MRI images and thus is not suitable for the present application. Another 3D-to-2D registration method which has gained some traction in the field orthopaedic biomechanics is JointTrack software (JointTrack, University of Florida, (http://sourceforge.net/projects/jointtrack/) [80, 88-90]. JointTrack is feature-based 3D-to-2D registration methodology focused on alignment of 3D models to fluoroscopy images. It uses a silhouette projection system implemented in ITK and VTK, along with a built-in Canny edge detection procedure to generate its objective function. There is limited ability to adjust contrast or to select specific edges of interest. JointTrack is based on an initial user alignment of the 3D model using a 3D GUI and a mouse and keyboard interface, to roughly align the model to the objective function. Following this step a local optimizer can be used to refine the alignment obtained. Global optimization is precluded in JointTrack due to the large amount of time that each individual cost function evaluation takes, compared to the number of iterations of the optimizer require to achieve a consistent result. Additionally, JointTrack was designed for low resolution fluoroscopy images (512x512 resolution), and as such, optimization scales poorly with increasing image size. The large high resolution images (2530 x 2043 resolution) to be used in the registration of PA standing radiographs require a large amount of time to be computed through the optimizer. Additionally, as JointTrack requires an initial manual registration step combined with a local optimizer, there is a level of inconsistency introduced due to a hand pre-registration step. The significant computation time for optimization combined with the poor repeatability of initial hand registrations made JointTrack an unsuitable option for use in this study. Instead, purpose written registration method was created which used a similar silhouette edge matching technique as that of JointTrack. This new method benefits from a faster cost function evaluation for more robust optimization, and from lack of a user-based pre-registration step to help reduce user variability.

A 3D-to-2D registration algorithm written in MATLAB was created to provide a purpose-written, expeditious, robust and highly configurable system for alignment of models to x-rays. The system was written to be generalizable to a wide variety of applications with minimal parameter tweaking between models, in order to be useful for computing hundreds or thousands of alignments. It also was made to require very little user intervention, in order to mitigate user-to-user variability as well as investigator time. The system begins with: (1) segmentation of the bony geometry from 3D and 2D images, (2) construction of a virtual radiographic scene, (3) formulation of a 2D goodness-of-fit cost function, (4) silhouette edge sampling of the cost function, and (5) optimization of the alignment, based upon the cost function.

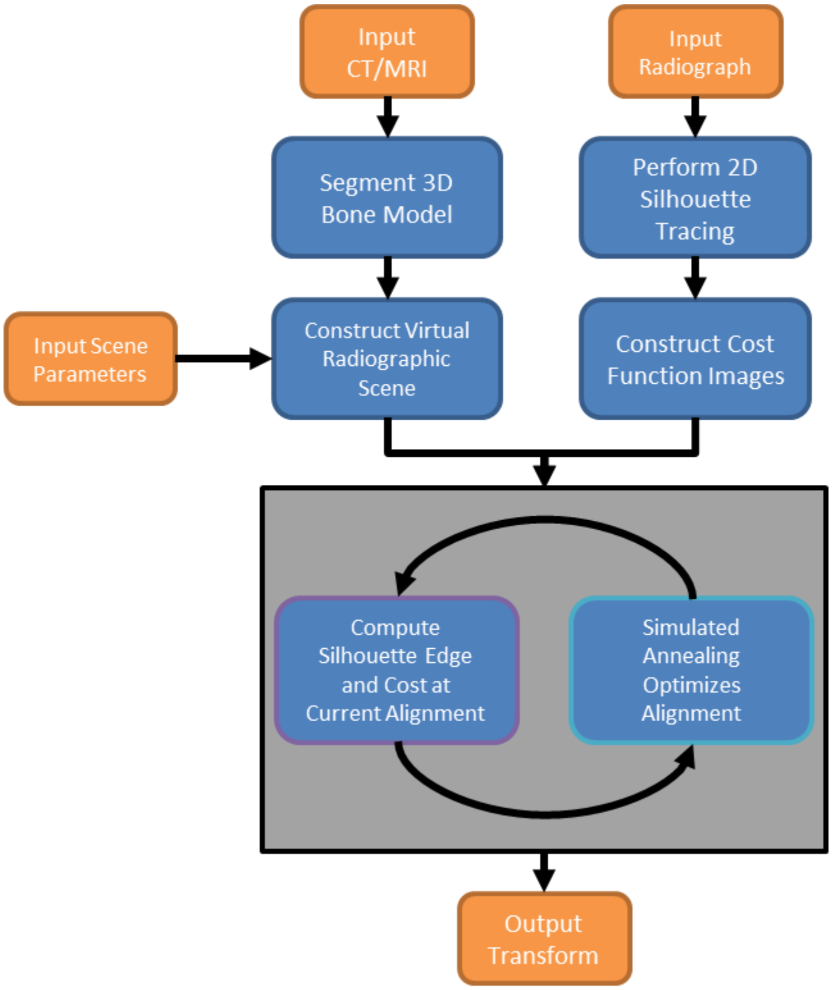

Figure 30. Flowchart of an overall 3D-to-2D alignment algorithm in which a 3D radiographic scene is recreated in a virtual environment using segmented bone models, radiograph segmentations and input scene parameters. Edge silhouettes from the bone models are projected onto the film surface using ray casting and the appropriate transformation parameters, to perform an optimal match between the bone edge silhouette and radiograph edge segmentation is computed.

4.2.2.1 Alignment Step 1: Segmentation

A 3D triangulated polygon surface of each bone is required prior to alignment. The model must be as faithful a representation of the native bone as possible, and may therefore involve only minor smoothing and editing. When read to the program, it is converted into a wing edge polygon representation [91]. A wing edge polygon mesh stores a 3D triangular mesh as a list of vertices (floating point 3D coordinates), faces (indices to the three edges which create a face) and edges (indices to two vertices which describe the edge, indices to the two faces which contain the edge, and indices to the other edges which connect to this edge). This allows for adjacency of polygons to easily be computed, along with computationally efficient traversal of holes and edges.

A 2D segmentation is required to demarcate bone edges on the radiograph for calculation of the objective function for optimization. A MATLAB function was designed to perform this task in a semi-automated manner. First, the user reads the desired radiograph into the software. The software then prompts the user to crop the image to the bone of interest. After cropping, the selected region of interest (ROI) undergoes adaptive histogram equalization to create even contrast and intensity throughout the ROI. The adaptive histogram equalization routine is a tile-based histogram equalization included natively in the MATLAB software. Following equalization, a Canny edge detector is used to find all edges within the ROI. Canny edge detection is a multi-step edge detection algorithm which is fast, robust and directionally independent [89].

Due to the possibility of wide variation in radiograph contrast and artifact, no single best set of parameters for the Canny edge detector can be chosen to detect only the bone edge. Instead, Canny edge detector parameters were chosen to effectively over-segment the image. A user is then able to interactively select only the relevant bone edges present in the image.

The user edge selection utilizes a MATLAB interface with two adjacent windows, one showing all possible edges, and a second showing the histogram-equalized ROI. A selection reticle is present in the edge window and is used to highlight a desired edge. The user can then choose to add or delete the highlighted edge from the corresponding final segmentation. The final segmentation is shown in real time, overlaid on the window with the histogram-equalized ROI. Throughout this process the user is also able to crop line segments from the final image, adjust contrast of the final image and adjust Canny filter sensitivity. When the user has finished selecting and editing bone edges, the segmentation routine closes and saves the final segmentation as a binary image file with the same dimensions as the input radiograph. This has proven to be a process which allows for expeditious edge segmentation with significantly less variability than a manual tracing of the image.

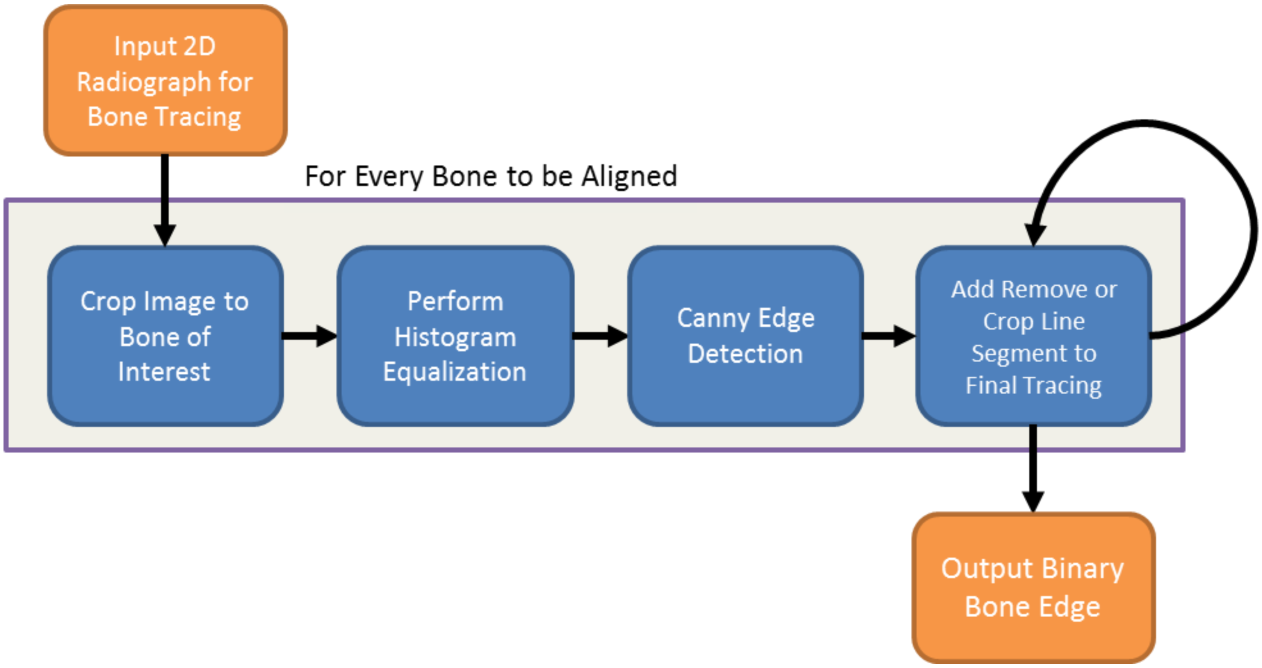

Figure 31. Flowchart of system for semi-automated segmentation of bone surfaces from radiographs using a MATLAB GUI.

Figure 32. Edge selection program for cost function construction. Two windows are present: one showing Canny detected edges (left) and one showing final edge selections (right). The user is able to add, remove and crop edges from the final image using a set of built-in tools.

4.2.2.2 Alignment Step 2: Construction of Virtual Radiographic Scene

Once a surface model containing the 3D object and a 2D segmentation of the radiograph are obtained, initialization for the alignment can begin. First, the radiographic scene must be created within the virtual space. Parameters are input by the user to recreate the positioning of the film and the x-ray source used to obtain the 2D x-ray. Required parameters are film size (in cm), film position, x-ray source position, and a nominal starting position for the 3D bone model.

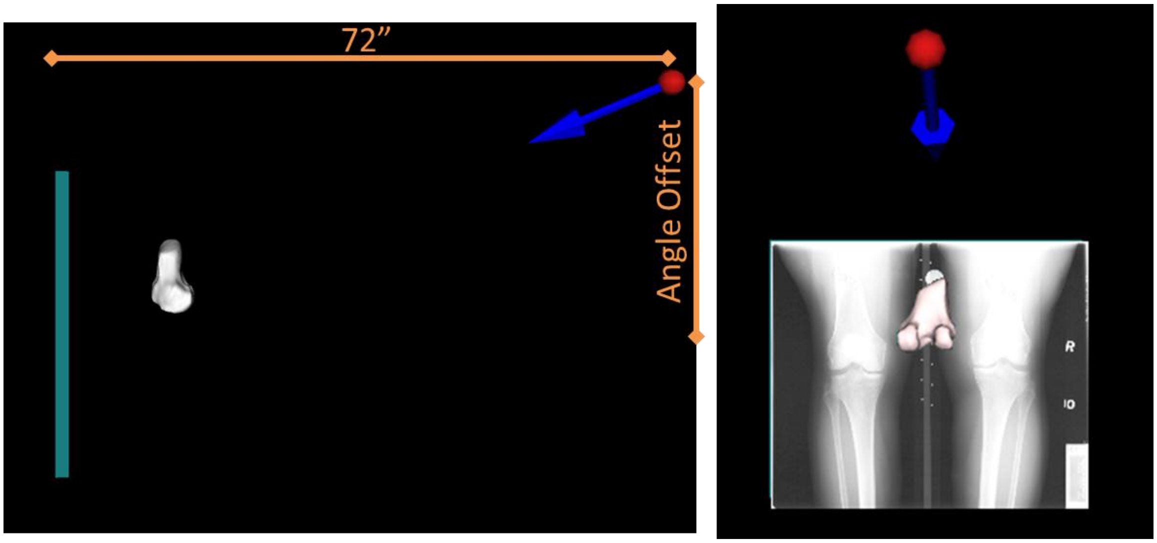

Figure 33. Example of virtual setup of radiograph (not to scale). X-ray source (red sphere) is placed 182 cm perpendicular to film (teal) in accordance with MOST radiographic protocol. Source is offset vertically with respect to radiograph to adjust for the angle offset of the original radiograph. Bone model is placed in a nominal starting position for alignment near the central region of the radiograph.

The radiographic film is simulated as a pair of congruent triangles matched upon their hypotenuse to form a quadrilateral. The triangle vertices are dictated by the film position and film size (Figure 33). The x-ray source is modeled as a point source, from which all beams of the x-ray originate. The film and the x-ray source provide the basis for creating 3D-to-2D projections for comparison to the existing radiograph segmentation (Figure 33).

4.2.2.3 Alignment Step 3: Cost Function Formulation

The radiograph segmentation is next loaded into the program and used to formulate a 2D cost function for evaluating the fit of the alignment. First, a distance transform is performed over the entirety of the image. The distance transform calculates the chessboard (orthogonal and diagonal adjacency) distance of every black pixel on a binary image to the nearest white pixel. The resulting image viewed topographically appears as a valley in the shape of the user edge tracing, with the slope of the valleys rising linearly with distance from the edge tracing (Figure 34). This distance transform image is saved as one component of the cost function. It has an influence over any projection upon the film, thus increasing the capture range of the optimization [79].

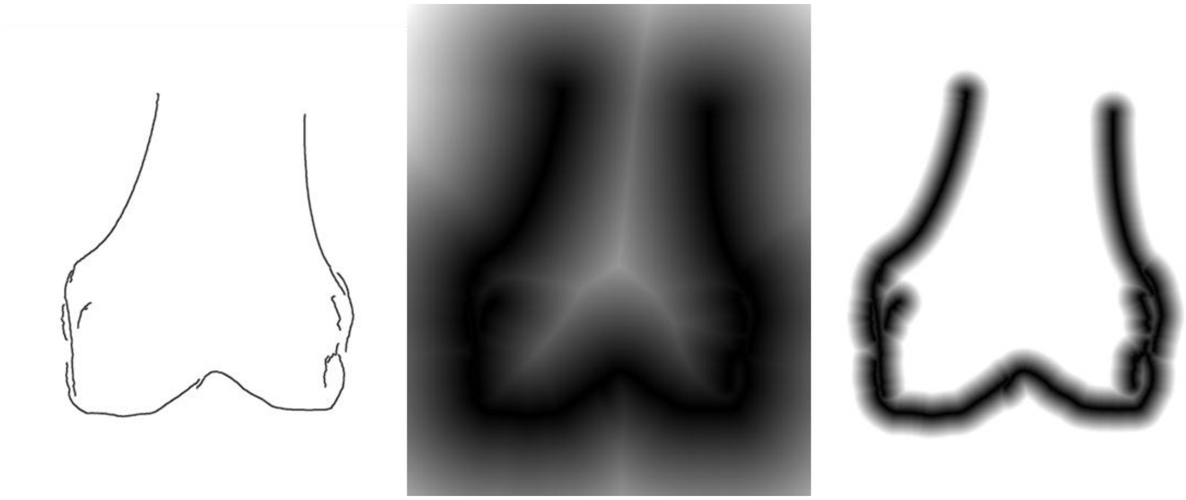

Figure 34. Line tracing of AP femur radiograph from semi-automated segmentation routine (left) shown with generated cost functions for alignment. Large capture region portion of cost function (center) is generated by performing a distance transform on line tracing. Small capture region (right) portion of the cost function formed by creating a local distance transform from the line tracing. This allows for local optimization of the 3D-to-2D alignment, while penalizing minimally for having regions segmented outside of capture region.

A second component of the cost function is formulated by subtracting a user-supplied value from the distance transform and culling all values which are greater than zero. This has the effect of creating an image with a flat topography of value zero, and a small ridge of negative values surrounding the edge segmentation (Figure 34). The value to be subtracted from the distance map can be empirically selected to best fit a given alignment task. This portion of the cost function provides a very small capture region, but it provides very little penalty for evaluating the cost function outside of the tracing regions. This is important for situations when there is significant mismatch between the 3D model and 2D segmentation, discrepancy which can be caused by MRI, CT or radiograph artifact, segmentation error, and poor spatial resolution.

These two cost function elements can be weighted differently depending on the alignment task. In preliminary development work it was determined that it is typically advantageous to weight the global distance map image at 1/3 the level of the more local (smaller) capture zone image. This provides a weak but large capture range for initial alignment and a much stronger but smaller capture range as the model approaches optimal alignment.

4.2.2.4 Alignment Step 4: Sampling the Cost Function

Once the cost function is formulated, a projection of the 3D model to the film is used to efficiently and rapidly evaluate the cost function. This is done by rapidly detecting silhouette and internal edge vertices from the 3D bone model and projecting these vertices on the film using the x-ray point source.

A computationally efficient ray casting based method was developed for projecting silhouette edges of a 3D model onto a film surface. The most computationally expensive step in all ray casting applications is detecting ray-polygon intersections. Other ray-casting based x-ray simulation or DRR methods require a ray to be cast through every pixel of a film and intersected with every polygon in a model, thus making it computationally inefficient [79]. The method presently adopted significantly limits the numbers of rays that are cast as well as the number of polygon intersections, by only shooting rays through silhouette edges of 3D models and intersecting those rays only with the two polygons of the film.

The chosen method begins with the finding of polygon edges which denote silhouettes edges of the overall model. Polygon edges are defined as a line segment connecting two adjacent polygons or two adjacent points on the edge of a polygon. A silhouette edge can be computed by finding an edge which connects a front facing and rear facing polygon. First, vectors are computed between each polygon centroid and the x-ray source. This represents the direction of the incident ray on the model. Next, a dot product is computed between the x-ray vector and each polygon normal. A search is then computed to find all edges which have both a back and front facing polygon connected to them. Silhouette edges are defined as edges between a front and back facing polygon. Back facing polygons are polygons in which the dot product of the x-ray vector and the polygon surface normal is negative. Front facing polygons are polygons in which the dot product of the x-ray vector and the polygon surface normal are positive (Figure 35). [92]

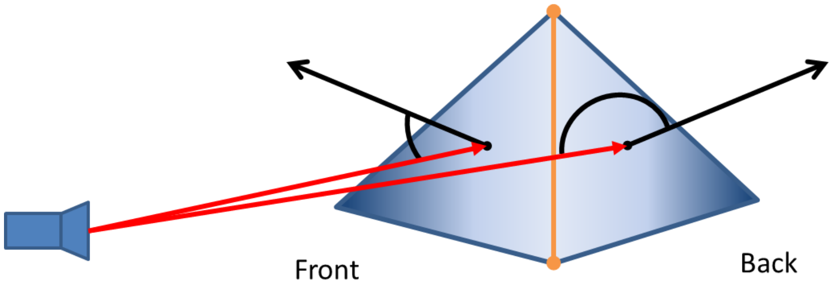

Figure 35. Silhouette edges (orange) are found by finding polygon edges which share front and back facing polygons. Polygon directions are found by shooting a unique ray (red) from the x-ray source (left) to each face in the model. The magnitude of the angle between the ray and polygon face normal designates the direction a polygon is facing.

Once all silhouette edges have been identified, rays are cast from the point source through the vertices of each silhouette edge segment and are intersected with the film plane. Since the film plane consists of two triangles, a set of intersections is computed between all rays and each triangle of the film. Ray-triangle intersections have been used extensively in the field of computer graphics and physics simulations for calculating the path of incident light beams and their reflections [93]. Each ray is a parametric representation of a line, where a point on that line (P) is described by its origin (P_0), a distance along the line (t), and a unit vector of the line's direction (v).

$$P = P_0 + t * v$$

The triangle is first described as the parametric equation of a plane described using a point on the plane (P), a unit normal vector (N), and a constant (d).

$$P \cdot N + d = 0$$

One can then substitute for P and solve for the distance along the line (t), to obtain the equation for a ray-plane intersection.

$$t = -(P_0 \cdot N + d)/(V \cdot N)$$

Solving this equation for each ray and plane will determine which rays intersect with the planes of the triangles and where each intersection point (P) occurs. Next, the barycentric coordinates of the intersection point on the triangle are computed. Barycentric coordinates are a way of representing any point on a triangle as a weighting of its three vertices, using three weighting values (u, v, w) (Figure 36) [94]. These three values are used to represent the location of a point on a triangle, with each coordinate representing a weighting of its corresponding vertices. The sum of these vertices must be equal to one. Thus the third value is implicit.

$$w = 1 - (u + v)$$

If the barycentric coordinates are valid (i.e., all values are < 1 and >0) then the intersection point is deemed to be valid [95]. Once intersection points for all rays are computed, then the barycentric coordinates are mapped to pixel locations on the cost function image.

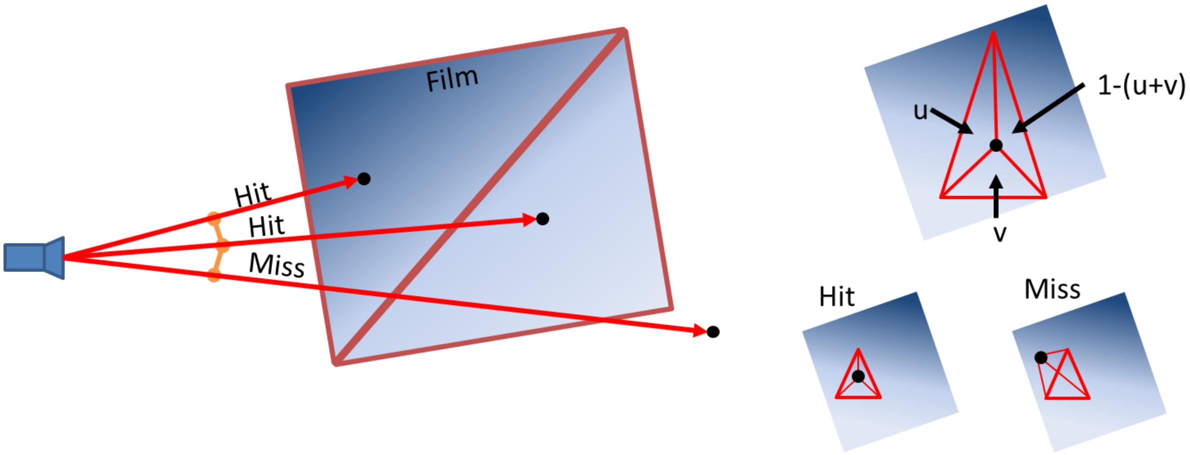

Figure 36. Rays are shot through detected silhouette edges (orange) and intersected with the two triangles which comprise the film (left). The first ray is intersected with infinite plane containing the triangle, to determine hit location. Next, barycentric coordinates of hit location are computed with each triangle. This determines whether the hit point is within triangle boundaries (right).

Mapping hit points on the film plane to pixel coordinates on the cost function is done using a process similar to texture mapping in computer graphics. In this process the texture (cost function) is parameterized and mapped to physical coordinates on a surface using values (0 to 1) to represent the vertical and horizontal directions on the image. Each vertex representing the film plane in the image is assigned a coordinate in parametric space corresponding to its relative position on the film. These parametric coordinates allow for simple translation between locations on the image and corresponding locations on the film. The barycentric coordinates of ray-triangle intersections, when combined with corresponding parametric coordinates, will produce a collection of parameterized texture hit points. These can easily be backed out into actual texture coordinates for sampling the cost function (Figure 37).

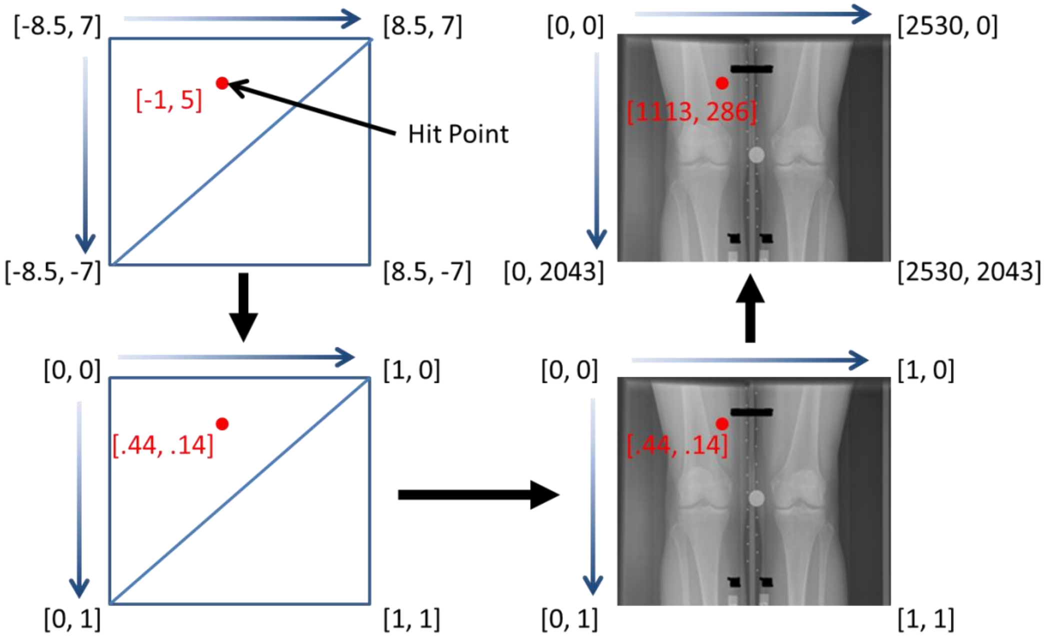

Figure 37. Physical coordinates from intersections of ray and film are parameterized and mapped to pixel coordinates of the radiograph. Each vertex from the film is assigned a texture coordinate in addition to its physical coordinate (lower left). Barycentric coordinates from ray-triangle intersection can be used to find texture coordinates of hit points. Radiograph texture is also parameterized to match virtual film coordinates (lower right). These coordinates are then converted into image pixel coordinates for image comparison (upper right).

Once silhouette ray hit points have been determined, they exist as a collection of individual coordinates in the space of the image. A continuous line is necessary for cost function evaluation. This line can be achieved by connecting points which share an edge. Points on a 2D integer coordinate grid can be connected rapidly and effectively using a Bresenham’s line drawing algorithm. The Bresenham’s line drawing algorithm is a rapid integer-based algorithm for drawing lines on a 2D surface, commonly used in computer graphics [96].

Following line construction, the ray-traced silhouette is now present as a set of coordinates which represent a continuous edge (Figure 38). Each of the cost function images is then sampled using the edge coordinates representing the silhouette. The mean value for each cost function image is scaled with a user-input weight and added, to find the total cost for that specific bone pose in space.

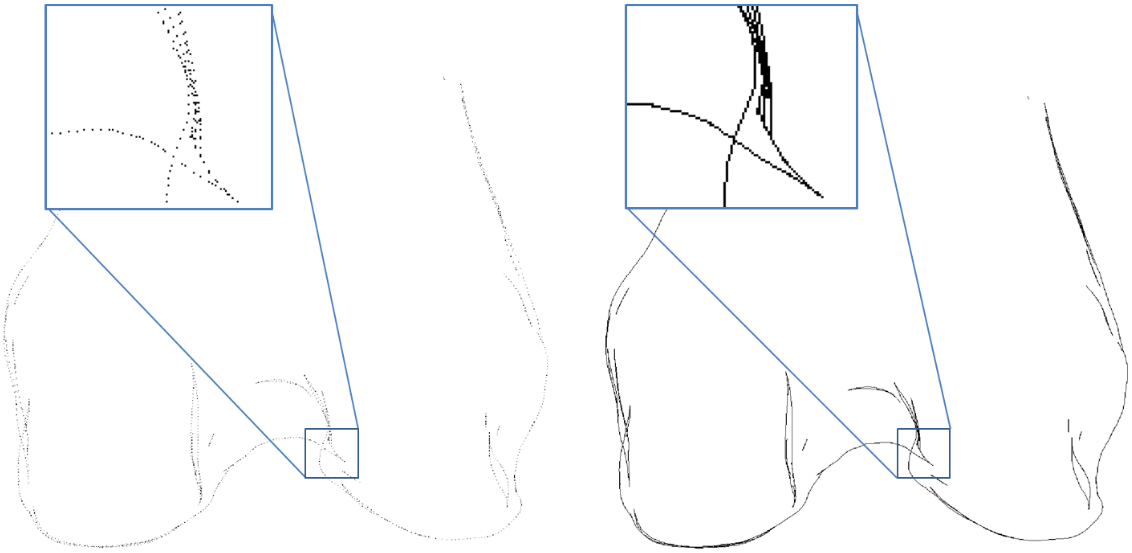

Figure 38. Image showing ray hit points sampled as image pixel coordinates on the virtual film (left) along with image showing detected silhouette edge following connecting ends of corresponding rays using Bresenham's line drawing technique (right).

4.2.2.5 Alignment Step 5: Optimization

A robust optimization routine needs to be used to obtain the global minima for each specific cost function. Simulated annealing (SA) has been selected for this purpose due to its general robustness with high-dimensional problems and its ease of implementation [97]. SA is a heuristic global optimization algorithm which performs a Monte Carlo sampling of the state space describing the problem. The SA algorithm avoids being stuck in local minima by allowing uphill moves as well as downhill moves within the cost function. It is analogous to the annealing of a metal in that a temperature variable (T) controls the internal "energy" of the system. When the simulation starts, T is large and allows both uphill and downhill moves in the cost function. The propensity of the simulation to accept an uphill move is determined by the Metropolis-Hastings criteria [98]. The probability (p) of an uphill move, is defined as the exponent of the difference between the new cost function evaluation f' and the current evaluation f divided by the system temperature, T.

$$p = e^{\frac{f' - f}{T}}$$

If the probability p is greater than p', (a randomly generated number [0 to 1]) then the uphill move is accepted. As the simulation continues the system begins to "cool" (i.e. T is reduced). A smaller T value reduces the value of p, constraining the algorithm to smaller and smaller uphill moves by the optimization. Eventually when the system is fully cooled (i.e., T approaches 0) no further uphill motions are allowed and the system switches to a local greedy optimizer.

The simulated annealing algorithm used was implemented in MATLAB and is based upon the work of Goffe et al. [97]. This is a slightly modified SA algorithm, which stores both the current and best answer of the evaluation and rescales the sampling range dynamically. The optimizer begins with a user set temperature (T), a 6x1 vector representing an initial Euler transform (X), a 6x1 vector representing initial step lengths for perturbations (V), a cooling schedule (tSched) which represents the rate of cooling of the optimization, and two values Ns and Nt which represent the number of iterations to run SA before adjusting parameters.

When operating as a minimizer the SA algorithm begins by computing the cost of the initial Euler transform X and recording the cost and position as the best obtained. A perturbation is then added by taking a random element of the Euler transform X_i and perturbing it by a random value range [-1 to +1]*V_i. A new cost function evaluation (f') is then executed at this new state. If f′ is less than f, then f′ is immediately accepted as the current state (f). If f′ is greater than f then f′ is accepted only if the Metropolis-Hastings criterion is evaluated as true. Additionally, if f’ is less than the lowest cost function evaluation (f”), then f’ is recorded as both f and f”. This is repeated for all 6 dimensions of the Euler transform in a random order and constitutes a single iteration of the optimization process.

After every Ns iterations X is set to X” so as to reset the optimization in the current best position and to “re-center” the optimizer on the current best position. Also, the step size V for each dimension is rescaled so as to accept approximately 50% of the cost function evaluations. If acceptance for the previous Ns iterations has been less than 40% then the step size V is decreased, thus shrinking the sampling space and leading to smaller gains in cost function for subsequent steps. If acceptance for the previous Ns iterations has been greater than 60%, then the step size V is increased, thus widening the sampling space and increasing the change in the cost function for subsequent steps.

After every Nt*Ns iterations the temperature is reduced by the amount prescribed in the cooling schedule (tSched), which is a user-input function for reducing the value of T. This has the effect of reducing the number of uphill movements by the optimization, and therefore the size of the sampling space.

The optimization is terminated once T has been reduced to a pre-determined value T_{final} or if the termination criteria have been met. If Ns*3 iterations of C(current) are within a ± 0.001 margin of one another then the simulation is deemed to have converged upon a global minimum. Also, if Ns*3 consecutive function evaluations have been rejected then the solution is deemed to have found a global minimum.

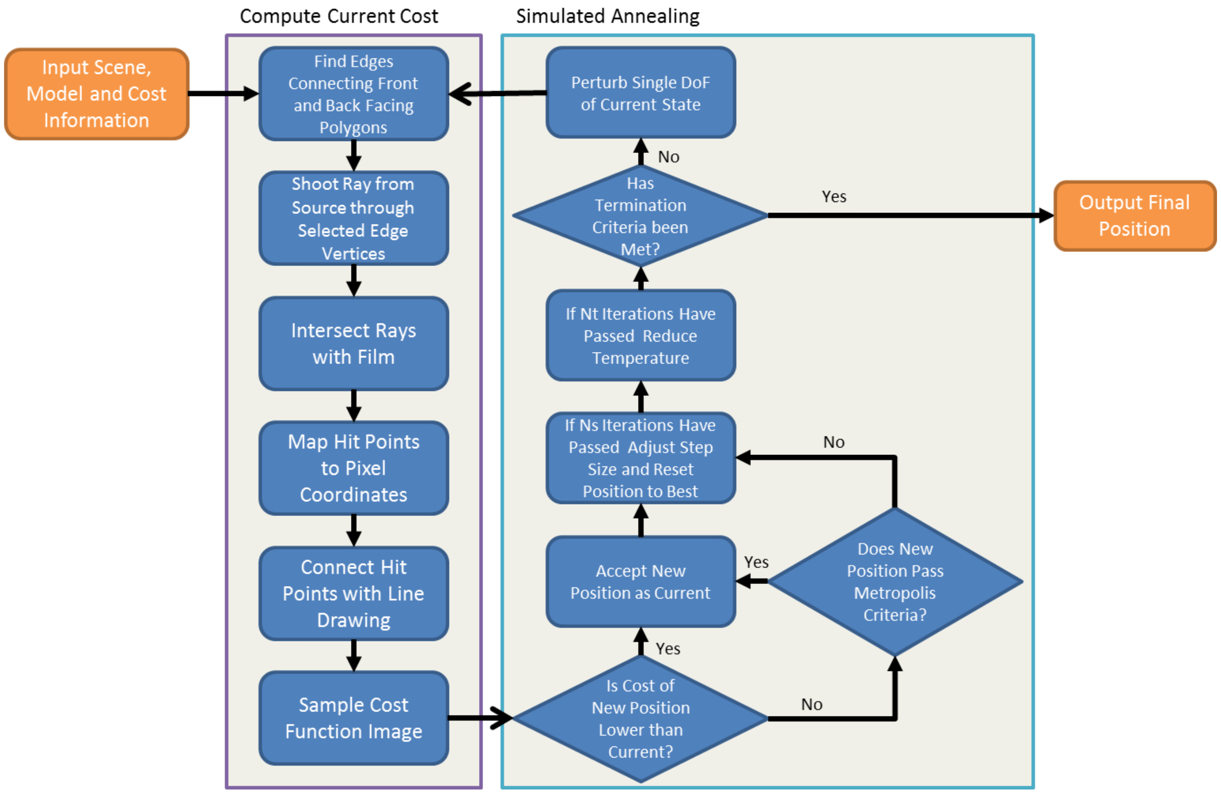

Figure 39. Flowchart of implemented 3D-to-2D alignment algorithm in which a cost function, scene information, and segmented 3D models are input to the algorithm. Silhouette edges from the 3D model to the film are traced using a ray casting algorithm to simulate the x-ray setup. A simulated annealing optimizer is used to optimize the match between a previously segmented radiograph edge and a computed silhouette edge.

4.4.4.6 Parameter Selection

Parameters for the optimization are required to be selected empirically based on trial runs [97]. Ns, Nt, tSched, T_{final}, and cost function weighting all need to be evaluated and tuned to the problem at hand. This was done by preparing several example cases with knee models and their corresponding radiographs. Parameter sweeps were performed for Ns, Nt, tSched, and cost function weighting. Results for these sweeps were compared and parameters were selected based upon the results which consistently provided a final optimization which visually matched the bone edge when projected on the image. Parameters were tuned using several different datasets. The first was a sphere model made using Geomagic Studio. A target image of this model was created using the ray casting algorithm to create a projection edge of the model at a known position in space. The model was then moved to a random location in space and the optimization procedure was run. This is a test purely for the translation component of the alignment since a sphere's projection is independent of rotation about its center. Parameters were selected so that from any starting position in space, the original projection position could be recreated to within 0.1 mm.

Once this trial was completed a test case was used with a randomly selected femur model. The same procedure was used by creating a silhouette of the femur using the ray casting algorithm and then moving the femur to a randomly selected position in space and re-aligning it to the silhouette. This was done to test rotations and translations in the alignment procedure with an "ideal" picture. In an actual alignment there would be inevitable error between the ray cast silhouette of the bone and radiographic edge tracing of the bone.

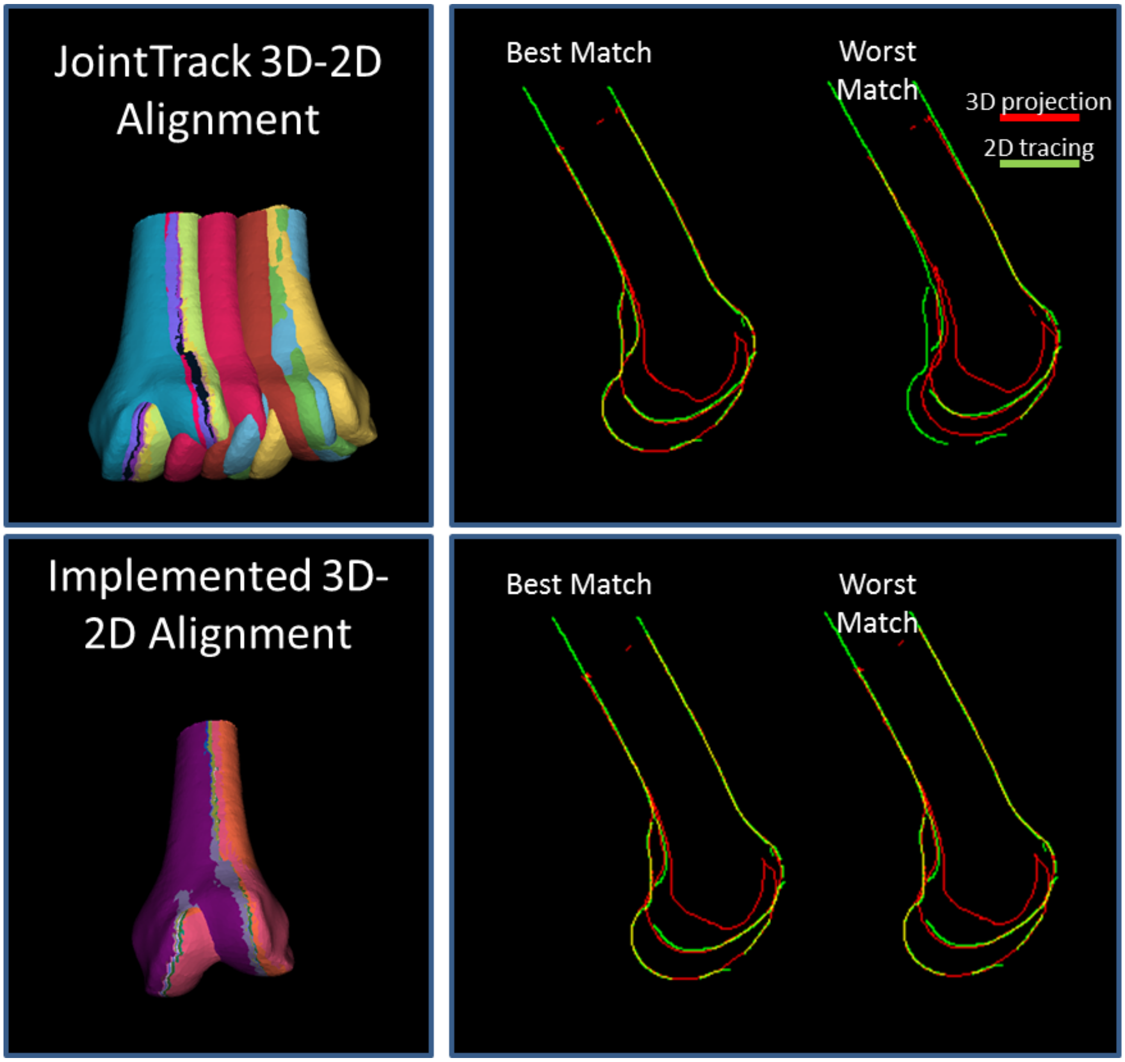

Figure 40. A test case of a 3D femur model and its corresponding 2D fluoroscopic image was used to evaluate the reproducibility of alignment in JointTrack and the present purpose-written alignment algorithm. Ten alignments were computed from a consistent starting alignment using the provided computational optimization procedure with each method. 3D renderings of the final alignment are overlaid (left). The best and worst alignments obtained are shown as 2D silhouette drawings. The quality of alignment is determined by the returned cost of the objective function for each methods optimization(right).

The next step was to use an example dataset from JointTrack. The JointTrack example dataset provided online consists of a sagittal fluoroscopic image of a femur, a femur model which corresponds to this image, and a set of calibration parameters to recreate the radiographic scene. This dataset allows JointTrack and our alignment technique to be compared with regards to final selected alignment, as well as to the variability present between multiple consecutive alignments. Our alignment technique was set up to properly replicate scene parameters (i.e. detector and source locations and angles) from the JointTrack calibration file. Bone edges from the fluoroscopic image were traced using the previously discussed 2D segmentation technique. Ten consecutive alignments were computing using both JointTrack and our alignment technique. Final alignment and variability measures were used to compare the two techniques based upon the 10 consecutive trials computed (Figure 40, Figure 41).

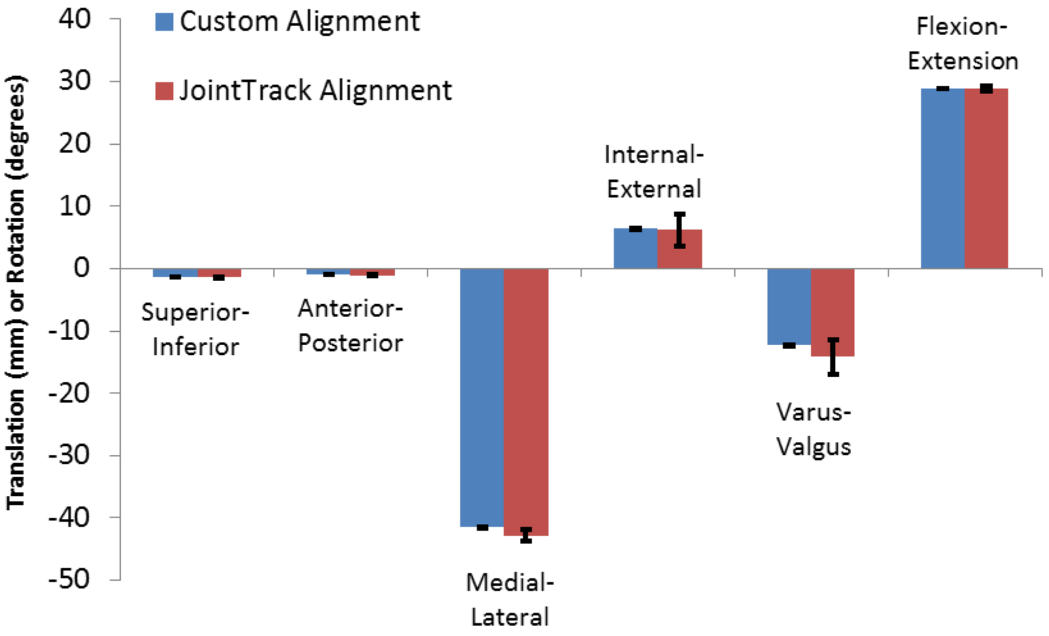

Figure 41. Comparison of resulting mean transforms using the present alignment versus JointTrack alignment algorithms after ten repetitions. Results are in the form of translations (first three groups) and Euler rotations (last three groups) from the starting position of the bone model. Error bars represent ± 1 standard deviation.

4.3 Implementation of 3D-to-2D Registration Techniques and Expedited Contact Stress Computation on 38 Subject-Specific Human Knee Models

Thirty-eight subjects from the Multi-Center Osteoarthritis (MOST) study cohort were selected for expedited contact stress analysis [63]. The MOST study is a cohort of 3,026 adults who are have or are at high risk for knee OA, ranging from age 50-79 years [63]. Subjects for this study were selected to have: (1) no missing baseline or 30 month MRI readings for cartilage morphology or BMLs, (2) presence of case and control sub-regions for BML changes or cartilage morphology changes, (3) a radiographic knee OA score (KL ≥ 2) at baseline, and (4) consistently denied knee pain or stiffness prior to enrollment.

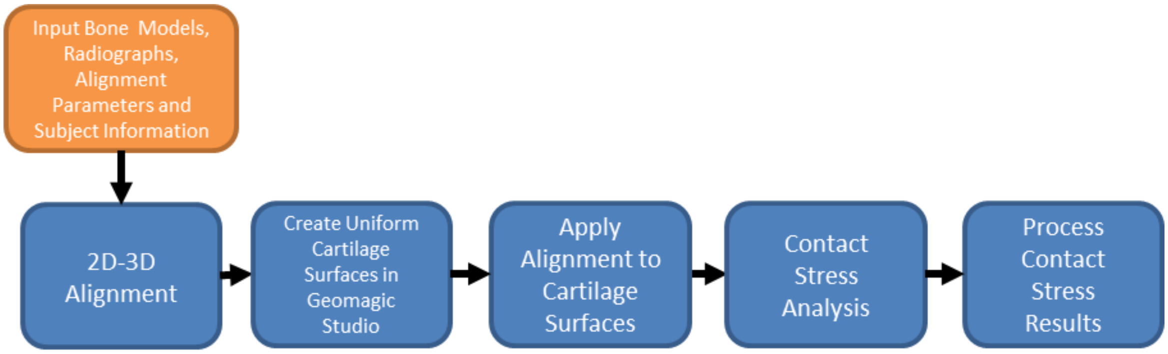

Figure 42. Flowchart of system for subject-specific alignment and contact stress evaluation of human knee models.

4.3.1 Model Creation

Knee MRIs were previously performed on a 1.0T dedicated knee system (ONI Medical Systems, OrthOne™). The protocol included axial and sagittal proton-density weighted fat-suppressed (PDFS) fast spin echo sequences (TR 4800 ms, TE 35 ms, 3.0 mm slice thickness, 0.0 mm interslice gap, FOV 14.0 cm2, matrix 288 x 192, echo train length (ETL) 8) and a STIR sequence in the coronal plane (TR 6650 ms, TE 15 ms, TI 100 ms, 3.0 mm slice thickness, 0.0 mm interslice gap, 256 x 192 matrix, FOV 14.0 cm2, ETL 8). Tibio-femoral geometry was hand-segmented from baseline coronal MRI scans using an interactive pen display and OsiriX software (The OsiriX Foundation, Geneva, Switzerland).

The resulting segmentations were output in point cloud format, converted to .ply files and wrapped in Geomagic Studio Software (Geomagic, Inc., Research Triangle Park, NC). Geomagic Studio is reverse engineering software designed for converting 3D scan data and polygon meshes into usable CAD surfaces. This software package contains many polygon meshing, smoothing and manipulation tools which are useful for creating 3D surface models from 3D point cloud data. Perhaps the most enabling feature for the use of Geomagic studio in large-scale contact stress evaluation studies is the ability to generate scripts. These scripts enable fully automated loading, meshing, smoothing and manipulation of 3D point cloud data across hundreds of models. All scripting done for Geomagic was in the Python computer language.

A Geomagic script was created to load individual point clouds and to wrap them using a point spacing of 1.5 mm, combined with Geomagic Studios' hole filling algorithm to repair any gaps in the bone model. If any significant holes existed on the contacting surface of the bones, the model was re-wrapped with larger point spacing to achieve a continuous articular surface with as little interpolation as possible. All holes on the models were filled except for at the distal and proximal ends of the tibia and femur, respectively. Following wrapping and hole-filling, the model was refined to roughly 100,000 faces, smoothed, and then immediately decimated to 10,000 - 15,000 faces. Each bone model was saved as an independent binary STL file for use in alignment and contact stress computation.

4.3.2 Model Alignment

A standing fixed flexion postero-anterior (PA) radiograph was taken for all subjects within the MOST cohort, using a consistent set of radiograph parameters. These radiographs allow for a subject-specific alignment to a functional loading, thus taking into account the effect of subject-specific alignment in generated contact stresses. The previously described 3D-to-2D alignment system was used to align 38 knee joints to corresponding standing fixed-flexion PA radiographs.

The standard radiographic acquisition protocol from the MOST study was used to recreate the radiographic scene in a virtual environment in MATLAB. The x-ray source was treated as a point source, and the detector was treated as a 35.6 x 43.2 cm plane made of two triangular faces. The film-to-source distance was 182.9 cm orthogonal to the plane of the film. The source was placed at a 5, 10 or 15 degree caudal angles to the film, depending on the recorded acquisition protocol. To enforce the angle of the x-ray beam relative to the film, the source was offset vertically to control the angle of the incident beams (Figure 33).

Femur bone models were loaded to the radiographic scene with the origin of the model corresponding to the origin of the scene. The alignment optimization was set up to constrain the femur bone to reasonable bounds within the simulation. Bone could not travel past the film, rotate more than ±90 degrees, or travel behind the source. The femur was allowed to translate from the plane of the detector to an offset 1000 mm orthogonal to the detector. Translations in directions parallel to the film plane were controlled using the cost function evaluation, by assigning an infinite cost to any ray which missed the film, ensuring rejection by the SA optimizer. This prevented the bone from traveling outside of the ‘pyramid’ of space created between point source and the edges of the film. Rotations were constrained to ±90 degrees from the initially loaded position of the bone. This prevented the optimization from sampling any grossly implausible alignment situations, as well as preventing any Gimbal lock that otherwise might arise.

Tibia bone models were aligned following the femur alignment by using the femur alignment transformation as an initial starting point. The tibia was constrained in the optimization to have a much smaller sampling window (± 5cm translation from the femur in any direction, ± 15 degrees from the femur alignment except in flexion-extension).

Due to the fact that the alignment utilized a heuristic Monte Carlo simulation, the same "optimal" answer is not always produced. Each alignment was performed four times, and then averaged to find an approximate optimal solution. An inter-and intra-user variability study was also conducted, to ensure that differing tracings of PA fixed flexion radiograph did not produce significantly different contact stress results (Table 1).

4.3.3 Knee Loading

Following alignment, the knee models were prepared for contact stress evaluation. Due to the substantial distance (182.9 cm) between the detector and x-ray source for the fixed flexion radiographs used for alignment, there is poor sensitivity to in-and out-of-plane translation of the femur relative to the film. This imprecision of out-of-plane translation can introduce errors in the joint spacing, which would lead to inaccurate contact stress measurements if solely the registered apposition were used in contact stress assessment [36]. To address this issue, the femur was translated superiorly relative to the tibia until the surfaces were no longer in contact. Subject-specific loading of ½ body weight was applied to the joint to approximate the loading challenge present to the subject. All other degrees of freedom were constrained in the contact simulation.

4.3.4 Cartilage Surface Creation

Due to the low spatial resolution of 1.0T MRI scans, it was very difficult to segment cartilage and meniscus surfaces. The subjects used in this study had a history of knee injury and joint pain, indicating some level of cartilage degradation, thus making "one size fits all" uniform cartilage thickness a tenuous assumption. Instead, cartilage was modeled as a subject-and compartment-specific uniform thickness extruded from the underlying bone surfaces. This thickness was obtained by performing a distance transform between the bone surfaces in the MRI-imaged resting apposition. It was assumed that there was just “kissing” contact between the cartilage surfaces in each compartment while lying in the MRI scanner. Therefore, the minimum distance between apposing bone surfaces was used. Each bone surface was imported to Geomagic Studio and cropped to relevant contacting surfaces. Following the cropping, a 3D offset operation was used on both the tibia and femur surfaces, with the offset proscribed as ½ the distance between the tibia and femur bones in MRI alignment. This was performed separately for each compartment of the knee. In each case it was visually verified that the cartilage surfaces had “kissing” contact.

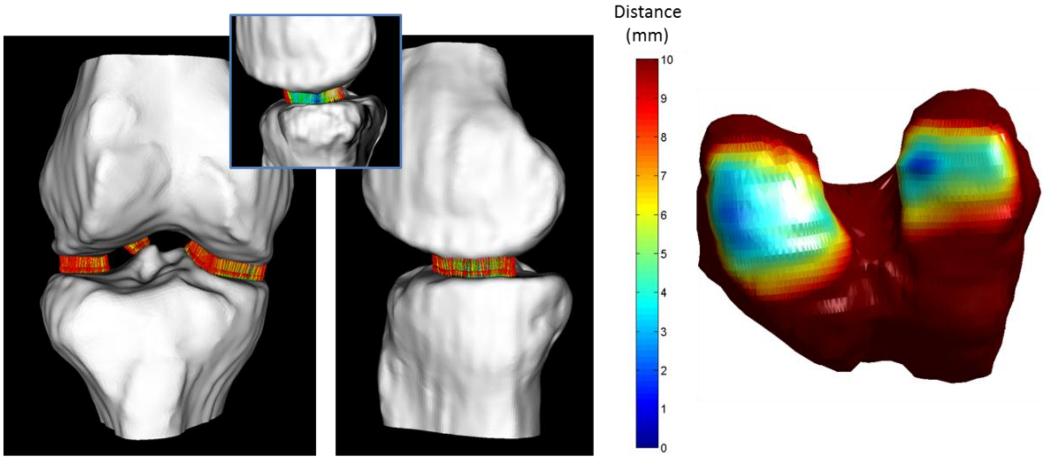

Figure 43. Cartilage thickness measurement is computed by measuring distance between bone surfaces from segmentation apposition.

4.3.5 Knee Contact Stress Evaluation

The previously described DEA contact stress routine was used to evaluate the contact stress between the cartilage surfaces of the 38 subject-specific knee models. Each knee cartilage model was read in, and then transformed using the Euler angles computed from alignment. Following alignment, the contact stress routine was run in load control. Computed contact stresses were stored in a results file for later processing.

4.3.6 Results Post Processing

Results for each of the 38 subjects were loaded and displayed onscreen in the form of a contact stress distribution. The user was prompted to separate the medial and lateral compartments of the knee using a mouse selection. Following this selection, mean and maximum contact stresses were recorded for both the medial and lateral compartments. The mean and maximum contact stresses were used for statistical analysis. A conditional logistic regression was used with baseline contact stress as the continuous predictor variable, and worsening of cartilage morphology and BMLs at 30-month follow-up as the dichotomous outcome variables. An M:N matched cases-control study design was used to eliminate between-person confounding. Statistical analysis was performed with SAS 9.2 with an alpha level of 0.05 set for statistical significance.

4.4 Results from Alignment and Contact Stress Evaluation in 38 Subject-specific Knee Models

The custom designed feature-based alignment algorithm was shown to replicate transformation parameters similar to JointTrack, but with smaller standard deviations across the 10 runs performed (Figure 41). Medial-lateral translation, internal-external rotation and varus-valgus rotation were all more variable in JointTrack than with the present custom designed alignment algorithm.

Inter-and intra-segmenter variability was found to be small with regards to the mean and max contact stresses found in medial and lateral compartments (Figure 44). Additionally, day-to-day alignment reliability was found to be excellent on the medial side, with Shrout-Fleiss reliability measure of 0.97 for maximum stress and 0.95 for mean stress [99]. The inter-user score was slightly weaker with 0.87 for max stress and 0.97 for mean stress. The lateral side was the weakest, with a Shrout-Fleiss reliability measure of 0.69 for day-to-day and 0.26 for inter user reliability measures. Since the alignment optimizer used a Monte Carlo simulation, the answer computed is not deterministic. Therefore, multiple runs of the optimizer needed to be made following each user line tracing. The Shrout-Fleiss reliability mean k score was used to determine reliability of the average of four trials done for each user line tracing. Taking the mean of 4 trials based off the same user line tracing improved the correlations of the alignment significantly, with the lowest reliability being in the lateral side with a value of 0.81 (Table 1).

Twenty-three of the 38 knees used in this study were female. Subjects had a mean age of 63.5±8.4 years and a mean BMI of 30.5±3.7 kg/m^2. The odds ratios for cartilage degradation and BML worsening in relation to baseline contact stress can be found in Table 2.

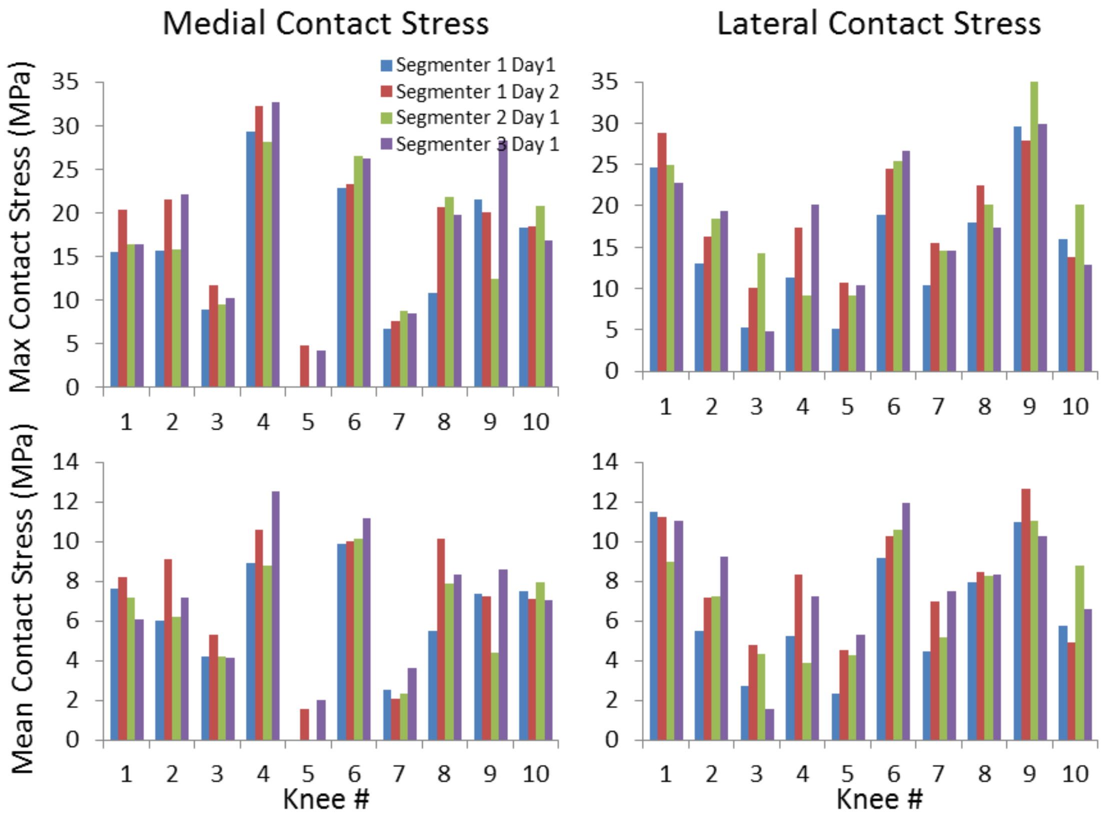

Figure 44. Contact stress results following segmentation reliability test. Maximum and mean contact stresses were recorded for both medial and lateral compartments, across three segmenters.

Table 1. Inter-Class Correlations for Alignment Variability Results

		Medial		Lateral	
		Max	Mean	Max	Mean
Day-to-Day	Single	.97	.95	.69	.68
	Mean	.99	.97	.81	.81
Inter-User	Single	.87	.76	.26	.26
	Mean	.99	.97	.81	.81

Table 2. Odds ratios for Cartilage Worsening and BML Worsening as a Result of Contact Stress Measured using DEA Across 38 Subject-specific Models from the MOST Cohort.

	Cartilage Worsening		BML Worsening	
	OR(95% CI)	p-value	OR(95% CI)	p-value
Mean contact stress	4.0 (2.5, 6.4)	<0.001	6.6 (2.7, 16.5)	<0.001
Peak contact Stress	1.9 (1.5, 2.3)	<0.001	2.3 (1.5, 3.6)	<0.001

4.5 Discussion of Results

Comparisons of the custom feature-based alignment algorithm with JointTrack using the sample dataset showed excellent results with regards to the amount of variability across 10 trials. Through visual inspection it is apparent that the amount of variability in medial-lateral translation is more substantial for JointTrack (Figure 40).

Mean values for alignment were also within 1 mm in translation and 1 degree in rotation. However, the variability present in the alignment methods is much smaller for the custom feature based alignment than the variability present in JointTrack. The observed reduction in variability was most likely due to the lack of a user-guided initialization step for the alignment and the use of more robust optimization criteria. Even though JointTrack likewise incorporates a simulated annealing global optimization algorithm, global optimization of a problem was deemed infeasible within JointTrack, due to the time it took to perform a single function evaluation. Simulated annealing requires, at a minimum, on the order of 10,000 iterations to achieve a valid global minimum, with some problems requiring even 100,000s of iterations [97]. Running this many iterations for the JointTrack optimization technique took days for a single solution to complete. Conversely, the present custom written feature-based alignment algorithm was written with the express goal of computationally simple cost function evaluation. The optimization was capable of performing 180,000 cost function evaluations within 20 minutes of computer time, which is roughly the amount of time the optimization takes to align a single bone. This allows for a global optimization to be run quickly and efficiently without the need for a user-guided initialization step.

When moving from the JointTrack example to segmentations from the MOST dataset, several additional issues came into play. First, the MOST radiographic protocol calls for a 182.9 cm perpendicular distance between the source and the film plane. This large distance makes the angle of incidence of the x-rays to the film extremely close to perpendicular. While this is advantageous for some aspects of the radiography, it makes determining in-and out-of-plane translation extremely difficult using only a single plane image for registration. Even large translations in-and out-of-plane (± 1 cm) were found to make very little difference on the resulting edge silhouette generated by the ray casting algorithm. This can result in variability in the final alignments arising from these radiographs, as the cost function is not well defined in this direction. In this study the poor precision with out-of-plane motion was countered by coupling the tibia alignment to the femur alignment and constraining tibia AP translation relative to the final femur result. In future work, inclusion of a second simultaneous-biplane radiograph could be used to improve the resulting alignment accuracy in the out-of-plane direction as well as all other directions [36]. Additionally, the models used were segmented from 1.0T MRI sequences with 3.0mm slice spacing. This large slice spacing undoubtedly introduced error to model segmentations, thus creating an inherent mismatch between the 3D model and the 2D line tracing from the radiograph. The effect of large mismatch between the 3D model and the 2D radiograph is unknown with regards to alignment accuracy, but it will most likely reduce consistency and physical relevance of the final alignment.

With regard to contact stress prediction reliability, it was found that both inter-and intra-user reliability ratings for segmentation with a fixed alignment and for alignment with a fixed segmentation were acceptable. This could potentially be improved as well by improving the quality of 3D model segmentation, by obtaining higher resolution 3D scans. Better 3D model resolution would improve matching between the radiograph contour and the model silhouette, thus improving the accuracy and consistency of alignment.

Due to the wide variations in subject joint space, it was deemed unrealistic to assume a uniform cartilage thickness that would be accurate across all subjects. Additionally, segmenting subject-specific cartilage surfaces from the 1.0T MRIs present in the MOST dataset was impractical, due to the poor resolution and contrast surrounding the articular cartilage surfaces. In lieu of a “one size fits all” cartilage thickness or subject-specific cartilage thicknesses, a single value for a uniform thickness had to be inferred based on joint spacing between the femoral condyles and the tibial plateau in the MRI resting apposition for each subject (Figure 43). While not optimal, this was the only measurement easily feasible with low-resolution MRI scans. Obtaining higher resolution

MRI images would allow for direct segmentation of cartilage surfaces for use of subject-specific cartilage thicknesses as well as subject-specific bone models.

Even with the shortcomings of low resolution 3D datasets and single plane radiographs, the odds ratios for BML worsening and cartilage degradation were significant with the reported contact stress values. This indicates that as the contact stress increases at baseline, risk for cartilage morphology worsening and BMLs worsening also increases significantly. These findings are consistent with the fact that BMLs are associated with joint pain, cartilage degradation and other knee symptoms, and it suggests that the DEA methodology used is suitable and valid for predicting knee OA risk. In the future this method may be used to inform and guide therapeutic treatments as well as to aid in determining the efficacy of prospective therapeutic interventions.

Strengths of this approach include the use of subject-specific models, alignments, lack of an FEA meshing step, and rapid computation time. Subject-specific models are important due to the structural variability present in all biological specimens, and given the sensitive nature of contact problems. Accurate subject-specific models are necessary to capture the complexities of the articulation that would otherwise be lost. Subject-specific alignment is also important due to the nature of the subjects used in this study. Many standing PA radiographs of the subjects showed significant variations in alignment from subject to subject. A universal alignment procedure would fail to capture these variations in alignment. Additionally, it has been shown that joint alignment plays a large role in the presence and resolution of joint pathology [100]. Thus, capturing proper joint alignment is critical to effectively and accurately determining the contact stress engendered within a subject-specific model.

Several limitations are present in the current biomechanical model, mainly the absence of ligament and muscle forces and the omission of a meniscus in the model. Ligament and muscle forces are important for use in dynamic models, in which the knees reach extremes of motion, and in which ligament forces become extremely significant.

However, the present model is capturing a static pose based on a standing task performed according to the MOST radiographic protocol. In this task, motion was constrained in all degrees of freedom except for superior-inferior translation of the talus for load control. Because of this, muscle and ligament forces should be largely implicit within the radiographic alignment. In the static pose used, the meniscus is also thought to be of little importance to the overall contact stress of the joint. Previous work involving DEA methods on a knee model which both included and excluded meniscus showed that meniscus has some impact on contact stress around the peripheral portions of the tibial plateau, but little effect in regions which undergo peak stress (central portions of each compartment)[31].

CHAPTER 5: CONCLUSIONS ON THE EFFICACY OF EXPEDITED CONTACT STRESS EVALUTATION METHODS

Contact stress exposure is thought to play a significant role in many aspects of joint degradation and pathology. Effective and accurate contact stress computation in normal or pathological joints is an important tool in determining the role of contact stress in OA onset and worsening, as well as eventually in developing and monitoring interventions to prevent joint degradation.

In the past, FEA modeling has facilitated studies which relate human ankle joint contact stress exposure to the presence of radiographic OA. While promising, contact FEA for subject-specific models is significantly limited by the number of cases that can be reliably solved. This is due to the difficulty of FEA meshing, as well as numerical convergence issues present in contact FEA. To obtain truly statistically powerful conclusions about the causes of joint degradation and OA onset, large numbers of subject-specific models will need to be created, run and analyzed.

Discrete element analysis, or DEA, has proven to be an effective method of contact stress measurement for both expedited evaluation of PTOA risk following tibial plafond fractures as well as for evaluation of BML worsening in the knees from a cohort of 38 at-risk patients. DEA treats cartilage as a bed of springs attached to an underlying rigid bone surface. It is a significant simplification from FEA in that it does not allow computation of internal stresses of an object. It does not incorporate elaborate material treatments, and it does not address true deformation of an object. This simplification comes with the benefit of reduced computational and investigator burden, due to bypassing numerical convergence issues as well as needing no FEA meshing step.

A custom written DEA algorithm was created in MATLAB, which works in conjunction with a load balancing algorithm to iteratively obtain contact solutions in both load and displacement control. This algorithm was first validated against a previously performed physical validation study involving two human cadaver ankles loaded in a custom built fixture. It was found that the DEA model could reproduce peak contact stresses to within 20% of the physically measured contact stress. When DEA contact stresses were registered and interpolated to the grid of the Tekscan pressure sensor, it was found that there was a 90% probability that the DEA-computed contact stress values differed less than 1 MPa from the physical measurement.

The DEA method was then used to replicate previously obtained FEA results in a study of 22 human ankle joints that had sustained tibial plafond fracture. FEA models and loadings were adapted for the DEA method and were run. DEA offered a significant speed increase while maintaining results comparable to the FEA. Even though DEA-computed contact stress values in areas of high incongruity were higher than the corresponding FEA values, the ability of DEA to predict PTOA development using a contact stress-time exposure metric was virtually unchanged (95% KL grade concordance and 100% OA concordance vs. 94% KL grade concordance and 100% OA concordance, for DEA and FEA, respectively).

The DEA method was then combined with a feature-based 3D-to-2D alignment routine custom-written in MATLAB. This alignment routine used an efficient ray casting method to recreate a virtual x-ray silhouette edge for a 3D model. This model was then aligned to a 2D edge tracing, based on an input radiographic image depicting a functional pose of the bone. A global optimizer (simulated annealing) was used to determine the best Euler transform to place the bone in an accurate position within the recreated virtual scene. Thirty-eight subject-specific knee models segmented from the MOST cohort were aligned to functional appositions based upon fixed-flexion PA standing radiographs. Contact stresses were then obtained from these aligned joints using DEA, to evaluate the relationship between contact stress level and bone marrow lesion worsening. It was found that as contact stress level increased so did the risk of BML worsening, with an odds ratio of 4.4 for cartilage worsening and 6.6 for BML worsening . As the worsening of BMLs is associated with joint pain, degradation, and pathology, an expedited contact stress method which can accurately predict BML worsening is especially valuable.

In the future, the DEA methods may be extended to yet-larger studies of subject-specific models in either the knee or the ankle joint. Larger studies will aid in improving the statistical power of these results. The reduced computational and investigator burden of DEA has shifted the burden from contact stress evaluation and setup to other tasks, such as alignment and segmentation. New and more automated segmentation techniques need to be implemented to effectively utilize the speed gains realized using the DEA method.

The DEA method is highly generalizable across a large number of contact calculation tasks. The ankle and knee joints represent only two of many possible applications of such expedited methods. DEA can be simply and easily modified to compute stress in a wide variety of subject-specific applications. Many different material models can be used to represent springs, thus increasing the range of possible simulations performed. Additionally, implementation of a similar contact algorithm into multi-body dynamics software would allow for simple and efficient computation of contact stresses and forces in dynamic simulations involving more complex motions and loading tasks. With the advent of easily implemented GPU computing, DEA is also amenable to significant computation speed increases with translation to a GPU. This would help to achieve near-real-time computation of contact stress.

Simplified and expedited methods of determining contact stress and functional alignment in subject-specific joint models are important tools for guiding clinical intervention and evaluating future treatment methods. Future translational research will depend on fast and expeditious methods which are easily implemented and which have robust predictive measures, to help bridge the gap between complex and expensive mechanics simulations and easily implemented clinical tools.

APPENDIX A AUXILLARY DATA FROM RIGID BODY SPRING MODEL VALIDATION

Table A-1. An analysis three different NN search techniques using different sized query and database point clouds. Structure build and search times are listed.

		Brute Force		kd-tree		Voronoi	
Database Points	Query Points	Build (s)	Search (s)	Build (s)	Search (s)	Build (s)	Search (s)
86704	2162	NA	10	8	4.8	7	0.5
	5835	NA	18	9	13	7	0.5
	11609	NA	38	8	25	8	0.6
	23023	NA	58	8	50	7	0.8
	78310	NA	292	8	153	7	1.5
25582	2162	NA	2.9	0.8	1.5	2.3	0.13
	5835	NA	5.8	0.8	4	2.3	0.16
	11609	NA	10	0.8	7	2.3	0.2
	23023	NA	15	0.8	16	2.3	0.2
	78310	NA	87	0.8	45	2.3	0.7
12862	2162	NA	1.5	0.21	0.83	1.22	0.07
	5835	NA	2.8	0.21	2.24	1.2	0.091
	11609	NA	4.7	0.22	4.3	1.16	0.12
	23023	NA	7.6	0.21	8.5	1.1	0.18
	78310	NA	44	0.21	24	1.3	0.48
4872	2162	NA	0.57	0.039	0.38	0.3424	0.03222
	5835	NA	1	0.038	1	0.34	0.04
	11609	NA	1.8	0.038	2	0.34	0.07
	23023	NA	2.9	0.04	4	0.34	0.12
	78310	NA	17	0.0388	11	0.34	0.37

APPENDIX B AUXILLARY DATA FROM HUMAN ANKLE CONTACT STRESS EVALUATION

Table B-1. Max and Mean Contact Stress Values for Intact Ankles using DEA at the Highest Loading Point of the Gait Cycle

	Intact Ankles		
Ankle Number	Max Contact Stress (MPa)	Mean Contact Stress (MPa)	Contact Area (mm^2)
1	8.9	4.0	678.8
2	12.4	5.0	716.7
3	8.4	4.8	662.8
4	9.0	4.2	665.4
5	12.9	4.6	508.0
6	7.4	4.2	626.1
7	10.6	4.7	551.4
8	13.3	4.9	792.1
9	9.8	3.6	689.9
10	8.9	3.3	529.8
11	9.2	5.0	624.6

Table B-2. Max and Mean Contact Stress Values for Post-op Fractured Ankles using DEA at the Highest Loading Point of the Gait Cycle.

Ankle Number	Post-op Fractured Ankles			
	Max Contact Stress (MPa)	Mean Contact Stress (MPa)	Contact Area (mm^2)	KL Grade
1	17.0	5.0	543.1	4
2	15.9	6.4	612.3	4
3	13.7	4.6	729.6	2
4	13.0	4.3	725.9	4
5	12.4	4.6	530.0	0
6	12.9	4.1	644.2	0
7	16.7	5.7	475.3	2
8	14.1	5.9	661.7	3
9	14.8	5.5	475.0	3
10	12.7	4.3	454.9	0
11	11.5	5.0	639.7	0

APPENDIX C AUXILLARY DATA FROM HUMAN KNEE CONTACT STRESS EVALUATIONS AND ALIGNMENTS

Table C-1. Differences in Euler Transform Between Custom Alignment Algorithm and JointTrack Using JointTrack Example Dataset.

	SI translation	AP translation	ML translation	IE rotation	VV rotation	FE rotation
1	0.0047	-0.0302	0.6374	-1.0277	-1.5849	0.04620
2	0.0228	-0.0226	0.2328	-0.3731	-1.8152	0.3827
3	0.0039	-0.0370	0.8081	-0.2438	-1.8377	0.1311
4	0.0094	-0.0332	0.6504	-0.3448	-1.6686	0.1103
5	-0.0045	-0.0403	0.8143	-0.3505	-2.0804	-0.0434
6	0.0075	-0.0358	0.6971	-0.2158	-1.8455	0.0816
7	0.0062	-0.0318	-0.7108	-0.3387	-1.8789	0.1846
8	-0.0234	-0.0077	0.4773	-2.9142	-4.1249	0.1466
9	-0.058	0.0222	3.0671	7.9541	0.3665	-0.6771
10	0.0511	-0.0377	2.6170	-2.1742	4.2447	0.8146
11	-0.0114	-0.0661	1.4052	0.1469	-1.7008	-0.4675
12	-0.0300	-0.0583	2.7475	-1.5759	-7.9105	-0.0127
13	-0.0413	-0.0679	2.1533	-1.5351	-3.0323	-0.9955

REFERENCES

1. Anderson, D.D., S. Chubinskaya, F. Guilak, J.A. Martin, T.R. Oegema, S.A. Olson, and J.A. Buckwalter, *Post-traumatic osteoarthritis: improved understanding and opportunities for early intervention.* J Orthop Res, 2011. **29**(6): p. 802-9.

2. CDC. 2011 May 2011; Available from: https://www.cia.gov/library/publications/the-world-factbook/geos/us.html.

3. Buckwalter, J.A. and T.D. Brown, *Joint injury, repair, and remodeling: roles in post-traumatic osteoarthritis.* Clin Orthop Relat Res, 2004(423): p. 7-16.

4. Saltzman, C.L., M.B. Zimmerman, M. O'Rourke, T.D. Brown, J.A. Buckwalter, and R. Johnston, *Impact of comorbidities on the measurement of health in patients with ankle osteoarthritis.* J Bone Joint Surg Am, 2006. **88**(11): p. 2366-72.

5. Valderrabano, V., M. Horisberger, I. Russell, H. Dougall, and B. Hintermann, *Etiology of ankle osteoarthritis.* Clin Orthop Relat Res, 2009. **467**(7): p. 1800-6.

6. Treppo, S., H. Koepp, E.C. Quan, A.A. Cole, K.E. Kuettner, and A.J. Grodzinsky, *Comparison of biomechanical and biochemical properties of cartilage from human knee and ankle pairs.* J Orthop Res, 2000. **18**(5): p. 739-48.

7. Marsh, J.L., J. Buckwalter, R. Gelberman, D. Dirschl, S. Olson, T. Brown, and A. Llinias, *Articular fractures: does an anatomic reduction really change the result?* J Bone Joint Surg Am, 2002. **84-A**(7): p. 1259-71.

8. Brown, T.D. and D.T. Shaw, *In vitro contact stress distribution on the femoral condyles.* J Orthop Res, 1984. **2**(2): p. 190-9.

9. Anderson, D.D., C. Van Hofwegen, J.L. Marsh, and T.D. Brown, *Is elevated contact stress predictive of post-traumatic osteoarthritis for imprecisely reduced tibial plafond fractures?* J Orthop Res, 2011. **29**(1): p. 33-9.

10. Thomas, T.P., D.D. Anderson, J.L. Marsh, and T.D. Brown, *A method for the estimation of normative bone surface area to aid in objective CT-based fracture severity assessment.* Iowa Orthop J, 2008. **28**: p. 9-13.

11. Li, W., D.D. Anderson, J.K. Goldsworthy, J.L. Marsh, and T.D. Brown, *Patient-specific finite element analysis of chronic contact stress exposure after intraarticular fracture of the tibial plafond.* J Orthop Res, 2008. **26**(8): p. 1039-45.

12. Anderson, D.D., J.K. Goldsworthy, K. Shivanna, N.M. Grosland, D.R. Pedersen, T.P. Thomas, Y. Tochigi, J.L. Marsh, and T.D. Brown, *Intra-articular contact stress distributions at the ankle throughout stance phase-patient-specific finite element analysis as a metric of degeneration propensity.* Biomech Model Mechanobiol, 2006. **5**(2-3): p. 82-9.

13. Anderson, D.D., J.K. Goldsworthy, W. Li, M. James Rudert, Y. Tochigi, and T.D. Brown, *Physical validation of a patient-specific contact finite element model of the ankle.* J Biomech, 2007. **40**(8): p. 1662-9.

14. Li, G., M. Sakamoto, and E.Y. Chao, *A comparison of different methods in predicting static pressure distribution in articulating joints.* J Biomech, 1997. **30**(6): p. 635-8.

15. Elias, J.J., D.R. Wilson, R. Adamson, and A.J. Cosgarea, *Evaluation of a computational model used to predict the patellofemoral contact pressure distribution.* J Biomech, 2004. **37**(3): p. 295-302.

16. Chao, E.Y., K.Y. Volokh, H. Yoshida, N. Shiba, and T. Ide, *Discrete element analysis in musculoskeletal biomechanics.* Mol Cell Biomech, 2010. **7**(3): p. 175-92.

17. Blankevoort, L., J.H. Kuiper, R. Huiskes, and H.J. Grootenboer, *Articular contact in a three-dimensional model of the knee.* J Biomech, 1991. **24**(11): p. 1019-31.

18. Bei, Y. and B.J. Fregly, *Multibody dynamic simulation of knee contact mechanics.* Med Eng Phys, 2004. **26**(9): p. 777-89.

19. An, K.N., S. Himeno, H. Tsumura, T. Kawai, and E.Y. Chao, *Pressure distribution on articular surfaces: application to joint stability evaluation.* J Biomech, 1990. **23**(10): p. 1013-20.

20. Schuind, F., W.P. Cooney, R.L. Linscheid, K.N. An, and E.Y. Chao, *Force and pressure transmission through the normal wrist. A theoretical two-dimensional study in the posteroanterior plane.* J Biomech, 1995. **28**(5): p. 587-601.

21. Brekelmans, W.A., H.W. Poort, and T.J. Slooff, *A new method to analyse the mechanical behaviour of skeletal parts.* Acta Orthop Scand, 1972. **43**(5): p. 301-17.

22. Huiskes, R. and E.Y. Chao, *A survey of finite element analysis in orthopedic biomechanics: the first decade.* J Biomech, 1983. **16**(6): p. 385-409.

23. Kloosterman, G., *Contact methods in finite element solutions*, in *Research Scool of Integrated Manufacturing*. 2002, University of Twente: Twente. p. 134.

24. Li, W., Q. Li, G.P. Steven, and Y.M. Xie, *An evolutionary approach to elastic contact optimization of frame structures.* Finite Elements in Analysis and Design, 2003. **40**(1): p. 61-81.

25. Grosland, N.M., K.H. Shivanna, V.A. Magnotta, N.A. Kallemeyn, N.A. DeVries, S.C. Tadepalli, and C. Lisle, *IA-FEMesh: an open-source, interactive, multiblock approach to anatomic finite element model development.* Comput Methods Programs Biomed, 2009. **94**(1): p. 96-107.

26. Fitzpatrick, C.K., M.A. Baldwin, and P.J. Rullkoetter, *Computationally efficient finite element evaluation of natural patellofemoral mechanics.* J Biomech Eng, 2010. **132**(12): p. 121013.

27. Volokh, K.Y., E.Y. Chao, and M. Armand, *On foundations of discrete element analysis of contact in diarthrodial joints.* Mol Cell Biomech, 2007. **4**(2): p. 67-73.

28. Pandy, M.G., K. Sasaki, and S. Kim, *A Three-Dimensional Musculoskeletal Model of the Human Knee Joint. Part 1: Theoretical Construct.* Comput Methods Biomech Biomed Engin, 1998. **1**(2): p. 87-108.

29. Kwak, S.D., L. Blankevoort, and G.A. Ateshian, *A Mathematical Formulation for 3D Quasi-Static Multibody Models of Diarthrodial Joints.* Comput Methods Biomech Biomed Engin, 2000. **3**(1): p. 41-64.

30. Garcia-Elias, M., K.N. An, W.P. Cooney, R.L. Linscheid, and E.Y. Chao, *Transverse stability of the carpus. An analytical study.* J Orthop Res, 1989. **7**(5): p. 738-43.

31. Anderson, D.D., K.S. Iyer, N.A. Segal, J.A. Lynch, and T.D. Brown, *Implementation of discrete element analysis for subject-specific, population-wide investigations of habitual contact stress exposure.* J Appl Biomech, 2010. **26**(2): p. 215-23.

32. Fregly, B.J., W.G. Sawyer, M.K. Harman, and S.A. Banks, *Computational wear prediction of a total knee replacement from in vivo kinematics.* J Biomech, 2005. **38**(2): p. 305-14.

33. Halloran, J.P., S.K. Easley, A.J. Petrella, and P.J. Rullkoetter, *Comparison of deformable and elastic foundation finite element simulations for predicting knee replacement mechanics.* J Biomech Eng, 2005. **127**(5): p. 813-8.

34. Caruntu, D.I. and M.S. Hefzy, *3-D anatomically based dynamic modeling of the human knee to include tibio-femoral and patello-femoral joints.* J Biomech Eng, 2004. **126**(1): p. 44-53.

35. Birthelmer, H., I. Soetebier, and J. Sahm, *Efficient representation of triangle meshes for simultaneous modification and rendering.* Computational Science - Iccs 2003, Pt I, Proceedings, 2003. **2657**: p. 925-934.

36. Fregly, B.J., S.A. Banks, D.D. D'Lima, and C.W. Colwell, Jr., *Sensitivity of knee replacement contact calculations to kinematic measurement errors.* J Orthop Res, 2008. **26**(9): p. 1173-9.

37. Arya, S., D.M. Mount, N.S. Netanyahu, R. Silverman, and A.Y. Wu, *An optimal algorithm for approximate nearest neighbor searching in fixed dimensions.* Journal of the Acm, 1998. **45**(6): p. 891-923.

38. Friedman, J.H., J.L. Bentley, and R.A. Finkel, *An Algorithm for Finding Best Matches in Logarithmic Expected Time.* ACM Trans. Math. Softw., 1977. **3**(3): p. 209-226.

39. Zakarauskas, P. and J.M. Ozard, *Complexity analysis for partitioning nearest neighbor searching algorithms.* Ieee Transactions on Pattern Analysis and Machine Intelligence, 1996. **18**(6): p. 663-668.

40. Aurenhammer, F., *Voronoi Diagrams - a Survey of a Fundamental Geometric Data Structure.* Computing Surveys, 1991. **23**(3): p. 345-405.

41. Barber, C.B., D.P. Dobkin, and H. Huhdanpaa, *The Quickhull algorithm for convex hulls.* Acm Transactions on Mathematical Software, 1996. **22**(4): p. 469-483.

42. Fregly, B.J., H.A. Rahman, and S.A. Banks, *Theoretical accuracy of model-based shape matching for measuring natural knee kinematics with single-plane fluoroscopy.* J Biomech Eng, 2005. **127**(4): p. 692-9.

43. Hertel, J., *Functional Anatomy, Pathomechanics, and Pathophysiology of Lateral Ankle Instability.* J Athl Train, 2002. **37**(4): p. 364-375.

44. Leardini, A., J.J. O'Connor, F. Catani, and S. Giannini, *A geometric model of the human ankle joint.* J Biomech, 1999. **32**(6): p. 585-91.

45. Randale C. Sechrest, M. *eOrthopod*. 2011 [cited 2011; Available from: http://www.eorthopod.com/content/ankle-anatomy.

46. Huei-Ming Chai, P.P. *The Ankle Complex*. 2004 [cited 2011; Available from: http://www.pt.ntu.edu.tw/hmchai/kinesiology/kinlower/ankle.htm.

47. Millington, S.A., M. Grabner, R. Wozelka, D.D. Anderson, S.R. Hurwitz, and J.R. Crandall, *Quantification of ankle articular cartilage topography and thickness using a high resolution stereophotography system.* Osteoarthritis Cartilage, 2007. **15**(2): p. 205-11.

48. El-Khoury, G.Y., K.J. Alliman, H.J. Lundberg, M.J. Rudert, T.D. Brown, and C.L. Saltzman, *Cartilage thickness in cadaveric ankles: measurement with double-contrast multi-detector row CT arthrography versus MR imaging.* Radiology, 2004. **233**(3): p. 768-73.

49. Repo, R.U. and J.B. Finlay, *Survival of articular cartilage after controlled impact.* J Bone Joint Surg Am, 1977. **59**(8): p. 1068-76.

50. Brown, T.D., D.D. Anderson, J.V. Nepola, R.J. Singerman, D.R. Pedersen, and R.A. Brand, *Contact stress aberrations following imprecise reduction of simple tibial plateau fractures.* J Orthop Res, 1988. **6**(6): p. 851-62.

51. DeCoster, T.A., M.C. Willis, J.L. Marsh, T.M. Williams, J.V. Nepola, D.R. Dirschl, and S.R. Hurwitz, *Rank order analysis of tibial plafond fractures: does injury or reduction predict outcome?* Foot Ankle Int, 1999. **20**(1): p. 44-9.

52. Demetriades, L., E. Strauss, and J. Gallina, *Osteoarthritis of the ankle.* Clin Orthop Relat Res, 1998(349): p. 28-42.

53. Saltzman, C.L., M.L. Salamon, G.M. Blanchard, T. Huff, A. Hayes, J.A. Buckwalter, and A. Amendola, *Epidemiology of ankle arthritis: report of a consecutive series of 639 patients from a tertiary orthopaedic center.* Iowa Orthop J, 2005. **25**: p. 44-6.

54. Kellgren, J.H. and J.S. Lawrence, *Radiological assessment of osteo-arthrosis.* Ann Rheum Dis, 1957. **16**(4): p. 494-502.

55. Stauffer, R.N., E.Y. Chao, and R.C. Brewster, *Force and motion analysis of the normal, diseased, and prosthetic ankle joint.* Clin Orthop Relat Res, 1977(127): p. 189-96.

56. Flandry, F. and G. Hommel, *Normal anatomy and biomechanics of the knee.* Sports Med Arthrosc, 2011. **19**(2): p. 82-92.

57. Blackburn, T.A. and E. Craig, *Knee anatomy: a brief review.* Phys Ther, 1980. **60**(12): p. 1556-60.

58. Goldblatt, J.P. and J.C. Richmond, *Anatomy and biomechanics of the knee.* Operative Techniques in Sports Medicine, 2003. **11**(3): p. 14.

59. Felson, D.T., R.C. Lawrence, P.A. Dieppe, R. Hirsch, C.G. Helmick, J.M. Jordan, R.S. Kington, N.E. Lane, M.C. Nevitt, Y. Zhang, M. Sowers, T. McAlindon, T.D. Spector, A.R. Poole, S.Z. Yanovski, G. Ateshian, L. Sharma, J.A. Buckwalter, K.D. Brandt, and J.F. Fries, *Osteoarthritis: new insights. Part 1: the disease and its risk factors.* Ann Intern Med, 2000. **133**(8): p. 635-46.

60. Sharma, L., J. Song, D.T. Felson, S. Cahue, E. Shamiyeh, and D.D. Dunlop, *The role of knee alignment in disease progression and functional decline in knee osteoarthritis.* JAMA, 2001. **286**(2): p. 188-95.

61. Ettinger, W.H., M.A. Davis, J.M. Neuhaus, and K.P. Mallon, *Long-term physical functioning in persons with knee osteoarthritis from NHANES. I: Effects of comorbid medical conditions.* J Clin Epidemiol, 1994. **47**(7): p. 809-15.

62. Lawrence, J.S., J.M. Bremner, and F. Bier, *Osteo-arthrosis. Prevalence in the population and relationship between symptoms and x-ray changes.* Ann Rheum Dis, 1966. **25**(1): p. 1-24.

63. Segal, N.A., J.C. Torner, D. Felson, J. Niu, L. Sharma, C.E. Lewis, and M. Nevitt, *Effect of thigh strength on incident radiographic and symptomatic knee osteoarthritis in a longitudinal cohort.* Arthritis Rheum, 2009. **61**(9): p. 1210-7.

64. Roemer, F.W., R. Frobell, D.J. Hunter, M.D. Crema, W. Fischer, K. Bohndorf, and A. Guermazi, *MRI-detected subchondral bone marrow signal alterations of the knee joint: terminology, imaging appearance, relevance and radiological differential diagnosis.* Osteoarthritis Cartilage, 2009. **17**(9): p. 1115-31.

65. Felson, D.T., C.E. Chaisson, C.L. Hill, S.M. Totterman, M.E. Gale, K.M. Skinner, L. Kazis, and D.R. Gale, *The association of bone marrow lesions with pain in knee osteoarthritis.* Ann Intern Med, 2001. **134**(7): p. 541-9.

66. Hunter, D.J., Y. Zhang, J. Niu, J. Goggins, S. Amin, M.P. LaValley, A. Guermazi, H. Genant, D. Gale, and D.T. Felson, *Increase in bone marrow lesions associated with cartilage loss: a longitudinal magnetic resonance imaging study of knee osteoarthritis.* Arthritis Rheum, 2006. **54**(5): p. 1529-35.

67. Guymer, E., F. Baranyay, A.E. Wluka, F. Hanna, R.J. Bell, S.R. Davis, Y. Wang, and F.M. Cicuttini, *A study of the prevalence and associations of subchondral bone marrow lesions in the knees of healthy, middle-aged women.* Osteoarthritis Cartilage, 2007. **15**(12): p. 1437-42.

68. Felson, D.T., S. McLaughlin, J. Goggins, M.P. LaValley, M.E. Gale, S. Totterman, W. Li, C. Hill, and D. Gale, *Bone marrow edema and its relation to progression of knee osteoarthritis.* Ann Intern Med, 2003. **139**(5 Pt 1): p. 330-6.

69. Shelbourne, K.D., S. Jari, and T. Gray, *Outcome of untreated traumatic articular cartilage defects of the knee: a natural history study.* J Bone Joint Surg Am, 2003. **85-A Suppl 2**: p. 8-16.

70. Baranyay, F.J., Y. Wang, A.E. Wluka, D.R. English, G.G. Giles, R.O. Sullivan, and F.M. Cicuttini, *Association of bone marrow lesions with knee structures and risk factors for bone marrow lesions in the knees of clinically healthy, community-based adults.* Semin Arthritis Rheum, 2007. **37**(2): p. 112-8.

71. Garnero, P., C. Peterfy, S. Zaim, and M. Schoenharting, *Bone marrow abnormalities on magnetic resonance imaging are associated with type II collagen degradation in knee osteoarthritis: a three-month longitudinal study.* Arthritis Rheum, 2005. **52**(9): p. 2822-9.

72. Wluka, A.E., F. Hanna, M. Davies-Tuck, Y. Wang, R.J. Bell, S.R. Davis, J. Adams, and F.M. Cicuttini, *Bone marrow lesions predict increase in knee cartilage defects and loss of cartilage volume in middle-aged women without knee pain over 2 years.* Ann Rheum Dis, 2009. **68**(6): p. 850-5.

73. Roemer, F.W., A. Guermazi, M.K. Javaid, J.A. Lynch, J. Niu, Y. Zhang, D.T. Felson, C.E. Lewis, J. Torner, and M.C. Nevitt, *Change in MRI-detected subchondral bone marrow lesions is associated with cartilage loss: the MOST Study. A longitudinal multicentre study of knee osteoarthritis.* Ann Rheum Dis, 2009. **68**(9): p. 1461-5.

74. Kroner, A.H., C.E. Berger, R. Kluger, G. Oberhauser, P. Bock, and A. Engel, *Influence of high tibial osteotomy on bone marrow edema in the knee.* Clin Orthop Relat Res, 2007. **454**: p. 155-62.

75. Brem, M.H., P.M. Schlechtweg, J. Bhagwat, M. Genovese, M.F. Dillingham, H. Yoshioka, and P. Lang, *Longitudinal evaluation of the occurrence of MRI-detectable bone marrow edema in osteoarthritis of the knee.* Acta Radiol, 2008. **49**(9): p. 1031-7.

76. Davies-Tuck, M.L., A.E. Wluka, A. Forbes, Y. Wang, D.R. English, G.G. Giles, R. O'Sullivan, and F.M. Cicuttini, *Development of bone marrow lesions is associated with adverse effects on knee cartilage while resolution is associated with improvement--a potential target for prevention of knee osteoarthritis: a longitudinal study.* Arthritis Res Ther, 2010. **12**(1): p. R10.

77. Koster, I.M., E.H. Oei, J.H. Hensen, S.S. Boks, B.W. Koes, D. Vroegindeweij, M.G. Hunink, and S.M. Bierma-Zeinstra, *Predictive factors for new onset or progression of knee osteoarthritis one year after trauma: MRI follow-up in general practice.* Eur Radiol, 2011. **21**(7): p. 1509-16.

78. Segal, N.A., D.D. Anderson, K.S. Iyer, J. Baker, J.C. Torner, J.A. Lynch, D.T. Felson, C.E. Lewis, and T.D. Brown, *Baseline articular contact stress levels predict incident symptomatic knee osteoarthritis development in the MOST cohort.* J Orthop Res, 2009. **27**(12): p. 1562-8.

79. Markelj, P., D. Tomazevic, B. Likar, and F. Pernus, *A review of 3D/2D registration methods for image-guided interventions.* Med Image Anal, 2010.

80. Banks, S.A. and W.A. Hodge, *Accurate measurement of three-dimensional knee replacement kinematics using single-plane fluoroscopy.* IEEE Trans Biomed Eng, 1996. **43**(6): p. 638-49.

81. Feldmar, J., N. Ayache, and F. Betting, *3D-2D projective registration of free-form curves and surfaces.* Computer Vision and Image Understanding, 1997. **65**(3): p. 403-424.

82. Florin, C., J. Williams, A. Khamene, and N. Paragios, *Registration of 3D angiographic and X-ray images using sequential Monte Carlo sampling.* Computer Vision for Biomedical Image Applications, Proceedings, 2005. **3765**: p. 427-436.

83. Groher, M., N. Padoy, T.E. Jakobs, and N. Navab, *New CTA protocol and 2D-3D registration method for liver catheterization.* Med Image Comput Comput Assist Interv, 2006. **9**(Pt 1): p. 873-81.

84. Zheng, G., M.A. Ballester, M. Styner, and L.P. Nolte, *Reconstruction of patient-specific 3D bone surface from 2D calibrated fluoroscopic images and point distribution model.* Med Image Comput Comput Assist Interv, 2006. **9**(Pt 1): p. 25-32.

85. Zheng, G., X. Dong, and M.A. Gonzalez Ballester, *Unsupervised reconstruction of a patient-specific surface model of a proximal femur from calibrated fluoroscopic images.* Med Image Comput Comput Assist Interv, 2007. **10**(Pt 1): p. 834-41.

86. Markelj, P., D. Tomazevic, F. Pernus, and B.T. Likar, *Robust gradient-based 3-D/2-D registration of CT and MR to X-ray images.* IEEE Trans Med Imaging, 2008. **27**(12): p. 1704-14.

87. Umeyama, S., *Least-Squares Estimation of Transformation Parameters between 2 Point Patterns.* Ieee Transactions on Pattern Analysis and Machine Intelligence, 1991. **13**(4): p. 376-380.

88. Mahfouz, M.R., W.A. Hoff, R.D. Komistek, and D.A. Dennis, *A robust method for registration of three-dimensional knee implant models to two-dimensional fluoroscopy images.* IEEE Trans Med Imaging, 2003. **22**(12): p. 1561-74.

89. Canny, J., *A computational approach to edge detection.* IEEE Trans Pattern Anal Mach Intell, 1986. **8**(6): p. 679-98.

90. Acker, S., R. Li, H. Murray, P.S. John, S. Banks, S. Mu, U. Wyss, and K. Deluzio, *Accuracy of single-plane fluoroscopy in determining relative position and orientation of total knee replacement components.* J Biomech, 2011. **44**(4): p. 784-7.

91. Baumgart, B.G., *A polyhedron representation for computer vision*, in *Proceedings of the May 19-22, 1975, national computer conference and exposition*. 1975, ACM: Anaheim, California. p. 589-596.

92. Kumar, S., D. Manocha, W. Garrett, and M. Lin, *Hierarchical back-face computation.* Computers & Graphics-Uk, 1999. **23**(5): p. 681-692.

93. Glassner, A.S., *An Introduction to ray tracing*. 1990, London; San Diego, CA: Academic Press.

94. Warren, J., *Barycentric coordinates for convex polytopes.* Advances in Computational Mathematics, 1996. **6**(2): p. 97-108.

95. Moller, T. and B. Trumbore, *Fast, minimum storage ray/triangle intersection*, in *ACM SIGGRAPH 2005 Courses*. 2005, ACM: Los Angeles, California. p. 7.

96. Bresenham, J.E., *An Incremental Algorithm for Digital Plotting.* Communications of the Acm, 1963. **6**(7): p. 366-366.

97. Goffe, W.L., G.D. Ferrier, and J. Rogers, *Global Optimization of Statistical Functions with Simulated Annealing.* Journal of Econometrics, 1994. **60**(1-2): p. 65-99.

98. Chib, S. and E. Greenberg, *Understanding the Metropolis-Hastings Algorithm.* American Statistician, 1995. **49**(4): p. 327-335.

99. Shrout, P.E. and J.L. Fleiss, *Intraclass correlations: uses in assessing rater reliability.* Psychol Bull, 1979. **86**(2): p. 420-8.

100. Wilson, A.J., W.A. Murphy, D.C. Hardy, and W.G. Totty, *Transient osteoporosis: transient bone marrow edema?* Radiology, 1988. **167**(3): p. 757-60.